METHODS FOR EVALUATION OF THE REMAINING SHEAR STRENGTH IN STEEL BRIDGE BEAMS WITH SECTION LOSSES DUE TO CORROSION DAMAGE

Eulogio M. Javier III

Thesis submitted to the faculty of the Virginia Polytechnic Institute and State

University in partial fulfillment of the requirements for the degree of

MASTER OF SCIENCE

In

CIVIL ENGINEERING

Matthew H. Hebdon, Chair
Carin L. Roberts-Wollmann
Roberto T. Leon

May 7, 2020

Blacksburg, Virginia

Keywords: Corrosion, Steel Beam, Load Rating, Bridges

Methods for Evaluation of the Remaining Strength in Steel Bridge Beams with Section Losses due to Corrosion Damage

Eulogio M. Javier III

ABSTRACT

This research is intended to better understand the structural behavior of steel bridge beams that have experienced section loss near the bearings. This type of deterioration is common in rural bridges with leaking expansion joints, which exposes the superstructure to corrosive road deicing solutions. Seventeen beams from 4 decommissioned structures throughout Virginia were tested to induce web shear failure near the bearing locations and measured for load, vertical displacement, and web strain behavior. The strain was measured using a digital image correlation (DIC) system to create a digital strain field at equal loading and beam displacement intervals during testing. The data recorded during these large-scale tests was compared to several existing methods for calculating the shear capacity of the damaged beams. Finally, the most appropriate method of these approaches was identified based on accuracy, conservatism, and ease of implementation for load rating. When using load rating methods to determine a steel beam's capacity, this study also recommends that the effective area of the web used in determining the percentage of remaining thickness should consist of the bottom 3 inches of the web and should extend the length of the bearing plus one beam height excluding any areas without any noticeable section losses.

Methods for Evaluation of the Remaining Strength in Steel Bridge Beams with Section Losses due to Corrosion Damage

Eulogio M. Javier III

GENERAL AUDIENCE ABSTRACT

Older bridge structures typically include a rubber joint near the ends to allow for expansion and contraction of the bridge due to heating and cooling from the weather. In many cases, these joints will get damaged due to impacts from vehicle tires and other environmental disturbances. Damage to these joints allows for water to leak through, which, while not in of itself harmful, also allows melting snow to carry road salts laid in the winter to spread onto the underlying bridge steel. These salts cause aggravated corrosion of the steel beams below the bridge's deck, resulting in damage or collapse of the bridge itself. The goal of this study was to characterize this damage and determine how it affects the remaining capacity of the bridge. This objective was achieved by testing 17 beams from 4 out of service bridges with varying damage levels. A load was applied near the damaged ends to determine their behavior during loading, to locate areas of high strain resulting from corrosion, and find the beam's capacity. Several methods to predict the remaining strength in corroded steel beams were compared and recommendations made based on accuracy and conservatism

Table of Contents

List of Figures

List of Tables

CHAPTER 1: Introduction

1.1 Background

Due to the aging infrastructure in the United States, significant effort is required to maintain and repair existing bridges. While many factors contribute to the degradation of bridge conditions, losses in steel bridge capacity over time can often be attributed to the corrosion of steel beams. Although this is a natural occurrence, the process may be aggravated due to pollutants, most notably chlorides that have a pronounced effect on the speed of corrosivity in metals. In the United States, the most common chloride sources for bridges are from seawater and road salts. The exposure of steel superstructure beams to road salts often occurs due to the leaking of expansion joints located above bearing locations. Roadway runoff from these damaged joints can cause accelerated corrosion of the beam ends, which can result in significant web thickness losses to occur over time. These losses can reduce the available web area to resist the high shear loads typically present at the supports. As a result, many bridges have been posted for reduced capacity or closed to traffic due to operating safety concerns.

The Virginia Department of Transportation (VDOT) often deals with bridges experiencing beam end corrosion and has expressed concerns with the current evaluation methods and load rating of these corroded structures. VDOT's current approach to assessing the severity of deterioration on beam ends is through the use of a corrosion rating on a 1-4 scale ranging from good to severe respectively (See Figure 1). However, this method is highly subjective and depends on the judgment of bridge inspectors and the visibility of the corrosion. The information provided by these ratings is qualitative; however, the consensus of bridge inspectors in the Staunton, Virginia district is that a rating of one indicates less than 1/16-inch section loss, two shows approximately 1/16-inch, and three shows greater than 1/16-inch of section loss. Furthermore, the element descriptor does not distinguish between corrosion locations on the web or flanges. Information regarding the actual quantity of section loss is dependent on the description given in the VDOT inspection report, which is up to the discretion of the inspector. Typically, an approximated uniform section loss on the web and flanges is given, but provided diagrams, dimensions, and pictures vary between VDOT districts and even inspectors.

VDOT ELEMENT NUMBER	**811**	**VDOT ELEMENT NAME**	**BEAM/GIRDER END**
DESCRIPTION	**This element defines the last 5 feet of a beam/girder end. Measurement shall begin at the end of the beam/girder and continue toward the center of the structure.**		
UNIT OF MEASURE	**EA**		

STEEL		**CONDITION STATES**			
DEFECT		**1** **GOOD**	**2** **FAIR**	**3** **POOR**	**4** **SEVERE**
1000	Corrosion	None	Freckled Rust. Corrosion of the steel has initiated.	Section loss is evident or pack rust is present but does not warrant structural review.	The condition warrants a structural review to determine the effect on strength or serviceability of the element or bridge; OR a structural review has been completed and the defects impact strength or serviceability of the element or bridge.
1010	Cracking	None.	Crack that has self-arrested or has been arrested with effective arrest holes, doubling plates, or similar.	Identified crack that is not arrested but does not warrant structural review.	
1020	Connection	Connection is in place and functioning as intended.	Loose fasteners or pack rust without distortion is present but the connection is in place and functioning as intended.	Missing bolts, rivets, or fasteners; broken welds; or pack rust with distortion but does not warrant a structural review.	

Figure 1. Corrosion Condition Rating as per VDOT Supplement to the AASHTO Bridge Inspection Manual for Bridge Element Inspection (VDOT, 2016)

Current methods used by VDOT to evaluate the remaining carrying capacity of beams use simplified beam cross-sections applied to AASHTO calculations for shear capacity. However, these simplified methods are not representative of the actual failure behavior of the beams. They depend on an assumed constant cross-sectional beam area. However, the actual affected region is a variable three-dimensional portion of the beam between the applied load and the support. The primary objective of this research is to determine a more appropriate method for VDOT to use for load rating bridges with steel beams exhibiting beam end corrosion. That is, to formulate a more accurate calculation that does not require an unreasonable amount of additional effort by bridge inspectors.

1.2 Corrosion Behavior

Corrosion of steel occurs as an electrochemical process whereby ferric ions are formed on the surface of the steel, which can react with atmospheric oxygen to create iron oxide (Cramer and Covino 2003). This process occurs due to the presence of an exposed metal surface, oxygen, water, and some form of electrolyte. Localized anodes and cathodes are formed on the metal's surface, which allows for the transfer of electrons through the electrolyte. At the anode, the surface iron reacts with water to form a hydrated oxide such as goethite, while electrons flow to the cathode, where oxygen and water react to form hydroxide. While this is typically a mechanism dependent upon atmospheric humidity or aerosols carrying moisture onto the metal's surface, this process is accelerated when the metal is exposed to excessive amounts of electrolyte rich water like seawater or roadway runoff.

Rusting of steel beams like those being tested in this study will typically occur due to exposure of the steel to chlorides in the atmosphere or from roadway deicing chemicals. These chemicals include both road salts and road brining pre-treatments, which are typically sodium chloride or calcium chloride. Regions of the United States which are more heavily affected by snow will typically apply higher amounts of deicing chemicals to roads and bridges during the winter, seen in Figure 2 (Roberge 2012), which shows a corrosivity map of the US. When bridge expansion joints are damaged during use, melting snow carries these salts over the road surface and can leak onto the ends of steel beams. This leakage exposes the beam ends directly below the joints to significantly more surface electrolytes than normal environmental conditions, enabling faster corrosion rates due to the process's electrochemical nature.

These chlorides can be an especially significant problem for bridges that are not routinely power washed, including most secondary and low traffic structures in Virginia.

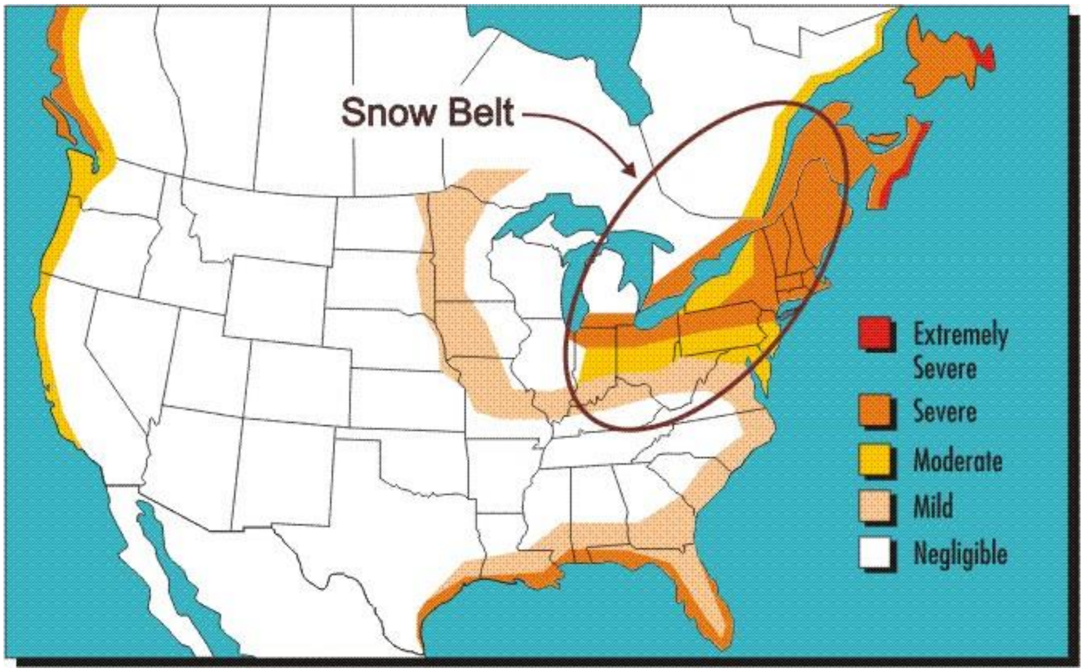

Figure 2. Corrosivity Map of the United States due to Road Salt Usage (Roberge 2012)

An additional feature of the corrosion process is its susceptibility to the presence of water, which is essential to the formation of corrosion on the steel's surface. Wet environments with relative humidity remaining above 80% for long periods of time, followed by alternating low humidity or dry periods cause corrosion to occur quickly. Such conditions may occur in the summer months in Virginia to bridges above waterways due to the constant water evaporation, and in winter due to alternating periods of snowfall and snow melt. This is known as wet-dry cycle corrosion which is the perfect condition for chlorides to form a thin electrolyte layer on the surface of steel.

An example of structures in Virginia that receive low amounts of maintenance is SS8 bridges, which refers to bridges with steel beams and timber deck superstructures (Figure 3). These structures comprise 17.2% or 2,509 of the 14,547 bridges in the VDOT inventory (VDOT 2019). In addition to atmospheric moisture, water can also be stored in the bridge timbers or in dirt and debris on the abutment seat prolonging the beam's exposure. In this case, the experienced corrosion can be severe and concentrated on the top flange of the beam, however, the damage on these structures is continuous rather than targeted at the beam ends. Although VDOT is working to replace these deteriorating structures, these efforts are limited by the available funding and total structural replacement cost.

Figure 3. Example of an SS8 bridge in Alleghany County, Virginia (VDOT, 2019)

1.3 Objective and Scope

The purpose of this research was to determine an appropriate method of assessing the remaining capacity of beams that exhibit web section losses due to corrosion. Several available capacity calculation methods were compared against the results of 17 steel beam tests to determine their accuracy and applicability for VDOT uses. Results from this analysis may increase the reliability of capacity assessment for corrosion-damaged steel bridges, which may yield safer load ratings and higher confidence when load posting bridges.

This research's scope includes both laboratory testing and determination of a method to predict corroded beam end shear capacity. Full-scale flexural testing of 17 steel beams was conducted at the

Thomas Murray Structures Laboratory at Virginia Tech. These steel beams were acquired from bridges located in several VDOT districts throughout Virginia and selected to encompass a full range of damage. This range includes beams from near zero section loss to severe localized end damage, including full height web thickness reduction and through-thickness holes. Several existing capacity calculation methods were then compared to determine their correlation to the full-scale testing results.

CHAPTER 2: Literature Review

2.1 Introduction

Several methods to determine the shear capacity of steel beams assume that beams maintain a constant cross-section for some length of the beam, which introduces difficulty when assessing corroded beams. A corroded cross-section may be uneven and often unsymmetrical, making both accurate measurement and calculation of the sectional properties challenging to achieve. Additionally, this damage can be continuous over the beam's length, which is not accounted for with an assumed cross-section. Inspection reports will often simplify the damage to an assumed web thickness reduction over an area representing a loss in fidelity of the actual dimensions. Even though more precise measurements can be taken, it is not practical to do so for every structure experiencing corrosion behavior. The following studies propose several methods for addressing beams with corrosion that may also be applied to the beams used in this experiment.

2.2 Kayser and Nowak - Early Work Concerning Beam End Deterioration

Initial research regarding the behavior of corroded steel beams was conducted by Jack R. Kayser and Andrzej S. Nowak, whose paper on "Capacity Loss due to Corrosion in Steel-Girder Bridges" set a basis for all studies concerning steel beam corrosion behavior (Kayser and Nowak 1989a). In this study, corrosion source, rate, and pattern were analyzed to determine their effect on simple span steel girders' structural capacity. The parameter for expressing loss of material due to corrosion was referred to as 'Loss per Surface," calculated by taking the area of an affected surface and dividing it by the average depth of the material loss within that area. This measure's advantage is that the affected area's entirety can be quantified rather than addressing a specific cross-section along the beam's length.

It was determined that an initial linear relation exists between the surface loss in the web near the girder end and the shear and bearing capacity of the girder. After some indefinite quantity of thickness loss, this relation became nonlinear, and the capacity rapidly decreases for shear and bearing. The relationship between the loss per surface measurement and the percent remaining shear and bearing capacity is presented in the curves in Figure 4 and Figure 5 respectively. The initial linear relationship present in both sets of curves can be preserved for bearing capacity by using stiffeners designed to AISC or AASHTO specifications, while such behavior occurs regardless of shear capacity. Conclusions from this study recognized that flexure ceases to be the governing failure mode for bridges with severe amounts of corrosion. The shear and bearing relation found in this study apply specifically to four beam sizes: W36x230, W36x182, W30x116 and W24x76. As such, these curves may not be directly used to estimate the remaining shear capacity in VDOT's inventory of bridges which consists of many different beam shapes.

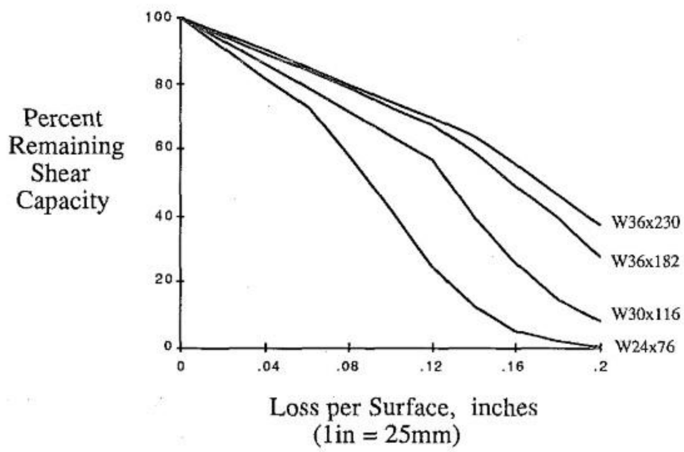

Figure 4. Relation Between Web Thickness Loss per Surface and Percent Remaining Shear Capacity (Kayser & Nowak 1989a)

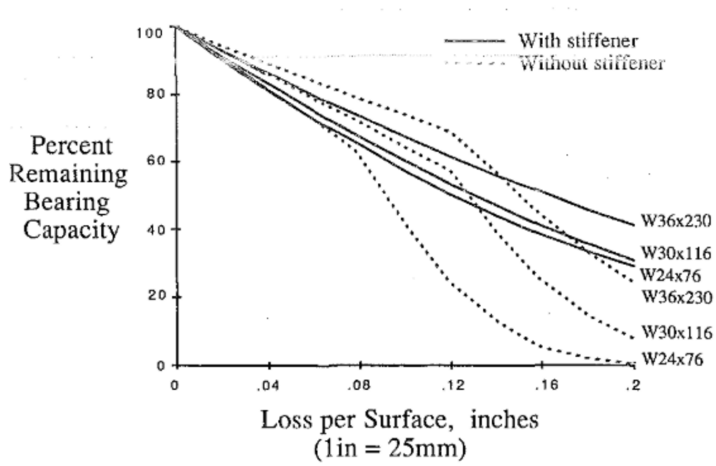

Figure 5. Relation Between Web Thickness Loss per Surface and Percent Remaining Bearing Capacity (Kayser & Nowak, 1989a)

This second study conducted by Kayser and Nowak was similar to their first study and identified the importance of girder slenderness and web compression on bridge reliability when discussing the effects of corrosion (Kayser and Nowak 1989b). It stated that the plate slenderness of compression elements most heavily influences steel plate girder bridges' safety. Thus, the steel web plates, primarily in compression, were most susceptible to thickness losses due to corrosion and the corresponding increase in slenderness. This observation demonstrated that governing failure mode can change due to corrosion damage, addressed in the capacity loss study. Additionally, the absence of bearing stiffeners on short-span bridges with high corrosion levels was observed to reduce bridge reliability over a 50-year lifecycle significantly.

2.3 Van De Lindt – MDOT Study and Capacity Ratio Curves

The Michigan State Department of Transportation (MDOT) had previous issues with corrosion of steel girder bridges attributed to exposure to road salts. Their method of assessing the remaining strength of bridges exhibiting significant section losses has been through either finite element analysis of individual structures or application of the simplified method, which they had found too conservative (van de Lindt and Ahlborn 2005). A set of 16 out-of-service bridges was selected for a study to determine their remaining capacity due to corrosion damage. To facilitate this, three-foot sections of damaged girders were taken from bridges and were loaded to induce buckling or crushing. The finite element programs

ABAQUS and SDRC I-DEAS were used to estimate the governing failure mode, and each specimen was loaded in an MTS test frame to confirm the models' accuracy. Results showed a good correlation between the initial models and the capacities from testing.

A set of design charts were created to relate the measured damage height and depth to the remaining capacity expressed by a deterioration factor Ψ_d using this data. This method allowed for a remaining bearing capacity correlating to the prior test results to be determined quickly given the damage measurements. This deterioration factor method was then compared to the simplified MDOT reduced section calculations using formulas from LRFD. The correlation was not entirely clear. In some cases, the deterioration factor gave more conservative estimates of capacity than the simplified method. This behavior could be partially due to the oversimplification of section loss parameters in the simplified method. Assuming the finite element study represents actual beam behavior, estimated capacity was typically increased using this modified MDOT method. This approach would give load raters additional leeway in determining the adequacy of existing structures before requiring posting for reduced capacity.

2.4 Sugimoto – Durability Evaluation and Presentation of a Simplified Method

After the work presented by Kayser and Nowak in 1989, there was an absence of studies regarding corroded beam capacities during the 1990s. However, due to an aging infrastructure of highways and expressways in both the United States and Japan, the early 2000s saw an increase in interest concerning bridge maintenance efforts. This period was when Dr. Ichiro Sugimoto, Dr. Yusuke Kobayashi, and Dr. Atsushi Ichikawa conducted a study regarding the durability of steel deck girders; and the scientific literature regarding the field of corroded beam capacities began to see publication (Sugimoto et al. 2006).

In the Sugimoto study, the topic of discussion was the aging steel railway infrastructure of Japan. Predating the extensive expressway network constructed in the years after World War II, railways had been an essential function in Japanese society since their introduction in the 1800s. Thus, the deterioration of aging steel deck girders required a capacity evaluation method that prioritized the repair and replacement of Japanese railway bridges. It was noted in this study that ultimate strength evaluation methods at the time relied on assumed values of steel properties, the existing "structural form," and the degree of corrosion, which were regarded as "uncertainties." As a result, the research included experimental testing on out-of-service steel plate girders from a railway bridge built in 1904. Corrosion on the bridge girders was measured using a laser displacement sensor, where the vertical position of top flange was recorded at several cross-section locations and averaged.

A four-point flexural bending test was performed on the steel plate girders to determine the influence of the existing corrosion patterns on the girders' flexural capacity. The girders' mode of failure was local buckling of the top flange in between the loading points, where corrosion of the gusset connection was observed. The relationship between the applied loads and vertical displacement of the beams was linear until the top flange began to yield during the test. The beams then started to bend at the midspan until the maximum load was achieved, shown in Figure 6. Static nonlinear analysis was conducted in ABAQUS to replicate the test conditions, which modeled the corrosion conditions and approximated the local failure mode at the reduced upper flange section.

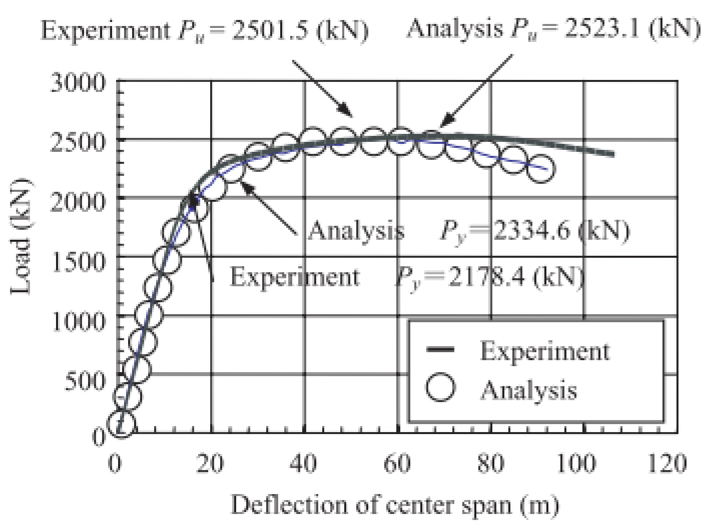

Figure 6. Load vs Midspan Deflection Curve (Sugimoto et al., 2006)

Following the flexural tests on the out-of-service girders, a second series of shear strength tests was conducted on a plate girder with artificially accelerated corrosion patterns created using a saltwater spray. Testing was applied with a single point shear load near a roller bearing resulting in an out-of-plane web buckling. This behavior was again approximated in a finite element analysis program to prove the validity of finite element analysis in predicting the behavior. As a result of these tests, it was determined that the section losses' location did not predominantly determine the capacity of the beam. Instead, the remaining strength was governed by an average web thickness measured along a diagonal line from the support. Furthermore, a simplified strength evaluation method was determined for both the bearing and shear strength of plate girder structures. Regarding shear, a relation was found between the average plate thickness reduction ratio in Equation 1 and the shear buckling strength in Equation 2. The following formulae were presented:

$$R_{tavg} = \frac{t_0 - t_{avg}}{t_0}$$

Equation 1. Average Plate Thickness Reduction Ratio Equation (Sugimoto et al. 2006)

Where:
R_{tavg} = average plate thickness reduction ratio
t_0 = design plate thickness
t_{avg} = average residual plate thickness

$$R_{P_{rc}} = \frac{P_{cr}}{P_{cr(0)}}$$

Equation 2. Shear Buckling Strength Ratio Equation (Sugimoto et al. 2006)

Where:
R_{Prc} = shear buckling strength ratio
P_{cr} = shear buckling strength in a corroded state
$P_{cr(0)}$ = shear buckling design strength

The average plate thickness was measured along a 45-degree slant perpendicular to the web plate's shear force to determine the governing corrosion measurement used in the equation. Assuming the critical applied shear load is located at a distance equal to one web height away from the end of the support, this 45-degree line designated the web area affected by the direct flow of forces between the applied load and the support. Using the average web thickness along this path, in theory, accounted for the damage sustained along the web's critical section.

2.5 Rahgozar and Sharifi – Remaining Capacity using Minimum Curves

Following this study by Sugimoto, Iranian researchers Reza Rahgozar and Yasser Sharifi published a series of papers concerning corroded steel beam sections' capacity. In 2009, Rahgozar conducted an analytical study that looked at the remaining capacity of corroded beam models to establish minimum curves that could be used to predict the remaining strength of several universal beam (UB) sections (Rahgozar 2009). It proposed that the United States' visual inspection methods are not rigorous enough to adequately evaluate a bridge's corrosion conditions. While this study also evaluates corrosion effects on bending capacity like the Sugimoto paper, the following synthesis of the literature will focus solely on shear and bearing effects.

Calculations made by Rahgozar concerning shear capacity refer to British Standard 5950 Part 1 from 1985 (BS 5950), which states the following equations (Equation 3 and Equation 4) concerning critical shear strength (q_{cr}):

$$q_{cr} = 0.6p_{yw} \text{ for } \lambda_w \leq 0.8$$

$$q_{cr} = 0.6p_{yw}[1 - 0.8(\lambda_w - 0.8)] \text{ for } 0.8 < \lambda_w < 1.25$$

$$q_{cr} = q_e \text{ for } \lambda_w \geq 1.25$$

Equation 3. Critical Shear Strength Equations (Rahgozar 2009)

Where:

q_{cr} = critical shear strength of a plate girder web panel

p_{yw} = web design yield strength

q_e = elastic critical shear stress

λ_w = equivalent web slenderness factor

$$\lambda_w = \sqrt{\frac{0.6p_{yw}}{q_e}}$$

Equation 4. Equivalent Web Slenderness Factor Equation (Rahgozar 2009)

The minimum curves established in this study allowed for the remaining capacity to be estimated using a measured percent loss of the web thickness. An example of one of these curves is shown in Figure 7 for beam webs with uniform corrosion, while additional curves may be used for beams with varying corrosion. These curves rely on the categorization of damage into:

Category 1 - where the web depth to thickness ratio $\frac{d}{t} \leq 63\sqrt{275/p_y}$

Category 2 - where the web depth to thickness ratio $\frac{d}{t} > 63\sqrt{275/p_y}$

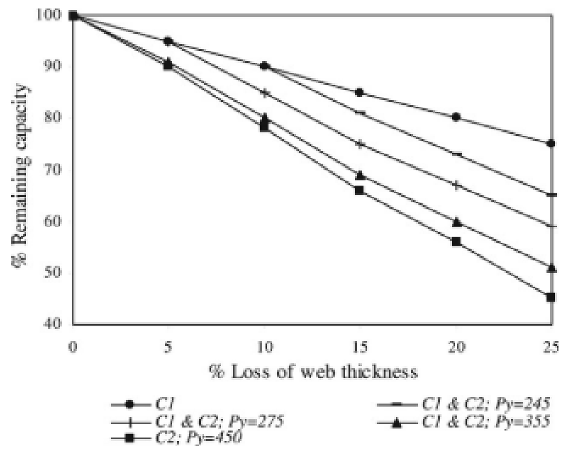

Figure 7. Minimum Curve for Shear Capacity of Webs with Uniform Corrosion (Rahgozar 2009)

Regarding the applicability to the current study, these curves do not continue past 25% loss of web thickness. They cannot be directly used to determine the corroded specimens' capacity. The existing curves could be extended to extrapolate an estimated capacity at higher section losses; however, the accuracy of these curves is not guaranteed past the known data points.

2.6 Kim, Lee, Ahn and Kainuma – Residual Shear Strength of Locally Corroded Webs

Several studies involving work done by Jin-Hee Ahn, In-Tae Kim, Shigenobu Kainuma, and Myoung-Jin Lee are associated with steel beam corrosion; however, two studies from 2013 concern the determination of remaining shear buckling capacity. The first study, published in February of 2013, addresses a set of experiments conducted to determine the shear behavior of corroded web panels on plate girder specimens (Kim et al. 2013). In this study, five plate girder end panels with varying degrees of artificial corrosion were loaded in shear to determine the effects of uniform section loss on the remaining shear capacity. An example of this corrosion and the dimensions of the specimen can be found in Figure 8 and Table 1. The artificial corrosion was produced using metal cutting router bits, which removed varying amounts of thickness from the web at varying heights. Note that the difference between the undamaged control girder Ch00T6 and specimen Ch0'T6 is that the latter's web is separated from the bottom flange along the corroded area's length by removing the weld in this area.

Table 1. Dimensions of Artificially Corroded Plate Girder Specimens (Ahn et al., February 2013)

Geometry of shear loading test specimens (mm)										
	Height (H)	**Width of flange (W_t)**	**Length of web (d_s)**	**d_e**	**d_f**	**Web thickness (t_w)**	**Flange thickness (t_f)**	**Stiffener thickness (t_m)**	**Corroded height (C_h)**	**Corroded Thickness (t_c)**
Ch00T6	800	200	1200	20	200	6	16	12	0	6
Ch10T4									100	4
Ch20T4									200	4
Ch10T2									100	2
Ch0'T6									0	6

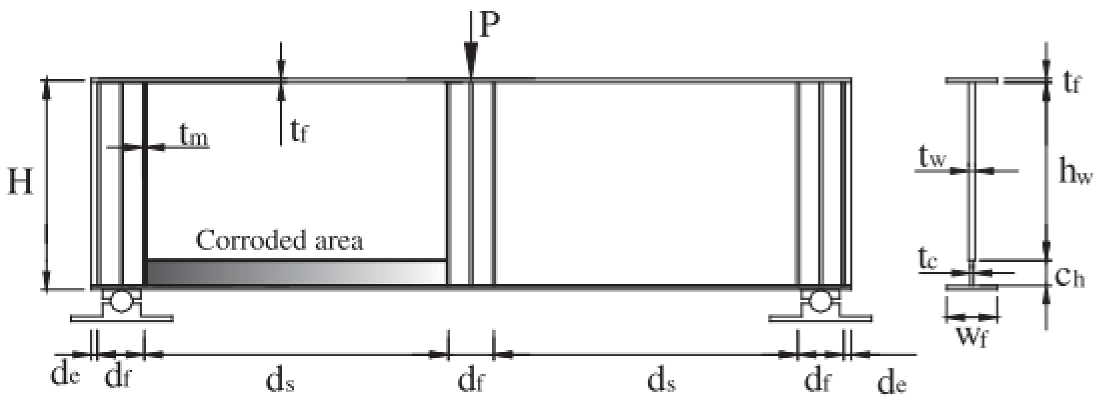

Figure 8. Specimen Dimensions and Affected Corrosion Area (Ahn et al., February 2013)

These experiments show that in these web end panels, two measures of corrosion damage govern the effect of the damage on the remaining capacity. Firstly, the increase in corroded volume quantified as a ratio of the current to the original volume was related to a decrease in shear buckling strength, as shown in Table 2. Specimen Ch0'T6 experienced a significant loss in shear buckling strength, despite having no thickness loss. Therefore, an additional relation exists between the boundary conditions of the web panel and the remaining capacity. The effects of the boundary conditions were merely observed without a stated relationship in the study. A curve for the relation between corroded volume ratio and the shear buckling strength ratio was created and is shown in Figure 9. During the same year, Ahn et al. published a related study, which introduced a finite element model of the previously tested plate girders (Ahn et al. 2013). A best-fit curve was created using the finite element model results, which can be seen in Figure 10.

Table 2. Results of Shear Testing and Comparison to Design Code Estimated Capacities (Ahn et al., February 2013)

Design code comparisons of critical shear buckling loads and shear buckling strengths											
Specimens	**Corroded Volume ratio**	**Shear load test results**		**Critical shear buckling equation [AASHTO]**		**AASHTO**		**AISC**		**JSCE**	
		Critical buckling load (kN)	**Shear buckling strength (kN)**	**Critical buckling load (kN)**	**Ratios for values**	**Critical buckling load (kN)**	**Ratios for values**	**Critical buckling load (kN)**	**Ratios for values**	**Critical buckling load (kN)**	**Ratios for values**
Ch00T6	1	673.15	1286.54		0.54		0.52		0.53		0.77
Ch20T4	0.92	597.86	1152.46		0.57		0.58		0.60		0.86
Ch10T4	0.96	610.50	1275.75	362.69	0.57	671.59	0.53	687.05	0.54	987.89	0.77
Ch10T2	0.92	659.50	1186.37		0.55		0.57		0.58		0.83
Ch0'T6	1	482.47	1017.46		0.75		0.66		0.68		0.97

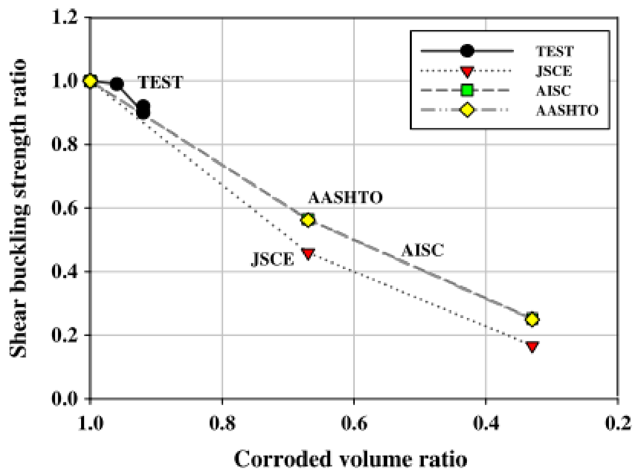

Figure 9. Chart of Shear Testing Results and Calculated Capacities Using Design Codes (Ahn et al., February 2013)

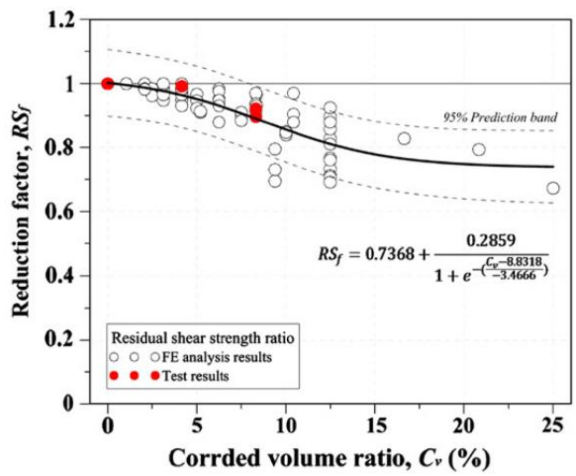

Figure 10. Curve of Shear Testing Results and Finite Element Modeling Results (Ahn et al., August 2013)

The application of these results for capacity estimation is limited because the specimens were plate girders, and the current study was conducted on rolled shapes without stiffeners. It is worth noting that the corrosion effects on the boundary conditions of the beams may be relevant to the current research.

2.7 Tzortzinis and MassDOT Procedure

A more recent study concerning steel beam corrosion was conducted at the University of Massachusetts Amherst. Massachusetts Department of Transportation (MassDOT) inspection data was analyzed to understand the most common damage patterns and locations for bridges experiencing beam-end corrosion (Tzortzinis et al. 2018). In total, 93 structures and 732 total corroded beams were used as subjects for the study. Deterioration patterns were split into two groups: general corrosion and holes. Within these groups, six general corrosion patterns and four through-web hole patterns were identified as representative of the beam end section losses in the raw data gathered from MDOT inventory. Pattern data from bridge inspection documents were compiled into spreadsheets, summarizing each bridge in the study. Subsequently, a MATLAB script was generated to extract the data from all of the spreadsheets into a single data set. This data set was then used to make several critical statistical observations about the state of beam end corrosion behavior, with now 18 characteristic corrosion patterns determined through the statistical post-processing. These observations include potential links between these characteristic corrosion patterns, alluding to a typical evolution between these observed patterns' subsets. Additionally, analytical modeling was proposed for these 18 corrosion patterns to determine their effects on the remaining capacity of deteriorated girders.

Further work in association with MassDOT yielded a 2019 report regarding an effort to load rate deteriorated steel beam ends (Tzortzinis et al. 2019). This report follows the deterioration pattern work done in 2018, with experimental work and finite element modeling. The experimental tests began with six corroded beam specimens selected from a set of beams from the replaced Colrain and Charlemont bridges in Massachusetts. These beams were chosen due to their limited distortion. The loading test configuration was a beam-end shear test with an applied load located 5 feet from the beam end support. Each beam was fitted with strain gauges, potentiometers, linear variable differential transducers (LVDTs), load cells, and pressure transducers. The load test results are tabulated in Table 3, along with the predicted capacities using the current MassDOT equations for shear capacity.

Table 3. Experimental Results of Load Testing (Tzortzinis et al. 2019)

Specimen	Bridge	Beam type	Max Applied Load (kips)	Bearing Failure Load (kips)	Prediction (kips)
1	Colrain	33WF125	134.1	99.1	38.3
2	Colrain	33WF132	91.3	67.6	102.2
3	Colrain	33WF125	112.5	84.3	0
4	Charlemont	21WF73	53.3	42.8	91.5
5	Charlemont	21WF73	45.1	30.9	17.6
6	Charlemont	21WF59	58.8	40.9	6.1

Following the load testing, a set of finite element models were created in Abaqus to model different corrosion behaviors outside of those exhibited in the actual specimens. The previous 2018 pattern study was referenced, and a computer script was created to automate the creation of corrosion scenarios run by the finite element analysis program. Several corrosion patterns were applied to the beam shapes with varying degrees of thickness loss, and several curves were generated for various beam shapes. These curves were then used to modify existing MassDOT shear capacity equations to fit the capacity curves better using various constants.

Calculations to determine web-crippling capacities are modified forms of previous MassDOT formulas found in the current MassDOT Bridge Manual. The initial coefficients in these formulas were based on linear regression used to determine the impact of several variables describing beam geometry and corrosion severity. The proposed MassDOT equation for corroded web resistance is provided in Equation 5:

$$\text{Corroded Web Factored Resistance} = \text{Min}\left[\phi R_{n,yield}, \phi R_{n,crip}\right]$$

Equation 5. Factored Resistance Equation (Tzortzinis et al. 2019)

Where:

$\phi R_{n,yield} = (\phi_b = 1.0)\ (R_{n,yield})$

$\phi R_{n,crip} = (\phi_b = 0.8)\ (R_{n,crip})$

The corroded web factored resistance is taken as the minimum of the calculated nominal yield and crippling capacity shown in Equation 6 and Equation 7, respectively:

$$R_{n,yield} = F_y t_{ave}(2.5k + N)$$

Equation 6. Corroded Web Yielding Capacity Equation (Tzortzinis et al. 2019)

Where:

t_{ave} = the average remaining thickness within the bottom 4 in. of the web height (in.)

k = distance from outer face of flange to web toe fillet (in.)

N = bearing length (in.)

$$R_{n,crip} = \left(\boldsymbol{c}\sqrt{EF_y t_f}\, t_{ave}^{1.2} + \boldsymbol{d}\left(\frac{(N-H)}{d}\right)\frac{\sqrt{EF_y t_f}}{t_f^{1.5}}(t_{ave})^3\right)\left(\frac{t_{ave}}{t_{web}}\right)^{\boldsymbol{h}}$$

Equation 7. Corroded Web Crippling Capacity Equation (Tzortzinis et al. 2019)

Where:

t_f = flange thickness (in.)

H = length of hole along length used for capacity (in.)

t_{web} = nominal web thickness of the intact section

d (non-bold) = beam depth

c, **d**, and **h** = corroded web equation coefficients as defined in Table 4 below

Table 4. Modified MassDOT Equation Coefficients (Tzortzinis et al. 2019)

Imperfection Amplitude	**1 t_{web}**	**0.5 t_{web}**	**0.1 t_{web}**
c	0.33	0.32	0.38
d	0	0.17	0
h	0.4	0.2	0.15

Finally, t_{ave} is the calculated average web thickness considering web holes presented in Equation 8 as:

$$t_{ave} = \frac{(N + md - H)t_w}{(N + md)}$$

Equation 8. Average Web Thickness Formula for Corroded Web Capacity Equations

Where:

m = average web thickness factor defined in Table 5

t_w = remaining web thickness (defined over bottom 4 inches of web in study)

Table 5. Proposed values of factor m, for average web thickness calculation

	Imperfection Amplitude		
	1 t_{web}	**0.5 t_{web}**	**0.1 t_{web}**
N/d > 0.2	0.2	0.2	0.1
N/d ≤ 0.2	0.1	0.1	0

These equations can undoubtedly be applied to the specimens in the current study. This research is the most relevant of those available in the current literature. It addresses rolled shapes without stiffeners and presents a method for capacity calculation for beams with end corrosion. The only significant difference is in the size of the beams tested. The current study targets much smaller rolled sections, common in older and rural structures.

In January 2020, MassDOT released a revision to their bridge load rating guidelines which has not yet incorporated the Tzortzinis study (MassDOT 2020). The MassDOT Bridge Manual defines the area over which the corroded web thickness must be measured. This is defined as the bottom four inches of the web above the bearing length and 2.5k on either side of the bearing (Figure 11). Additionally, it makes clear that although a buckling capacity procedure was previously determined, it is not included in the current revision due to overly conservative results.

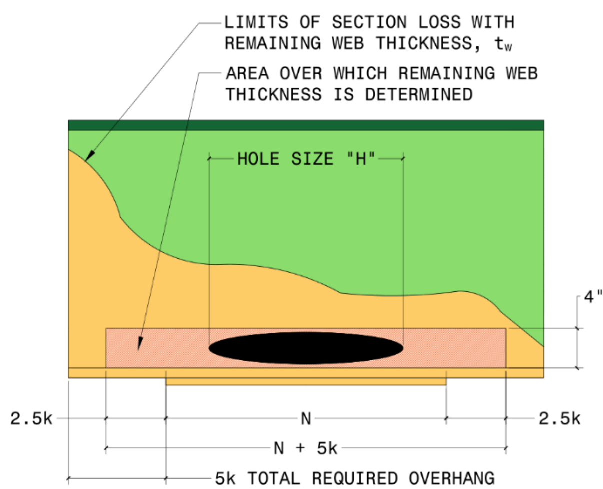

Figure 11. End of Beam Elevation Describing the Deteriorated Beam End (MassDOT 2020)

The calculation for the adjusted average web thickness in Equation 8 was also modified. It is presented in Equation 9 as:

$$t_{ave} = \frac{(N + 5k - H)t_w}{(N + 5k)}$$

Equation 9. MassDOT Average Web Thickness Equation (MassDOT 2020)

This modified version of the equation does not include the m factor presented in Table 5 and instead defaults back to the previous MassDOT equation rather than using the proposed values from the Tzortzinis study. Instead, if an overhang past the bearing of less than 5k is provided, then the *"5k"* term in the equation should be substituted with *"2.5k."* Similarly, the factors presented in Table 4 were also excluded from the MassDOT revision procedure and are shown in Equation 10 and Equation 11.

$$R_{n,yield} = F_y t_{ave}(2.5k + N)$$

Equation 10. MassDOT Corroded Web Yielding Capacity Equation (MassDOT 2020)

At interior-pier reactions and for beam end reactions applied at a distance from the end of the member that is greater than or equal to d/2:

$$R_{n,crip} = 0.8t_{ave}^2\left[1 + 3\left(\frac{(N - H)}{d}\right)\left(\frac{t_{ave}}{t_f}\right)^{\mathbf{1.5}}\right]\frac{\sqrt{EF_y t_f}}{t_{ave}}$$

Otherwise:

$$R_{n,crip} = 0.4t_{ave}^2\left[1 + 3\left(\frac{(N - H)}{d}\right)\left(\frac{t_{ave}}{t_f}\right)^{\mathbf{1.5}}\right]\frac{\sqrt{EF_y t_f}}{t_{ave}}, \text{when N/d } \leq 0.2$$

$$R_{n,crip} = 0.4t_{ave}^2\left[1 + \left(\frac{4(N - H)}{d} - 0.2\right)\left(\frac{t_{ave}}{t_f}\right)^{\mathbf{1.5}}\right]\frac{\sqrt{EF_y t_f}}{t_{ave}}, \text{when N/d} > 0.2$$

Equation 11. MassDOT Corroded Web Crippling Capacity Equation (MassDOT 2020)

These equations are unchanged from the previous versions of the MassDOT Bridge Manual and do not reflect the Tzortzinis study's modifications.

2.7 Darwin – Web Openings in Steel Beams

Outside of research specifically targeting corroded beam capacity, studies have been conducted regarding the effects of web openings in steel beams. Professor David Darwin completed such analyses at the University of Kansas to determine composite beams' capacity with web holes through the steel sections, such as those used to route utilities through buildings. In his 1988 study, Darwin proposed a method for determining the shear capacity of beams with web openings by summing the beam sections' individual shear capacities above and below the opening (Darwin and Donahey 1988). However, the composite concrete component was not expected to be utilized for the current study. Thus, Darwin's calculation for the maximum shear capacity of the non-composite bottom tee may be used (Equation 12).

$$V_b(max) = V_{pb}\left(\frac{\lambda\sqrt{3}}{\sqrt{3}+\frac{a_0}{s_b}}\right)$$

Equation 12. Maximum Shear Capacity Equation (Darwin and Donahey 1988)

Where:

V_b (max) = Maximum Shear Capacity of the bottom tee

V_{pb} = Plastic Shear Capacity of the bottom tee

λ = Constant used in linear approximation of von Mises yield criterion ($\sqrt{2}$=1.414)

a_0 = Length of the opening

s_b = Height of the bottom tee

The plastic shear capacity is defined in Equation 13 as:

$$V_{pb} = \frac{F_y}{\sqrt{3}} t_w s_b$$

Equation 13. Plastic Shear Capacity Equation for the Bottom Beam Tee (Darwin and Donahey 1988)

Where:

F_y = Yield Strength of steel

t_w = Web Thickness

This equation can also be applied to the top tee in the case of a non-composite beam, where the top tee's height would replace the value of s_b. The total maximum shear capacity would then simplify to Equation 14:

$$V(max) = F_y t_w \lambda \left(\frac{s_b}{\sqrt{3} + \frac{a_0}{s_b}} + \frac{s_t}{\sqrt{3} + \frac{a_0}{s_t}} \right)$$

Equation 14. Simplified Shear Capacity Equation for a Non-Composite Beam (Darwin and Donahey 1988)

Where:

s_t = Height of the top tee

2.8 AASHTO LRFD Shear Capacity Calculations

The shear capacity of corroded steel bridge beams may be determined using AASHTO (Equation 15 and Equation 16) and AISC (Equation 17) calculations using modified section properties. The VDOT Bridge Load Rating and Evaluation Manual calls for using AASHTO LRFR code to evaluate the remaining capacity in existing structures. The AASHTO calculations for shear capacity of unstiffened webs are found in section 6.10.9.2 of the AASHTO LRFD Bridge Design Specifications and are as follows (AASHTO 2017):

$$V_n = CV_p$$

Equation 15. AASHTO Nominal Shear Capacity Equation (AASHTO 2017)

Where:

V_n = nominal shear capacity

C = Ratio of shear buckling resistance to shear yield strength

V_p = plastic shear capacity

Φ_v = 1.0

$$V_p = 0.58 F_y D t_w$$

$$\text{if } \frac{D}{t_w} \leq 1.12 \sqrt{\frac{Ek}{F_y}} \text{ then } C = 1.0$$

$$\text{if } 1.12 \sqrt{\frac{Ek}{F_y}} < \frac{D}{t_w} \leq 1.40 \sqrt{\frac{Ek}{F_y}} \text{ then } C = \frac{1.12}{(\frac{D}{t_w})} \sqrt{\frac{Ek}{F_y}}$$

$$\text{if } \frac{D}{t_w} > 1.40\sqrt{\frac{Ek}{F_y}} \text{ then } C = \frac{1.57}{(\frac{D}{t_w})^2} * \frac{Ek}{F_y}$$

Equation 16. Plastic Shear Capacity Equation (AASHTO 2017)

Where:

D = Web depth

t_w = Web thickness

k = Shear buckling coefficient (= 5 if unstiffened, actual 5.35)

The AASHTO equations for shear capacity apply to the AASHTO critical section for shear, defined as an applied load located a beam height away from the support.

2.9 AISC Shear Capacity Calculations

The equations used in chapter G of AISC 360-16 to calculate shear capacity are shown in Equation 17 (AISC 2016):

$$V_n = 0.6F_yA_wC_v$$

$$\text{when } \frac{h}{t_w} \leq 1.10\sqrt{\frac{k_vE}{F_y}} \text{ then } C_{v=}1.0$$

$$\text{when } 1.10\sqrt{\frac{k_vE}{F_y}} < \frac{h}{t_w} \text{ then } C_{v=}1.10\frac{\sqrt{\frac{k_vE}{F_y}}}{\frac{h}{t_w}}$$

Equation 17. Nominal Shear Capacity Equation with Shear Strength Coefficients (AISC 2016)

Where:

A_w = Web area ($= dt_w$)

d = Web depth (for rolled shapes, the distance between flanges less the fillet)

t_w = Web thickness

k_v = Shear buckling coefficient (= 5.34 for webs without transverse stiffeners)

C_v = Web shear strength coefficient

h = The clear distance between flanges

Φ_v = 0.9

Note that the web thickness used in these formulae is for webs of uniform thickness, so to apply it to a corroded section, an assumed thickness must be used.

2.10 VIRTIS Procedure for Beam Section Losses and VDOT Load Rating

A 2007 VDOT document describes a process for evaluating structural steel members with holes in the web specifically for application in bridge rating for previously used AASHTOWare software VIRTIS which has since been replaced by BR|R (VDOT 2007). This process uses defined percentages of remaining web and flange areas to establish an assumed cross-section. This percentage distributes the section loss by symmetrically reducing the web or flange thickness and using that reduced area to calculate section properties, which is a rough approximation, especially if the inspection data is imprecise. This same document also recommends comparing results to those from a VDOT sectional property Excel worksheet, which allows for more specific placement of holes in the web. This worksheet then compares VIRTIS's answers and another previously used rating analysis program known as PCBars or BARS. If the difference between the solutions is greater than 5%, then the document suggests reducing the percentage thickness reduction value until the 5% threshold has been reached to better reflect the actual behavior of the beam in its specific corroded condition.

Information regarding corrosion included in inspection data varies significantly between reports. The National Highway Institute Bridge Inspector's Reference Manual includes a chapter describing the various forms of potential damage sources and types in addition to inspection methods (FHWA - Federal Highway Administration 2012). This section mentions visual and physical examination descriptions for corrosion and other steel defects. The physical examination section recommends using an inspection hammer or wire brush to remove corrosion buildup and remaining paint before taking measurements of the steel. Language in this section also vaguely prescribes the use of "a straight edge and a tape measure" or "calipers or an ultrasonic thickness gauge" to measure section loss due to corrosion. This ambiguity may result in less reliable measurements being recorded, resulting in more uncertainty in any capacity calculation using these values.

CHAPTER 3: Experimental Testing Methods

3.1 Specimen Acquisition and Selection

All the bridge beams used in this study were received through contact with several of VDOT's districts and residencies, whose ongoing maintenance work includes the replacement and disposal of retired bridge superstructures. For many of these beams, their availability was limited due to logistics concerning construction schedules and access to vehicles for hauling beams. Due to this limitation, deteriorated bridge beam candidates were briefly reviewed to determine if they were appropriate for the experimental testing. This assessment included in-person inspection when available, discussion with VDOT engineers, and review of available bridge inspection documents with VDOT permission. After a bridge was determined to show adequate corrosion damage for the study, beams were transported to the Thomas M. Murray Structures Laboratory at Virginia Tech. To maximize the pool of available beams to select from, nine total sets of bridge beams were delivered from which four beam ends from four of these bridges were selected and tested.

3.2 Specimen Matrix

Individual beams were selected to represent a spectrum of section loss conditions and their web damage was ranked using the following qualitative scale: low, medium-low, medium-high, and high. Beams with attached stiffeners were not considered to exclude their effect on beam capacity and because many of the bridges in question throughout the Virginia inventory do not have bearing stiffeners. The initial selection and damage ranking of these specimen conditions was made visually according to apparent section loss but was further quantified using more precise measurements after cleaning the beams. Each beam set included four beams of identical beam shape, except for the W16x45 beams. Five of these beams were tested due to the original four selected beams not fully encompassing the previously mentioned range of damage types.

These four test beam groups total 17 specimens, which are included in Table 6 below, along with their nominal web thickness and minimum average web thickness. These minimum average web thicknesses, which were used to calculate the remaining capacity, were determined by averaging the web thickness measurements over the beam height at the cross-section with the most section loss. The process of taking these measurements is further defined at the beginning of the Large-Scale Flexural Tests section of the Results and Discussion. Additionally, each beam was given a designation, which is how the beams are referred to throughout the remainder of the report. The naming convention represents information about the specimen separated by dashes. The first number describes the test order as they were performed from 1 to 17, followed by the structural shape and height, and ends with abbreviations of the specimen's condition state. For example, beam 1-S8-L indicates that it was the first test completed, the beam was an S8 shape, and the web represents a specimen with low corrosion losses.

Table 6. Specimen Matrix for Steel Beam End Corrosion Flexural Tests

Specimen Number	Beam Shape	Beam Designation	Web Damage Condition	Beam Depth (in)	Nominal Web Thickness (in)	Minimum Average Web Thickness (in)	% Thickness Remaining
1	S8x18.4	1-S8-L	Low	8.0	0.271	0.271	99.8%
2		2-S8-ML	Medium-Low			0.225	83.1%
3		3-S8-MH	Medium-High			0.126	46.4%
4		4-S8-H	High			0.125	46.0%
5	W10x26	5-W10-L	Low	10.3	0.260	0.256	98.3%
6		6-W10-ML	Medium-Low			0.247	95.0%
7		7-W10-MH	Medium-High			0.191	73.6%
8		8-W10-H	High			0.193	74.3%
9	W16x45	9-W16-L	Low	16.1	0.345	0.261	75.7%
10		10-W16-ML	Medium-Low			0.324	93.9%
11		11-W16-MH	Medium-High			0.308	89.3%
12		12-W16-H	High			0.330	95.6%
13		13-W16-L(A)	Low Alternate			0.337	97.6%
14	W21x62	14-W21-L	Low	21.0	0.400	0.387	96.7%
15		15-W21-ML	Medium-Low			0.364	91.0%
16		16-W21-MH	Medium-High			0.344	86.1%
17		17-W21-H	High			0.294	73.5%

The four specimen web damage conditions were based on existing VDOT specifications for steel corrosion condition states, found in the VDOT Supplement to the AASHTO Manual for Bridge Element Inspection shown previously in Figure 1 (Virginia Department of Transportation 2016). The Low

Specimen Condition corresponds to the Good Condition State -1; Medium-Low corresponds to the Fair Condition State – 2; Medium-High corresponds to the Poor condition state - 3, and High corresponds to the Severe condition state - 4. However, because of specimen availability not every beam set included a completely ideal range of corrosion damage. A beam with damage closer to a higher or lower condition state was selected to fill the gap in these cases. Justification for the chosen specimen conditions is discussed further in this section.

3.3 Specimen Preparation

Each beam was prepared before testing to remove existing corrosion and paint on the surfaces that were to be analyzed during testing. Oxidized steel layers adhering to the beam surface were initially removed using a chisel or a Mason hammer to remove oxidized steel from the base metal. Initial paint removal was then performed using Dumond Peel Away®, an alkaline paint removal system that chemically stripped layers of paint from the beam surfaces. One of the significant issues with this method was the necessary precaution to avoid lead particulate poisoning and spread due to the unknown makeup of the existing paint on the beams. This process required much certification and monitoring to achieve, which significantly delayed progress on specimen preparation. It also needed a full breadth of personal protective equipment, including a respirator, chemical goggles, nitrile gloves, and a full Tyvek suit to prevent injury or harm to the operator. Additionally, an AllSource VacBlast abrasive blasting system was attempted for paint removal. The required amount of air pressure exceeded what was provided by the laboratory's portable air compressor and could not be used outside of the laboratory where the beams were stored. Finally, a more successful alternative method of paint and corrosion removal was proposed, which was using a Desco Model 40 pneumatic needle scaler.

The needle scaling tool uses multiple fine metal needles to abrade the beam's surface to remove layers of paint and oxidized metal from the base metal and capture the particulate using suction from a vacuum. This method was the most effective surface preparation available due to the speed of removal, the enclosed nature of the removal process, and its ability to clean uneven surfaces, which was necessary for the corroded metal of the specimen webs. Furthermore, the process could be used with a PowerBOSS 3250 gasoline generator and transported to the lot where the beams were stored. This portability was necessary due to limitations on available space at the structures lab, as paint removal could be conducted at various locations without allocating a specific area around the lab building. An example of this configuration is shown in Figure 12. The needle gun is shown connected to the lab's DeWalt 15 Gallon Workshop compressor by the green pneumatic hose and a Desco Dominator 6E ultra-low particulate air (ULPA) filtered vacuum to collect the debris created by the gun.

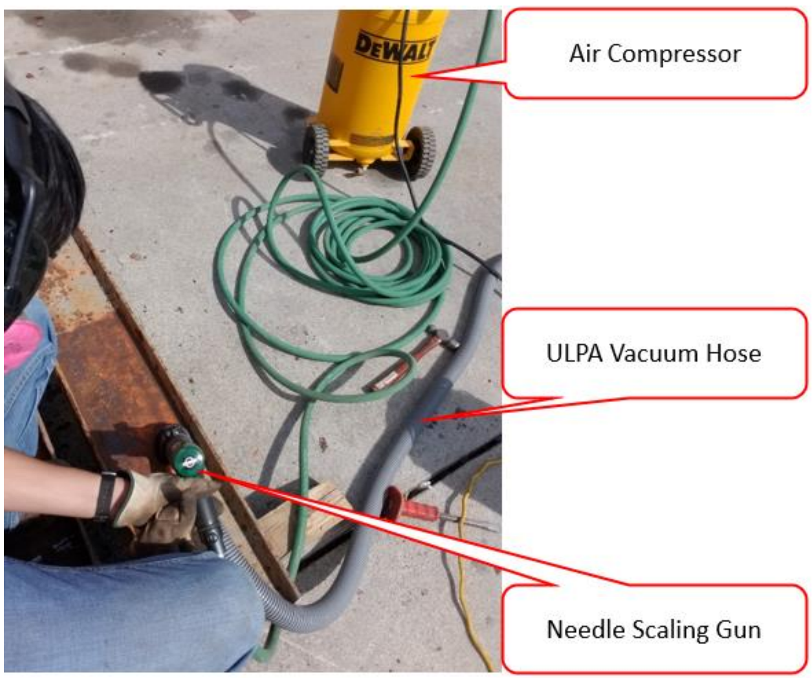

Figure 12. Pneumatic Needle Scaler Configuration

3.4 Test-Setup and Instrumentation

The testing setup consisted of a 3-point beam loading test, with a single applied load near the support to determine the shear capacity. The tests were carried out on a self-reacting steel load frame, resting upon two W36x160 reaction beams. Test specimens were supported at the north support by a 1/2-inch-thick by 12-inch-long neoprene rubber bearing pad with width equal to the flange width of the test specimen, placed on top of a W14x90 coped beam running across the reaction beams. The south support consisted of a 2.5-inch-thick by 12-inch-long by 16-inch-wide neoprene pad placed on a W21x68 beam running across the reaction beams. The neoprene pads were used to better replicate the in-field conditions of the specimens and were chosen in favor of roller bearings due to the minimal translational displacement resulting from the near bearing loading point. The load frame was made up of two W12x53 columns connected by two coped W18x86 crosshead beams, which supported a 200-ton Enerpac RR20013 hydraulic cylinder used for loading. This cylinder was connected to a 10,000-psi Enerpac Hushh Pump with hoses equipped with ball-type quick couplings and a hydraulic tee adapter connected in series to allow for pressure readings taken using a pressure transducer. Figure 13 and Figure 14 show diagrams of the load frame configuration from the front and side view.

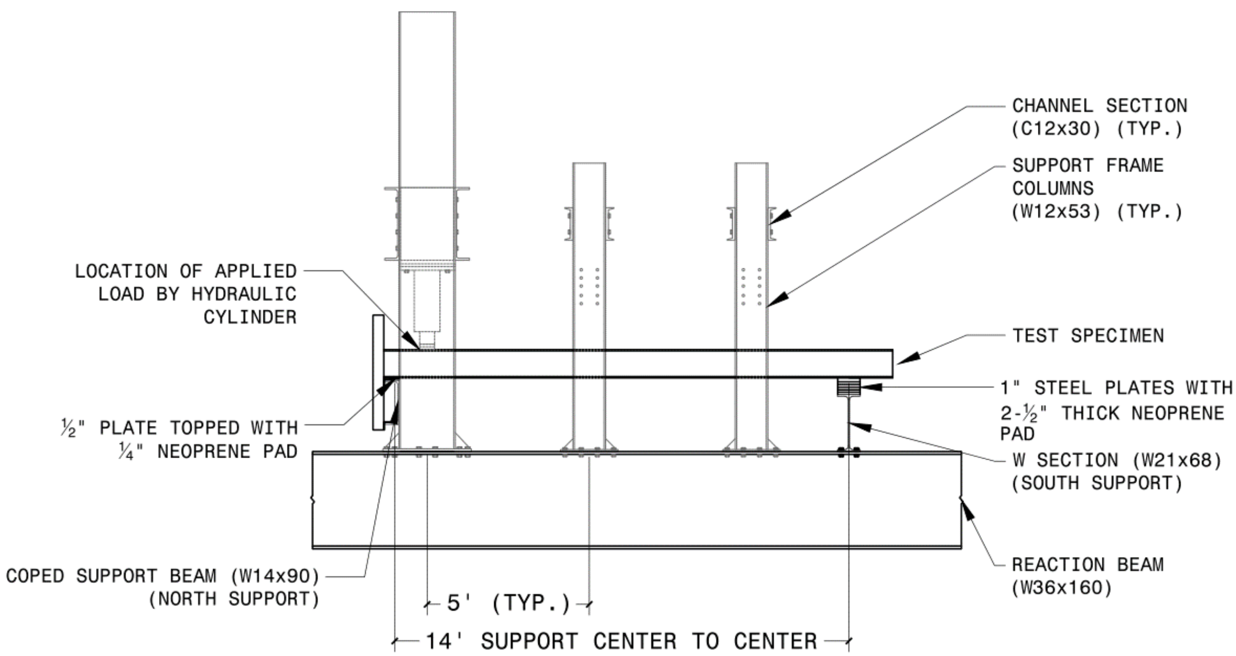

Figure 13. Elevation View of Full-Scale Beam Testing Configuration

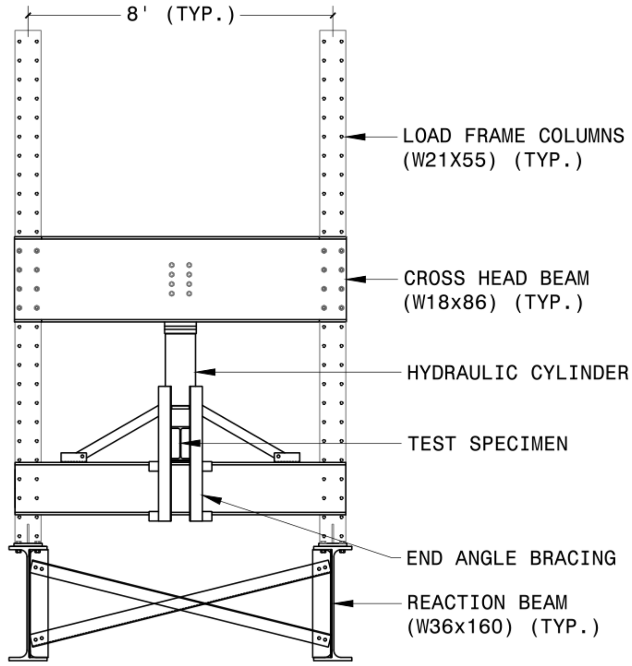

Figure 14. Transverse Elevation View of Full-Scale Beam Testing Configuration

The coped support beam shown in Figure 13 was moved to sit on the top flange of the reaction beams during the W16x45 and W21x62 load tests so that the load could be positioned further from the bearing. As a result, the 1-inch steel plates on the south support were moved to the north support to level the test specimen. Additionally, lateral supports were added to brace the beams at 5-foot intervals from the loading point and at the beam end to prevent lateral torsional buckling and ensure that the beam would fail in shear. The beam end lateral bracing system first shown in Figure 14 was comprised of a system of welded angles clamped to the loading frame using heavy duty bridge clamps. The beam end bracing is shown in Figure 15, with the clamping locations marked with red circles. This configuration was easily reassembled between beam tests and adjusted to various beam widths while providing enough stability to prevent beam torsion at the bearing during testing.

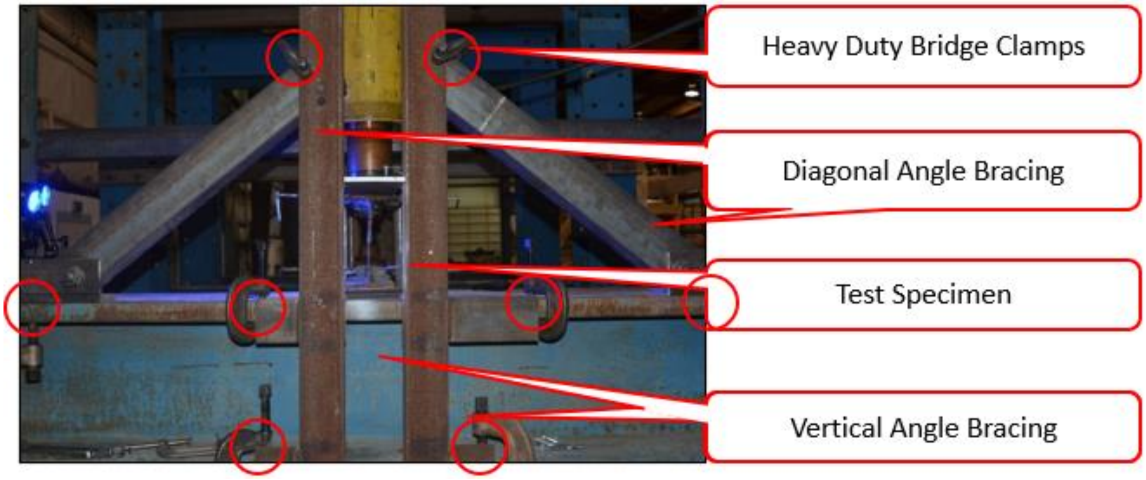

Figure 15. Beam End Bracing Configuration

Beams were loaded at varying distances from the support due to variation in beam size and the decision to move the load further for taller beams to maintain a similar shear state between beam sizes. This is further discussed in the Specimen Discussion section; however, Table 7 provides the distances between the loads and the edge of the north support. The distance between the load and the edge of the support was chosen instead of the distance to the midpoint of the support because loads applied to the beams during testing caused many of the specimens to lift at the beam end, only contacting the support at the edge. This behavior can be seen in an advanced state in Figure 16 where significant amounts of deformation has caused clearly visible lift of the beam end. Figure 17 shows a more detailed view of the north support, including the bearing pads used, the positions of the lateral support structures, the beam height shown as 'h', and the distance from the load to the support shown as 'd'.

Table 7. Test Specimen Distances Between Applied Loads and Edge of Support

Test Set	Distance Between Load and Support 'd' (in)
S8x18.4	4
W10x26	4
W16x45	16
W21x62	21

Figure 16. Example of Beam Lifting at End due to Applied Loads

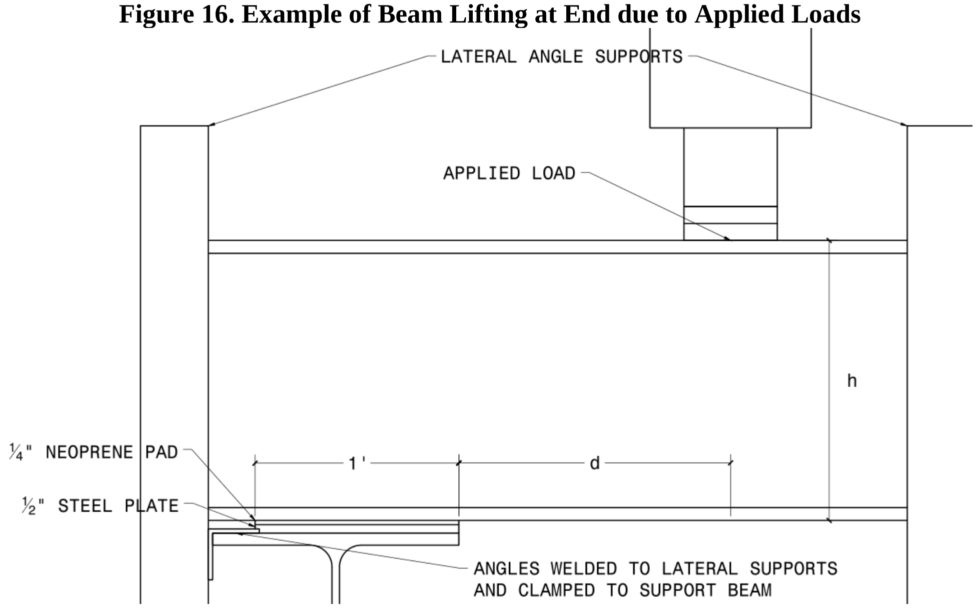

Figure 17. North Support View of Full-Scale Beam Testing Configuration

The data was collected using a Campbell Scientific CR6 data acquisition system paired with a KPS3050 Eventek DC power supply. Additionally, a Campbell Scientific SDM AO4A analog output module was used to communicate the applied loads from the data logger to the DIC system described further in this section. Figure 18 is an image of the data acquisition system configuration and its wiring. An Ashcroft G2 calibrated pressure transducer was connected to the hydraulic cylinder and used to determine the applied loads. The pressure transducer was initially calibrated using an FL300C 300-kip StrainSert compression flat load cell, which was, in turn, calibrated using a Forney compression testing machine. The relationship between the load and the pressure was recorded during this calibration step.

Additionally, a single string potentiometer was installed directly below the loading point to record the beams' vertical displacement during testing.

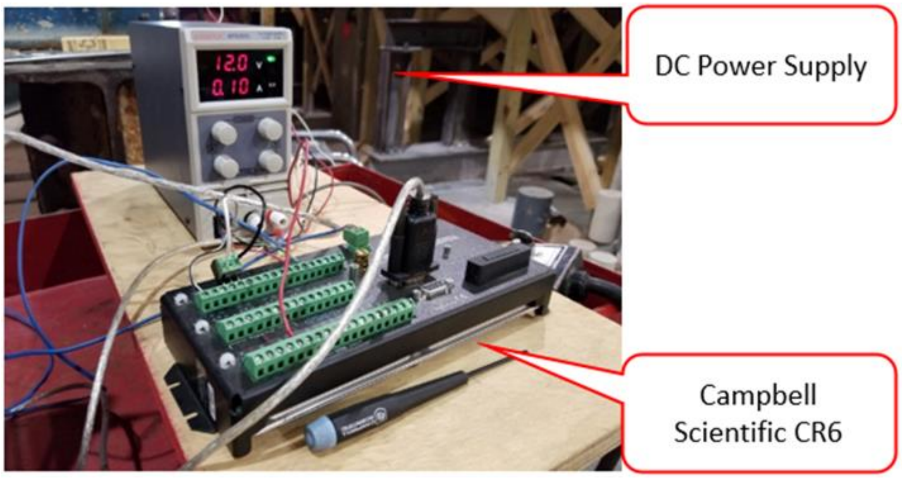

Figure 18. Campbell Scientific CR6 Data Acquisition System with DC Power Supply

Comprehensive strain fields of the beam webs were captured using an ARAMIS DIC system. This system replaced the need to use strain gauges by instead making use of an applied stochastic pattern. This pattern's application was a simple process. A primary coat of white spray paint was applied to the beam web to create a uniform base layer. The white paint was allowed to dry before a randomized series of black dots were painted overtop by applying a small amount of pressure to the nozzle of a black spray paint can. Figure 19 is an example of the system in use. The camera system projects a bright blue polarized LED light on the stochastic pattern, which was photographed throughout the loading process using a stereoscopic camera arrangement to identify displacements of individual points on the face of the webs. It was essential to use contrasting paint colors (black and white in this case), high-resolution cameras, and constant bright lighting to ensure that the images taken were clear and consistent. The quality of these images assured that the randomized points could be tracked between separate photographs taken throughout the loading process.

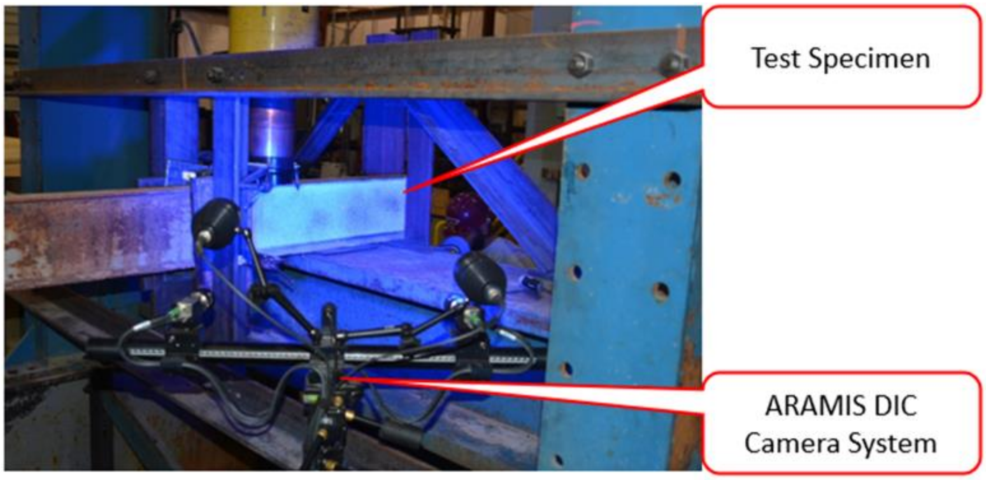

Figure 19. Digital Image Correlation Camera Scanning a Beam

Using the GOM Correlate software, the images taken were then converted into a surface model with a strain field based on the location of each point on the web before and during loading. This method removed the need to use an extensive series of strain gauges or multiple strain gauge rosettes that are time-consuming to apply. Additionally, the DIC system was advantageous because strain gauges do not work well on uneven surfaces such as corroded metal.

Before each load test, the GOM software was used to convert images taken on each side of the undeformed beams into a 3D mesh, which was then referenced for the original beam's section loss measurements. These preliminary scans were achieved initially by taking images on both sides of the beams and marking five points where no corrosion had occurred on either side of the web, typically towards the upper flange where moisture did not accumulate during the bridge's service life. This process formed two separate meshes representing each side of the web. The marked points were then matched in the 3D point cloud, and mesh processing software CloudCompare was used to create a plane around which the mesh objects could be oriented. One of the meshes was then translated perpendicularly to the plane by a distance equal to the uncorroded web's thickness to create a model of the corroded web, which included both section loss from both sides of the web. This method was used for the first four beams; however, after gaining a better understanding of the DIC system, a more efficient process was determined and used for all the following specimens.

The second method utilized a wooden board marked with five target dots and clamped to the top flange such that the DIC cameras could see the targets from either side of the beam. Thus, by matching the five marker points using external software like CloudCompare or within the GOM software, a single web mesh could be generated with relative ease and more certainty of the accuracy of measurements made. Figure 20 illustrates the process where DIC images were taken of the east and west faces of the beam end. The target dot boards marked with red dashed lines were matched in 3D space to align the surface models in the center of the figure shown as bright green rectangles.

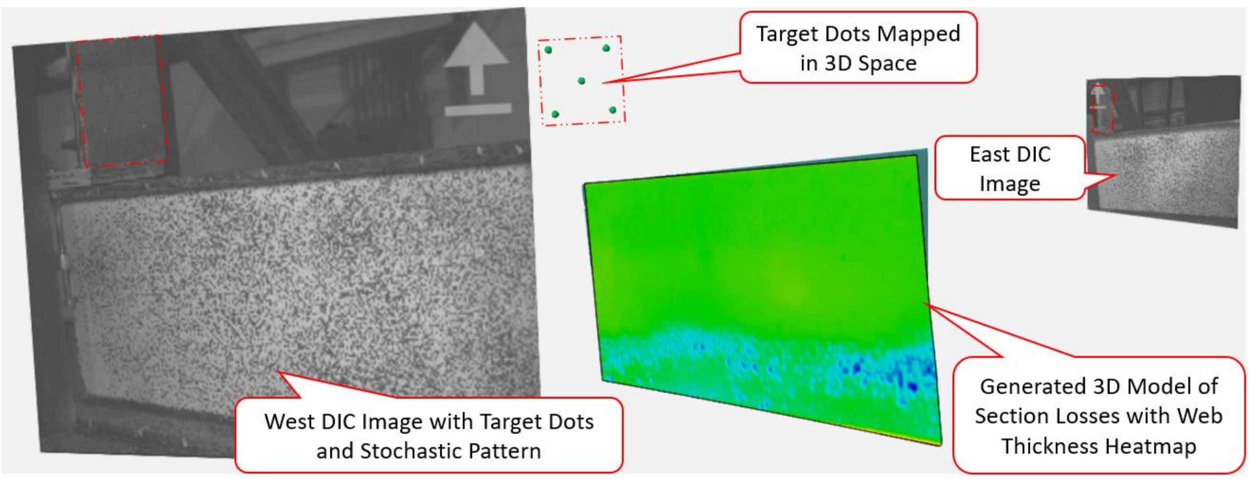

Figure 20. DIC Profile Scanning Using Target Dots

After the scanning process was completed, the deviation between the 3D surface models could be referenced to determine the remaining thickness of each beam digitally. Points were sampled from the 3D meshes at 0.5-inch intervals for the S8x18.4 and W10x26 beams and 1-inch intervals for the W16x45 and W21x62 beams. This difference in measurement interval was due to the ARAMIS software's limitations on the number of sample points placed on a single scan. These sample points were then exported to Microsoft Excel to create a matrix of thickness measurements referenced for web thickness data.

Steel coupons cut from the webs of each beam set were tested in tension according to ASTM E8 (ASTM International 2021). A 220-kip uniaxial load frame with a 22-kip load cell was used to load each specimen in tension. Each coupon was pulled until failure to produce a stress-strain curve used to determine the elastic modulus and steel grade of each beam set. The load frame was equipped with a load cell to record the applied tensile loads, and a non-contact laser extensometer was used to measure the coupon displacement during testing. Table 8 tabulates the calculated material properties received from these tests.

Table 8. Steel Properties from Beam Coupon Samples

Test	Elastic Modulus (ksi)	Tensile Yield Strength (ksi)
S8x18.4	29,027	38.7
W10x26	29,879	42.4
W16x45	29,665	50
W21x62	29,693	57.3

3.5 Specimen Discussion

3.5.1 Specimen Set 1: S8x18.4

The first set of beams tested were S8x18.4 beams and featured heavy section losses due to corrosion spread across the beam end webs. A total of nine beams from a single bridge were brought to Virginia Tech in August of 2018. Four beams with varying corrosion damage were selected for testing and assigned damage levels ranging from low to high. Images of these four beams with applied stochastic patterns are provided in Figure 21.

a. 1-S8-L

b. 2-S8-ML

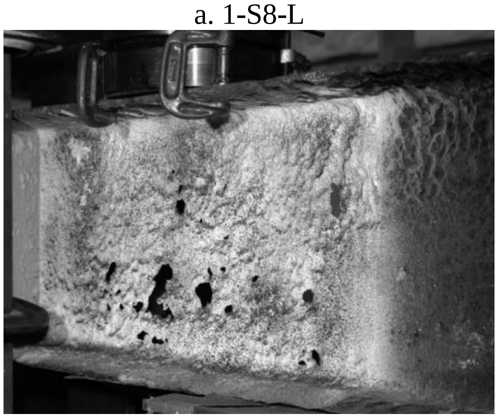

c. 3-S8-MH

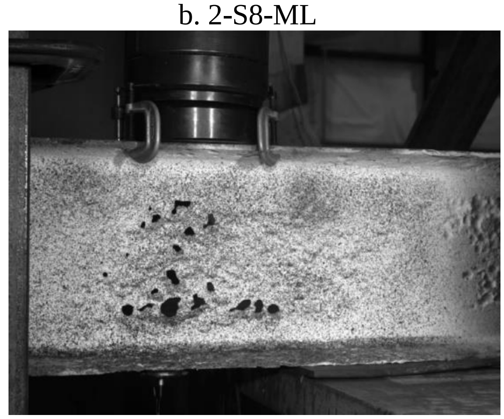

d. 4-S8-H

Figure 21. Photos of Beam End Specimens with Stochastic Patterns Showing Corrosion Damage

The first set of the deteriorated beams tested were the S8x18.4 shapes. These specimens came from a steel beam timber deck bridge, which had experienced severe localized corrosion on several beam webs and flanges. This deterioration was likely due to exposure to atmospheric moisture, roadway leakage, and moisture absorbed by the timber deck planks. Figure 22 shows an image of the first specimen tested after arrival at the Virginia Tech Structures Laboratory. The first specimen was nearly undamaged besides some paint coating failure and minor corrosion near the beam end and small portions of the lower flange. Initial preparation began with stripping the beams of paint at the tested end with a chemical paint removal treatment. An example of the first beam after cleaning is shown in Figure 23.


Figure 22. Image of Specimen 1-S8-L After Arrival at Lab


Figure 23. Specimen 1-S8-L Stripped of Paint

Specimen 2-S8-ML featured significantly more section loss than specimen 1-S8-L. The decision to use this beam as the Medium-Low specimen was driven by the presence of significant section losses without any through-web holes. As the study progressed, it became clear that the corrosion on specimens 2-S8-ML, 3-S8-MH, and 4-S8-H were unlike most patterns' characteristic of deck joint failure. The deterioration of a joint failure would follow the path of water runoff along the height of the beam end and near the bottom flange where water typically pools. The bridge this specimen came from was a steel beam timber deck design, making it likely that the wood absorbed and stored water, which was gradually released onto the web surface. Figure 24 shows an image taken of one of the bridge beams during service and illustrates this full-height web corrosion.

Figure 24. Example of Steel Beam Timber Deck Web Corrosion

The medium-high damage specimen 3-S8-MH showed more significant amounts of section loss spread across the entirety of the studied area, including through-web holes. Furthermore, the damage extends past the applied stochastic pattern towards the end of the beam. However, the specimen was positioned so that the applied load would be placed directly over most web holes to analyze the shear behavior around these defects.

Specimen 4-S8-H was selected as the high damage beam based on its holes' vertical positioning. If an analysis were to use the worst beam cross-section as the defining corrosion measure for 3-S8-MH, it would be taken at the center of the large 'L' shaped hole in the lower half of the web in Figure 21c. For specimen 4-S8-H, it would be taken along the column of holes directly below the load shown in Figure 21d.

In Figure 25, a comparative drawing of the cross-sections illustrates these holes' dimensions without the surrounding section losses. The ratio of hole to total web area between the flanges results in a 27% section loss for specimen 3-S8-MH and a 33% section loss for 4-S8-H. When creating the specimen matrix, this simplified cross-section was used as the rationale for assigning the condition rankings.

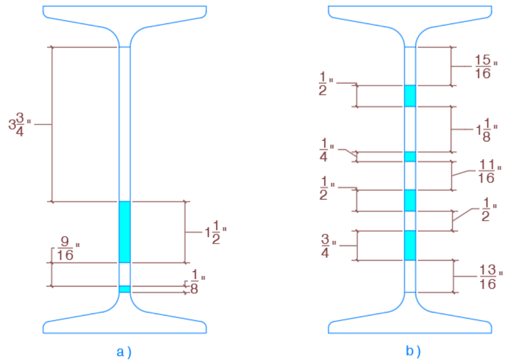

Figure 25. Comparison of Worst Cross-Section in a) 3-S8-MH b) 4-S8-H

3.5.2 Specimen Set 2: W10x26

The second set of beams tested were selected due to the limited availability of suitable beams between 10 and 12 inches in height. Specimen 5-W10-L represented the low damage configuration of the W10x45 beams and was selected from the available bridge beams due to its uniform profile. Despite this low damage designation, all of the beams in this set showed lower web corrosion and paint loss 3 inches above the bottom flange. Figure 26 shows photos of each of the corroded beam ends with applied stochastic patterns.

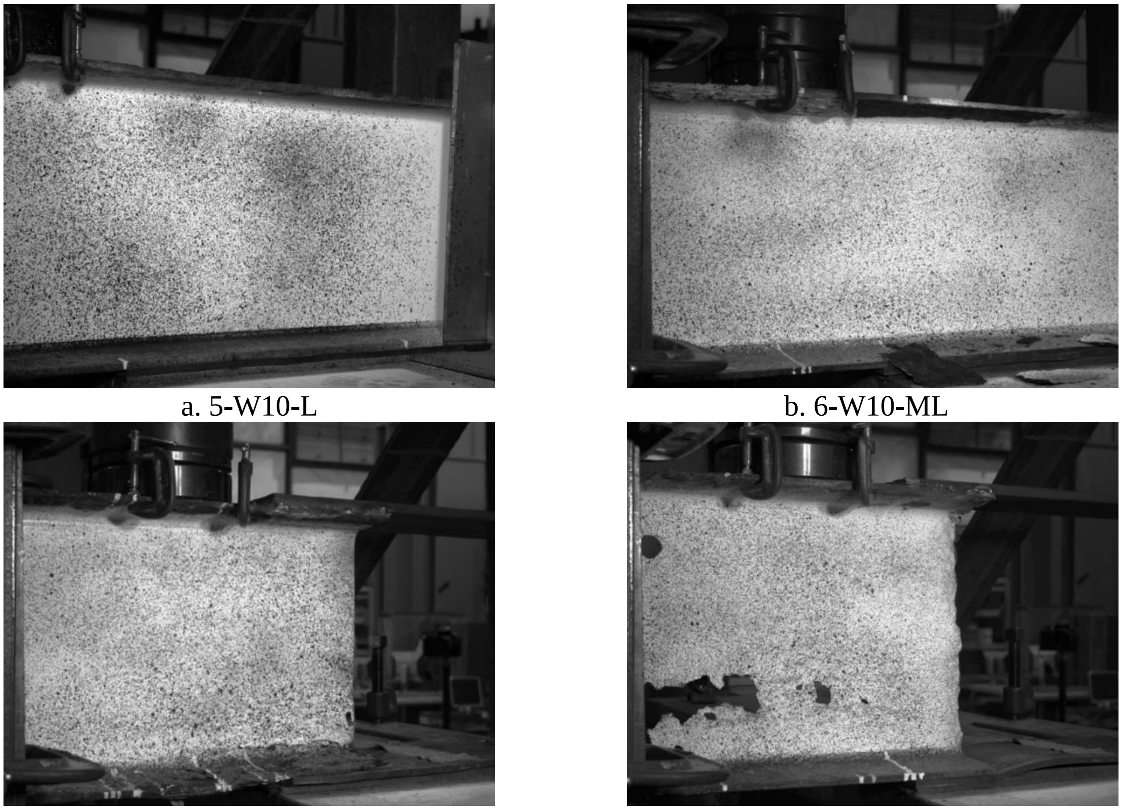

a. 5-W10-L b. 6-W10-ML

c. 7-W10-MH d. 8-W10-H

Figure 26. Photos of W10x26 Beam End Specimens with Stochastic Patterns Showing Corrosion Damage

Specimen 6-W10-ML also exhibited low corrosion but was selected due to noticeable localized pitting damage in the lower 3-inch band of corrosion mentioned before. This deep pitting continued intermittently throughout the length of the beam. This pitting caused various pinholes through the web; however, none were large enough for the DIC system to recognize. This is further discussed in the Results and Discussion section of Task 2.

The W10x26 beams selected did show significant corrosion; however, severe damage was only found on a single beam out of the set. This beam needed to serve as both the medium-high and high damage specimen to provide the necessary range of damage for the test matrix. First, specimen 7-W10-MH was loaded one foot from the beam's end. However, adjustments had to be made since the last 4 inches of the span are typically inserted between the bracing to the north of the support to prevent lateral torsion. A two-foot steel plate was welded for 6 inches along the top flange, shown at the top of Figure

26c. This plate would extend across the north support and sit between the two angle braces in place of additional beam length.

After testing the short section of specimen 7-W10-MH, the band saw in the lab was used to cut the deformed beam end off. An additional steel plate was welded to the top flange to test the high damage web section, specimen 8-W10-H. Since the section was from the same beam as the previous test, the continuous 3.5-inch longitudinal corrosion continues across this specimen. However, this beam also features a substantial through-web opening, shown in Figure 26d.

3.5.3 Specimen Set 3: W16x45

The third set of beams were W16x45 and came from a completed bridge replacement. Concerns with the bridge's remaining capacity due to corrosion made this an appropriate candidate for testing. Six beams with varying levels of damage were transported by a contractor to the Virginia Tech Structures Laboratory in February 2020. The low-damage specimen was selected from among the beams with minimal visible corrosion and intact coatings. Figure 27 shows images of all of the W16x45 corroded beam ends with applied stochastic patterns.

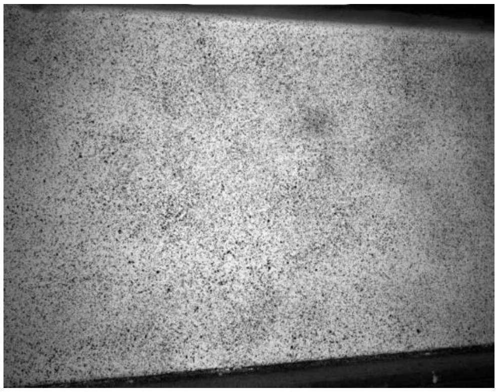

a. 13-W16-L(A)

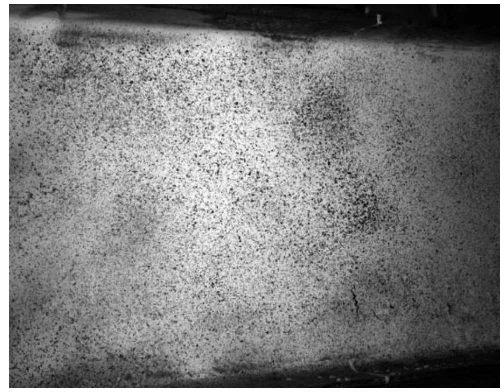

b. 9-W16-L

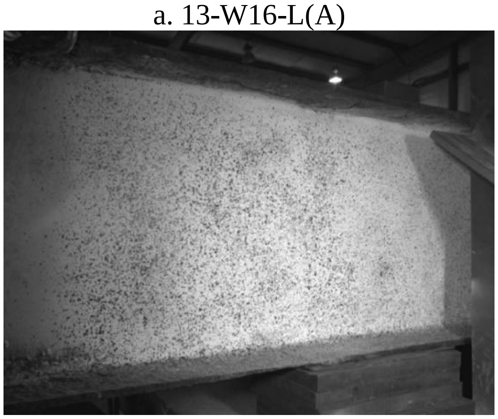

c. 10-W16-ML

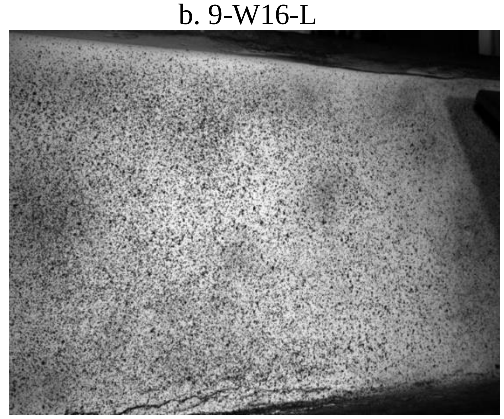

d. 11-W16-MH

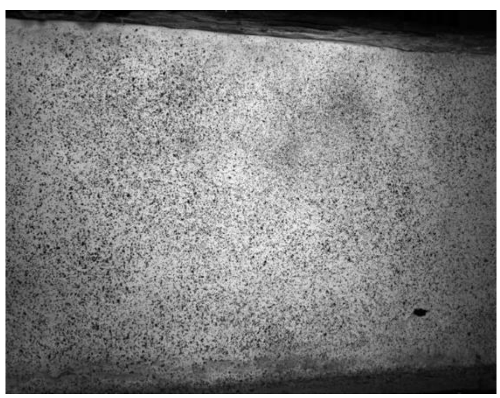

e. 12-W16-H

Figure 27. Photos of W16x45 Beam End Specimens with Stochastic Patterns Showing Corrosion Damage

The distance from the inner face of the support to the load point was changed from a set 4 inches to one beam height for the W16x45 beams than the S8x18.4 and W10x26 beams. This change was made because the distance between the center of the applied load and the support's face was targeted to be equal to the beam height. While the displacement data gathered in the first two beams accurately model the strain field behavior, the distance was too short to differentiate between shear and crushing action fully. Additionally, the original 4-inch spacing compresses the section of the beam initiating load transfer, making it more challenging for the system to identify failure initiation points. Thus, all the W16x45 beams were positioned so that the distance between the load and the face of the support was 16 inches.

Neither the medium-high nor high damage beams showed any form of through-web holes. Thus, these sections were instead selected from beams showing severe localized web thinning, typically in the lower three inches of the web directly above the bottom flange. The high damage specimen 12-W16-H showed similar corrosion patterns to the previous W16x45 beams; however, the lower web corrosion continues throughout its length.

While the initial test matrix called for four of each beam size with varying levels of damage, an issue was found during the testing of specimen 12-W16-H. This matter was that every beam end shared a common web end thinning, which occurred naturally due to the bridge's age. The thinning meant that even the specimens deemed as low and medium-low damage experienced this end thinning within at least the last foot of the web. It was decided that a new alternate low damage specimen should be tested to provide the full range of damage. One of the untested beams was cut one foot from the end to expose only the undamaged interior web to get a sample without any form of end thinning. This beam was given the designation 13-W16-L(A) and referred to as the low damage alternate specimen.

3.5.4 Specimen Set 4: W21x62

The W21x62 beam specimens were chosen from several candidate bridges selected due to the variation in corrosion damage visible on the web ends. However, four W21x62 beams were selected as the deepest specimens used in the testing matrix with the specific intent to select beams ranging from minimal to through-web damage. The original four beams were approximately 45 feet in length and delivered to the Virginia Tech Structures Lab gravel lot in January 2020. On arrival, four beam ends were selected to represent the four damage states of low, medium-low, medium-high, and high web corrosion. Figure 28 shows images of the four beam ends after application of the stochastic pattern prior to testing.

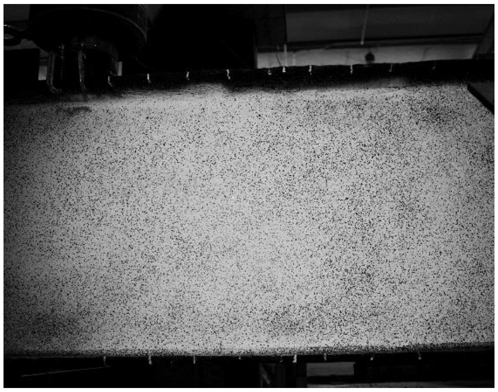

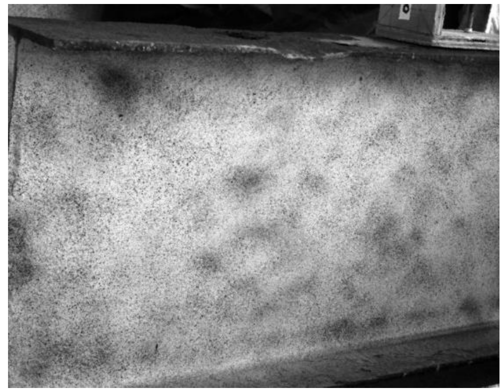

a. 14-W21-L b. 15-W21-ML

c. 16-W21-MH d. 17-W21-H

Figure 28. Photos of W21x62 Beam End Specimens with Stochastic Patterns Showing Corrosion Damage

Since the profile scans were conducted outside of the laboratory, the full height could be captured by adjusting the camera focus at a far distance. However, due to the increased beam depth of these specimens and the loading frame constraints, the full web could not be captured by the DIC system during these 21-inch beam tests. Figure 29 is an example of the DIC camera view for the high damage specimen and the initial testing scan. The flanges and web extremities are not visible.

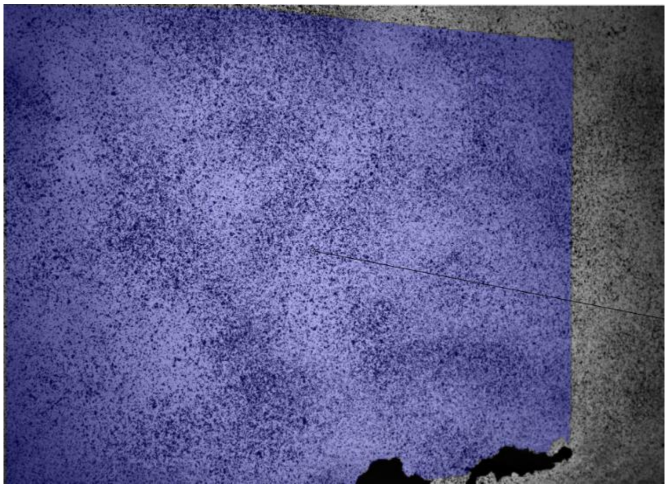

Figure 29. Specimen 17-W21-H Camera View and DIC Displacement Field

CHAPTER 4: Results and Discussion

4.1 DIC Scanned Beam Profiles

The following figures presented in this subsection represent the beam web thicknesses measured using the ARAMIS DIC system. These web measurements are given as heatmaps, which show changes in thickness as variations in color gradient ranging from blue representing little or no section loss to red, which denotes significant section losses. A scale is provided on each figure's right side, which defines the colors corresponding to varying web thicknesses. Additionally, some heatmaps include holes that could either signify through-web deterioration or, in some cases, errors made by the DIC capture for stochastic pattern recognition. The commentary accompanying each figure will differentiate between web holes and capture defects if this applies. Note that the web section captured using the DIC scans does not encompass the full beam length. Scans only depict the last 1 to 6 feet of the beam thickness out of 16 to 17 total feet of beam length. The captured sections were selected to include most of the significant web areas engaged during loading, typically between the applied load and the beam end. Each section ends with a table of average web thicknesses, which were created using the thickness measurements taken from these DIC beam scans.

Five methods of calculating the average web thickness were compared, including the minimum average, 45-degree average, area average, and 3- and 4-inch averages. The minimum average was determined by taking the average thickness over the web height at 0.5- or 1-inch intervals between the applied load and the north end of the beam and selecting the lowest value. The 45-degree average was determined by averaging the values in a straight line between the bottom of the web at the support's inner face and one beam height away at the top of the web. The area average was taken as the average of all the thickness matrix values between the interior face of the support and the applied load. Finally, the 3- and 4-inch averages were taken over the length of the support plus one beam height from the edge of the support. The five areas over which these measurements were compared and are illustrated in Figure 30 below.

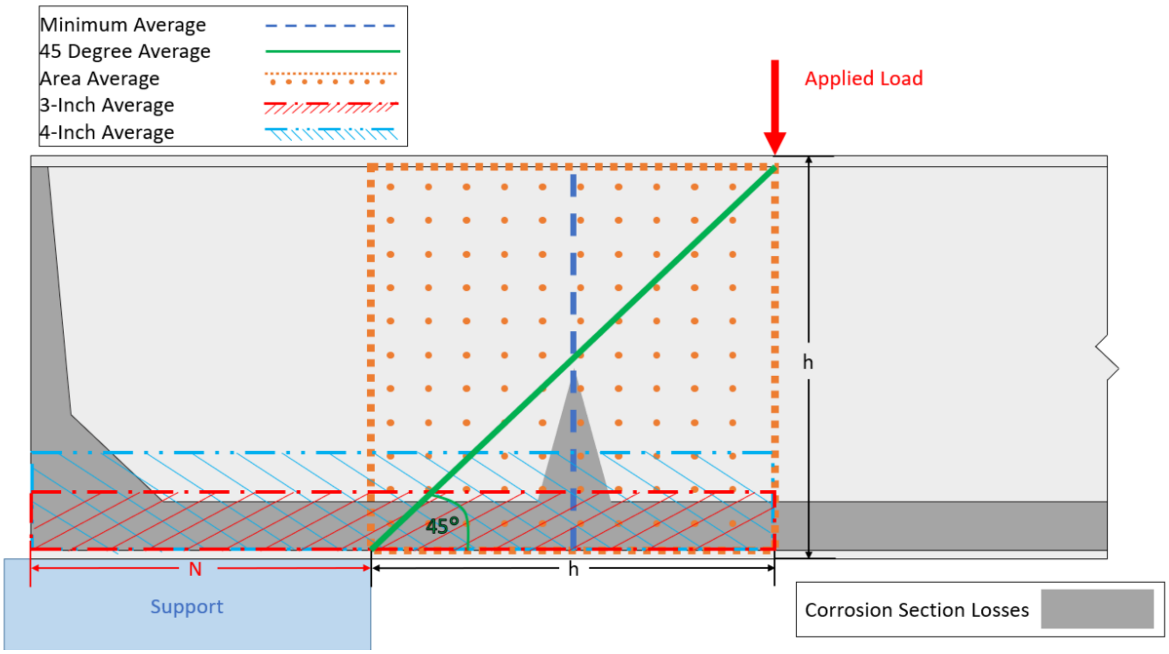

Figure 30. Methods for Calculating Average Web Thickness

To take these measurements, each DIC profile scan was sampled at 0.5-inch and 1-inch intervals as described in the Test-Setup and Instrumentation subsection of Task 2 to obtain the web thickness measurements across the face of each specimen's web. Figure 31 shows the DIC profile scan for specimen 2-S8-ML with points sampled at 0.5-inch intervals. Each box and leader correspond to the thickness measurement at each point on the web. These points were then exported as a thickness matrix and averaged over the areas described in Figure 30. For example, the measurements in the red box correspond to the minimum average cross-section. These values were averaged to get a thickness of 0.225 inches. The results of these averaged values are tabulated at the end of each specimen set section.

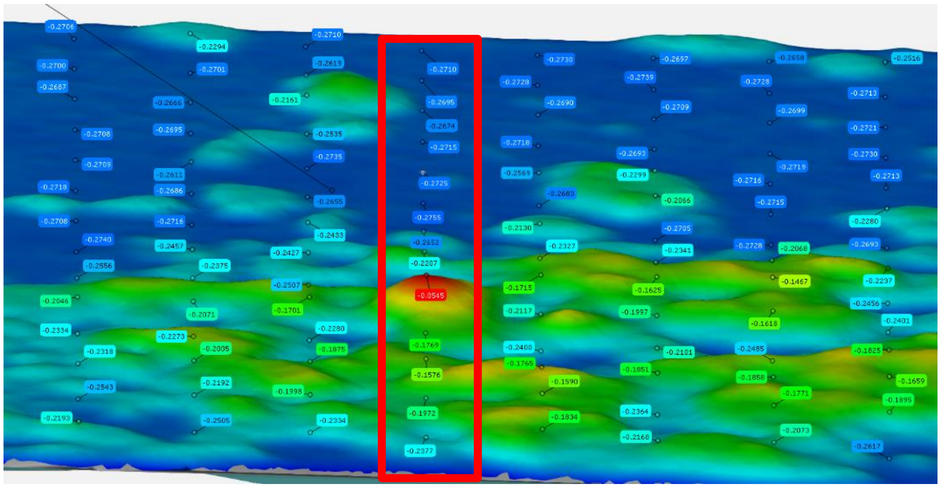

Figure 31. Example Web Thickness Profile Scan for Specimen 2-S8-ML with Points Sampled at 0.5-Inch Intervals

4.1.1 Specimen Set 1: S8x18.4 Beams

The first set of specimen scans are presented in Figure 32, where the applied load is shown at the top of each subfigure marked as a red arrow and the bearings at the bottom as black arrows. Note that although bearings appear to vary in length between specimens, all bearing lengths were kept at 12 inches but the black arrows only continue to the extents of the image taken cutting some of the bearing lengths short. This holds true for all of the remaining heatmaps as well.

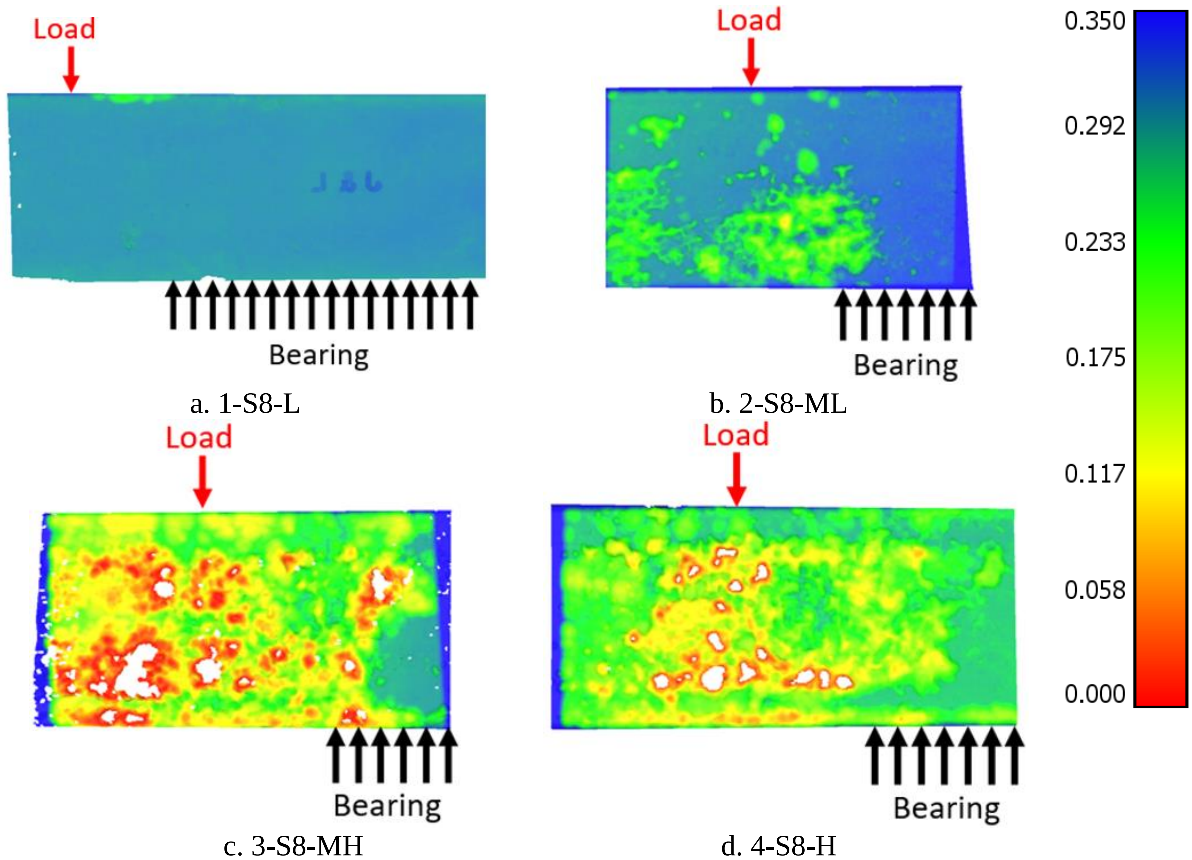

Figure 32. Heatmaps Showing Web Thickness of S8x18.4 Beam End Specimens (in)

Due to specimen 1-S8-L being the low damage beam, there is nothing of note about the surface profile outside of the fact that few noticeable section losses were present. In Figure 32a small amounts of section loss can be seen towards the top of the web in green. However, the depth of these deformities is approximately 0.06 inches in depth or slightly less than 1/16 inch. For this study's purposes, specimen 1-S8-L can be compared to a new beam as these losses equate to a highly localized 2% thickness loss. This type of damage is insignificant by the measure of any of the studies mentioned in the literature review. The multiple holes present on the figure's left, and right are due to the DIC camera failing to recognize points on the painted stochastic pattern.

The corrosion on specimen 2-S8-ML was scattered across the beam surface but was mostly targeted within the lower four inches of the web or the bottom half. Figure 32b shows the heatmap of the distance between the east and west profile, representing the thickness of the steel at that location. The green portion of the beam was approximately 10.4 inches in length, while the corrosion on the left side of the scan extended for about 8.9 inches. The DIC scan taken for the east profile was larger than the west profile because the camera angle used for the west image was suboptimal. The S8x18.4 beams were all scanned with the DIC system while in the load frame, which restricted the positions where the camera could be placed. Later profile scans were taken outside of the load frame for this reason.

Specimen 3-S8-MH showed two large holes in the lower web with multiple smaller holes scattered across the surface. Additionally, numerous deep corrosion pits were formed across the height and length of the beam. Most of the smaller holes in Figure 32c were again due to stochastic pattern recognition errors; however, web pinholes were present in the specimen.

Figure 32d shows the presence of multiple holes grouped in a 6-inch width band of the web, with most openings grouped near the bottom. Additionally, the orange areas demonstrate a 0.16-inch thickness loss, which surrounds the holes in this band. Further web thinning appears directly above the bottom flange. Following the issues with the profile scan of specimen 3-S8-MH, the scan of specimen 4-S8-H was taken outside of the load frame. The beam was elevated on concrete cinderblocks inside the lab so that the DIC camera could be moved freely without the need to take images from steep angles.

Table 9 shows the average areas for the S8x18.4 specimens for the measurements defined in Figure 30. Due to the highly irregular corrosion patterns present on the first test set, the measured beam averages were close for all five measurements. Due to the prevalence of holes throughout the beam height, the minimum cross-section average was typically the most conservative measure of section loss. However, the W10x26, W16x45, and W21x62 beam sets did not show similar results because their section losses were typically focused on the bottom 3 inches of the web.

Table 9. S8x18.4 Specimens Web Thicknesses Based on Different Methods

Specimen	Minimum Cross-Section	45-Degree Average	Area Average	3-Inch Average	4-Inch Average
1-S8-L	0.271	0.271	0.271	0.270	0.271
2-S8-ML	0.225	0.241	0.237	0.236	0.240
3-S8-MH	0.126	0.120	0.159	0.140	0.147
4-S8-H	0.125	0.162	0.172	0.170	0.220

4.1.2 Specimen Set 2: W10x26 Beams

The uniform corrosion in specimen 5-W10-L amounts to approximately 0.03 inches of thickness loss, which is the least of any of the W10x45 shapes tested. The deepest section losses appear as green on the heatmap in Figure 33a; however, they only represent about 0.05 inches of loss.

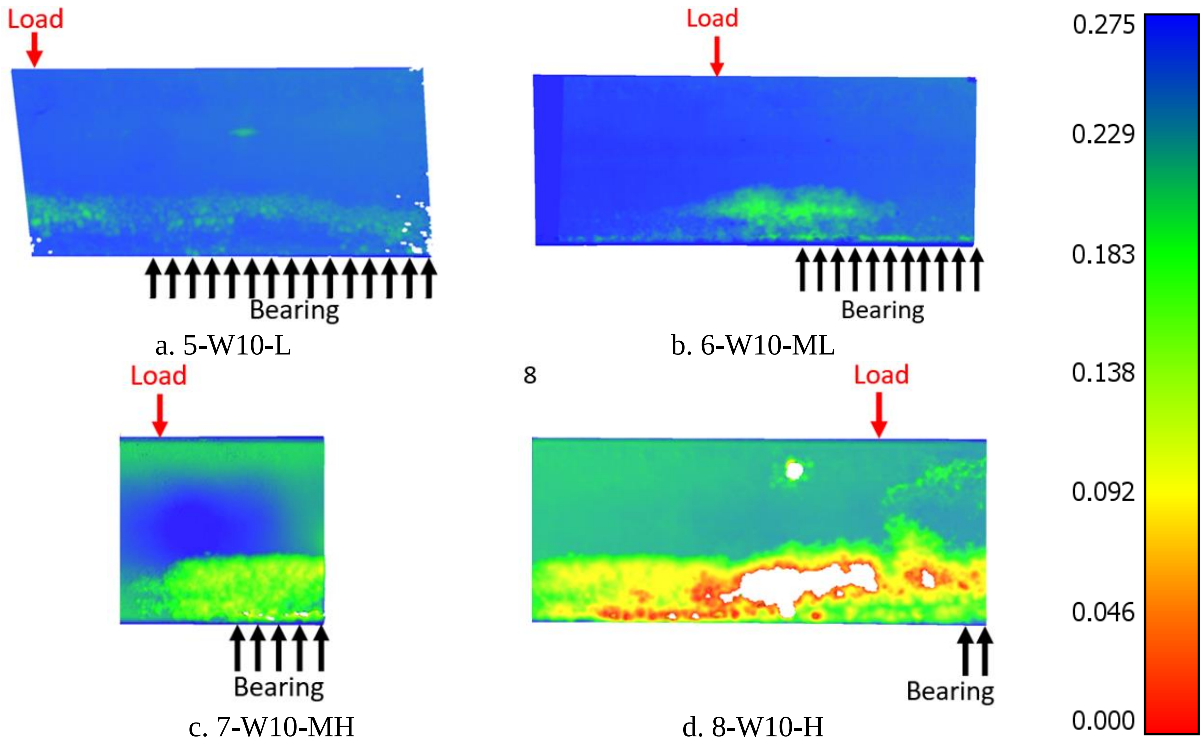

Figure 33. Heatmaps Showing Web Thickness of W10x26 Beam End Specimens (in)

The profile scan for specimen 6-W10-ML in Figure 33b showed that the pitting ranged from 0.06 to 0.11 inches of section loss, represented in green. The area of section loss measured 9.5 inches from edge to edge and 3 inches in height from the beam's bottom. Additionally, the strip of section loss directly above the bottom flange measures 0.5 inches in height and is continuous along the beam's length.

The corrosion-affected web area in specimen 7-W10-MH is shown in the bottom right corner of Figure 33c near the beam end. This damage comprises six through-web holes at 0.5 inches above the bottom flange and a relatively uniform section loss in the lower 3.5 inches of the web extending the full length of the stochastic pattern.

The most significant damage in specimen 8-W10-H is the large web opening extending 3.4 inches in width and 2.6 inches in height, the largest single hole in any test. However, the applied load was placed near the north end of this large hole. If the load was placed further south, the capacity would have been negligible due to the absence of any material capable of resisting shear forces. Two additional web holes are seen at the top of the web and to the right of the large web hole in Figure 33d. The circular upper hole was likely a bolt hole for a transverse stiffener to temporarily strengthen the beam before the bridge was replaced. Since this circular hole did not lie between the applied load and the support, it was not expected to contribute to the beam capacity reduction. Therefore, crack initiation was expected to begin either at the hole in the bottom right of Figure 33d or the pinhole directly to its right. The pinhole was too small for the DIC software to identify as a web opening. Instead, the DIC software modeled it as a severe section loss, visualized in Figure 33d as a red spot near the scan's right edge.

The average web thickness values presented in Table 10 show that the 3-inch average was the most conservative measure of the web thickness except in the case of specimen 8-W10-H due to the presence of large web holes located away from the bearing area, which is excluded from the 3-inch and 4-inch averages. Additionally, the 3-inch average did not include the entire height of the yellow section loss band in Figure 33d, which gave a much higher average than the other specimens.

Table 10. W10x26 Specimens Web Thicknesses Based on Different Methods

Specimen	Minimum Cross-Section	45-Degree Average	Area Average	3-Inch Average	4-Inch Average
5-W10-L	0.256	0.253	0.257	0.253	0.255
6-W10-ML	0.247	0.249	0.251	0.243	0.248
7-W10-MH	0.191	0.169	0.197	0.118	0.139
8-W10-H	0.193	0.199	0.205	0.213	0.154

4.1.3 Specimen Set 3: W16x45 Beams

The first W16x45 beam specimen 9-W16-L was used as the best damage condition despite showing extensive section losses at the beam end. However, the damage seen to the beam's right was not expected to contribute significantly to failure. The approximately 0.15-inch damage shown as green and yellow in Figure 34a extends towards the inner face of the support. While the shear test outcome will be discussed further in the section regarding the rendered strain fields, this test did not end with a diagonal web buckling between the applied load and the support as expected of a low damage beam. This irregular behavior prompted the fifth specimen to be tested, the low alternate specimen 13-W16-L(A).

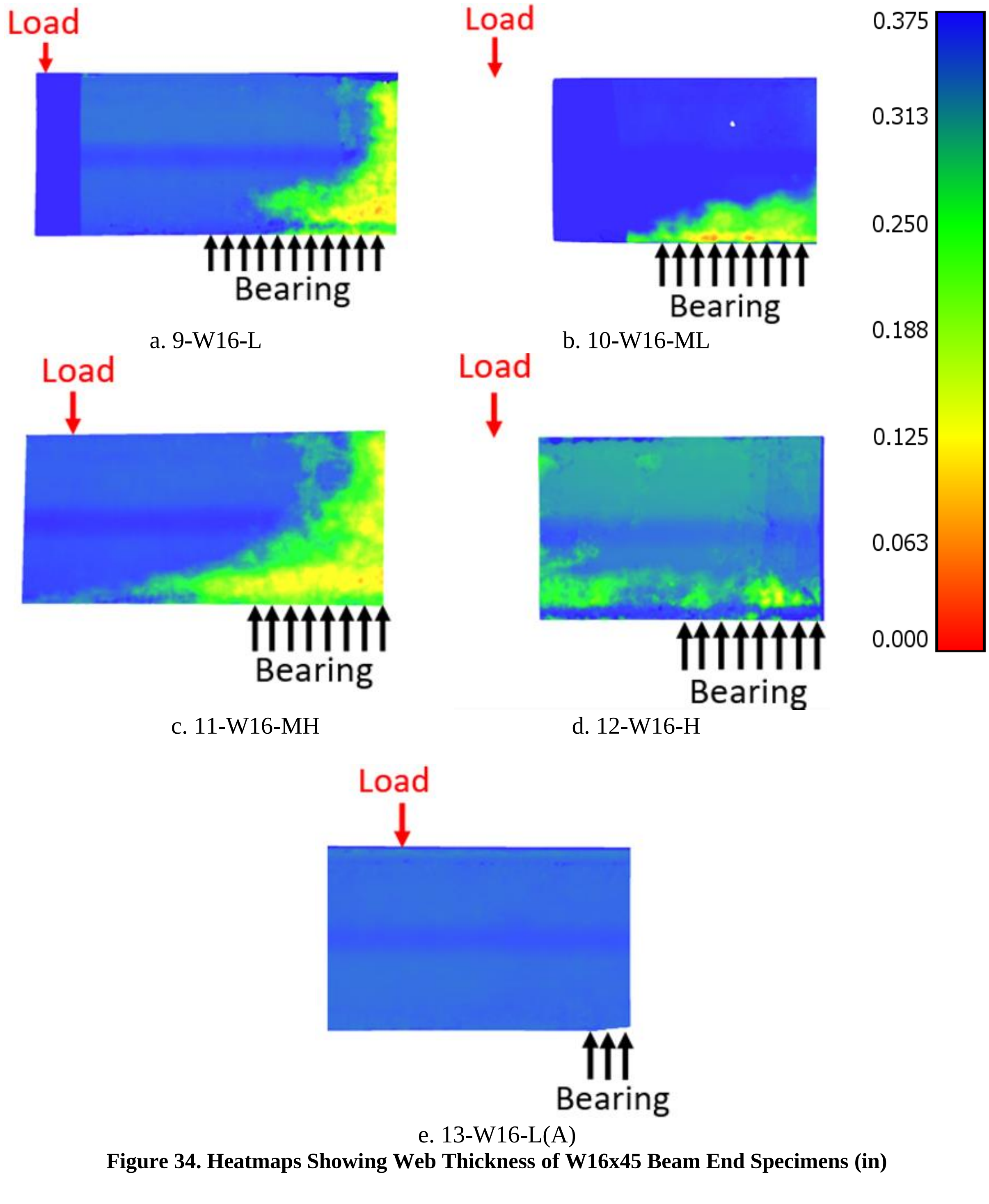

Figure 34. Heatmaps Showing Web Thickness of W16x45 Beam End Specimens (in)

Specimen 10-W16-ML was selected as the medium-low damage beam due to lower web section losses across its length, which is characteristic of corrosion patterns caused by water pooling. Damage to the W16 beams was relatively consistent with this lower web loss pattern, and the order of severity was selected based on the presence of localized damage. Upon visual inspection, 10-W16-ML showed relatively low amounts of section losses on both sides of the web, ranging from 0.04 to 0.2 inches of total web thickness loss, as shown in Figure 34b. Note that the web scans for specimen 10-W16-ML do not continue to the applied load location due to the range of the DIC camera. The red arrow representing the load has been placed approximately where the point load was applied during testing to the left of the scan.

The heatmap scan of 11-W16-MH shows similar damage to 9-W16-L, but the section losses continue further into the length of the beam. The total thickness loss amounts to 0.15 to 0.25 inches, which appears in the color range of green to yellow in Figure 34c.

The heatmap for specimen 12-W16-H shown in Figure 34d shows multiple locations of deep thickness losses in the lower 4.5 inches of the web. The comparatively low damage of this beam set's high damage specimen to the other beam sets is due to the stiffener repairs mentioned previously. As such, no beams with through web holes were available for testing.

Variation in the heatmap is at a maximum of 0.02 inches of thickness reduction in Figure 34 e. Compared to the rest of the beams, the 13-W16-L(A) surface profile was the most uniform because it was taken from the interior of the span from the retired bridge. As a result, it was expected that the capacity of 13-W16-L(A) would be closest to those calculated using AISC and AASHTO shear formulas for undamaged members.

The average web areas for the W16x45 beam ends presented in Table 11 again showed the 3-inch average as the most conservative estimate of the beam capacity due to the presence of the characteristic web corrosion pattern due to a leaking deck joint. In the case of specimens 9-W16-L, 10-W16-ML, and 11-W16-MH, the corrosion damage did not extend far past the support, and the 3-inch average was the only measure that was fully inside of areas with section loss and did not factor in any of the uncorroded beam surface.

Table 11. W16x45 Specimens Web Thicknesses Based on Different Methods

Specimen	Minimum Cross-Section	45-Degree Average	Area Average	3-Inch Average	4-Inch Average
9-W16-L	0.261	0.262	0.262	0.187	0.187
10-W16-ML	0.324	0.296	0.330	0.183	0.212
11-W16-MH	0.308	0.315	0.334	0.159	0.177
12-W16-H	0.330	0.335	0.337	0.301	0.306
13-W16-L(A)	0.337	0.337	0.338	0.337	0.337

4.1.4 Specimen Set 4: W21x62 Beams

Figure 35 shows the web thickness heatmaps of the W21x62 beams. Despite being the low damage specimen, 14-W21-L still shows a fair amount of section losses throughout its length. This was due to the history of the W21x62 bridge beams, as they were sourced from a storage yard and were sitting outdoors for several years before delivery to the Virginia Tech lab. All of the W21x62 beams had some section loss throughout them, but 14-W21-L had the least amount of damage. The heatmap in Figure 35a shows the extent of this section loss, ranging from 0.1 to 0.25 inches of total thickness reduction.

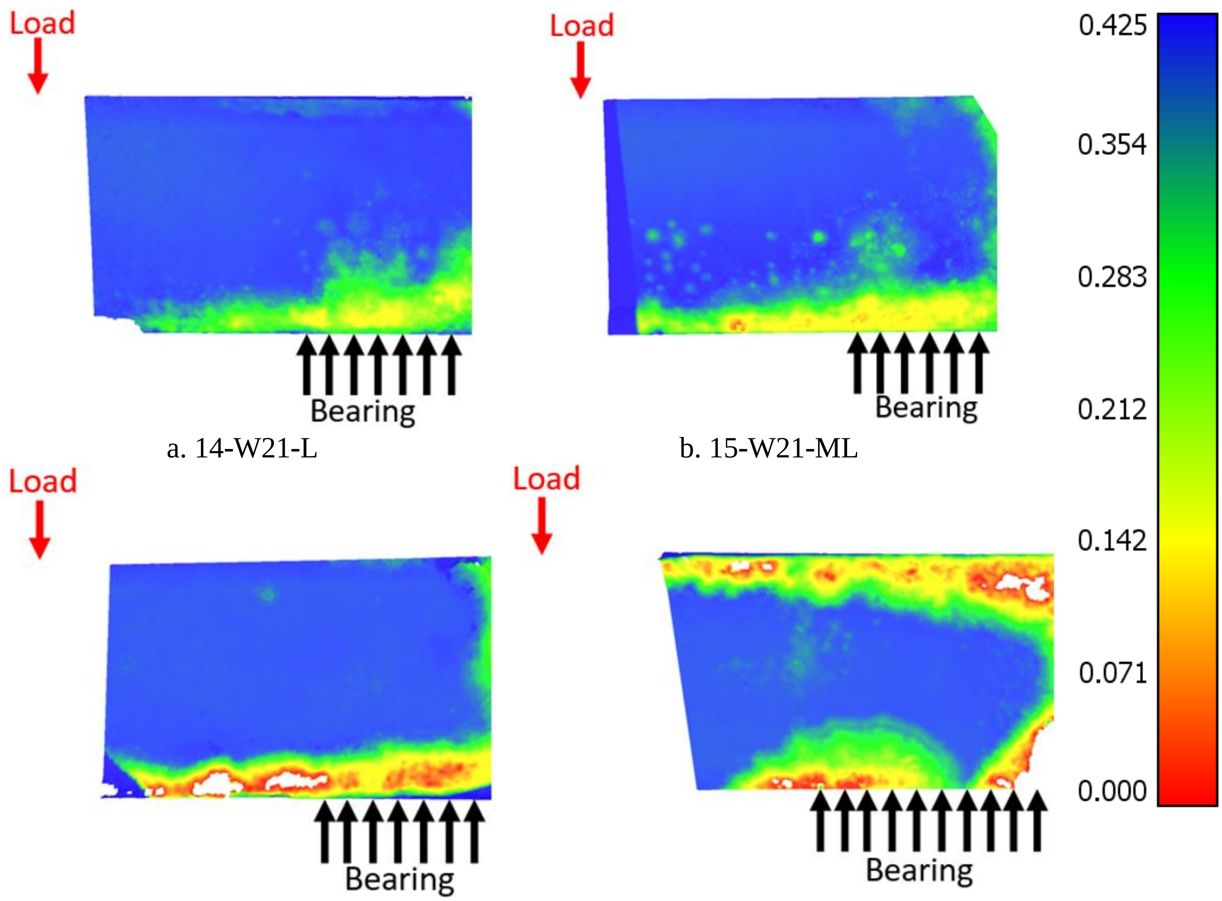

a. 14-W21-L b. 15-W21-ML
c. 16-W21-MH d. 17-W21-H

Figure 35. Photos of W21x62 Beam End Specimens (in)

The damage on 15-W21-ML shows a slightly more uniform lower web section loss than 14-W21-L. In Figure 35b, the 0.25-inch thickness losses in yellow continue across the scan's length at an average height of 2 inches from the bottom flange. Additionally, 0.1 to 0.15-inch section losses were scattered throughout the lower half of the web, shown as green blotches. The missing corner at the top right of the scan was due to the DIC camera's orientation during the profile scanning process.

The section losses present on specimen 16-W21-MH were heavily concentrated near the top and bottom of the web shown in Figure 35c. Note that the beam was inverted for this load test. This orientation was used because the web-end angle bracing could not support the highly deteriorated top flange. As a result, the concentrated web section losses in the 3-inch corrosion band were positioned at the top of the web. Additional localized section losses can be seen at the bottom of the web.

Specimen 17-W21-H was selected as the high damage beam due to multiple through-web holes located between the applied load and the support. The thickness loss band shown near the bottom of Figure 35d measured 3 inches in height. The damage ranged between 0.25 inches of thickness loss shown in yellow to near-total section loss in red. While it is possible that the more severe beam end damage shown in Figure 35c could result in lower capacity, the missing web area past the support was assumed non-influential to the shear behavior of the beam. However, the order of specimen damage from low to high does not necessarily correspond to the beams' performances during testing.

The W21x62 beam set again showed that the 3-inch average gave the most conservative estimate of the remaining web thickness (Table 12). Out of all the beam tests, the W21x62 specimens most resembled the corrosion patterns expected from bridges with compromised deck joint leaking. The results of using these averages to estimate beam capacity are further discussed in the Results and Discussion section of Task 3.

Table 12. W21x62 Specimens Web Thicknesses Based on Different Methods

Specimen	Minimum Cross-Section	45-Degree Average	Area Average	3-Inch Average	4-Inch Average
14-W21-L	0.387	0.389	0.401	0.245	0.259
15-W21-ML	0.364	0.363	0.376	0.174	0.214
16-W21-MH	0.344	0.348	0.354	0.131	0.186
17-W21-H	0.294	0.341	0.325	0.203	0.230

4.2 Load vs. Displacement Data

The data obtained from the full-scale tests included the load-displacement data and web deformation measurements from the DIC scans. Commentary for the gathered data accompanies each figure to clarify the significance of the results. The raw load data exhibited noticeable noise due to the use of the pressure transducer to track load. The pressure transducer was highly sensitive to pressure fluctuations in the hydraulic oil powering the hydraulic ram. The severity of these oscillations was partially handled using a 10:1 voltage divider, which significantly stabilized the signal received by the data logger by reducing the incoming voltage. While this may have reduced the signal's fidelity, this was necessary to read the load accurately during testing. Secondly, after a peak load had been reached, the pressure in the hydraulic cylinder would decrease over time before settling. This effect was due to cylinder drift, which is the equalization of oil pressure on either side of the piston in the hydraulic cylinder over time. The cylinder drift did not result in significant changes in vertical displacement due to this relaxation. Thus, both the remaining fluctuations and settling issues were adjusted in post-processing. This adjustment was made using a Savitzky-Golay filter to smooth the raw data curves shown in Figure 36.

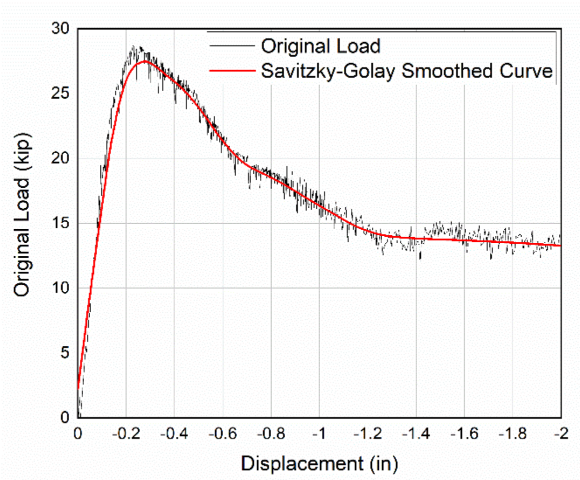

Figure 36. Specimen 3-S8-MH Raw Data (Black) vs. Savizky-Golay Filtering (Red)

One noticeable change made by the filter was a decrease in the overall maximum load between the original data and the smoothed curve. It was known that the initially reported load received from the pressure transducer was too high because the oil pressure was still equalizing. The true load was closer to what was reported after the hydraulic cylinder was given time to equilibrate its internal pressures, which is why the lower value of the plotted curve was used.

The following sections present the load-displacement curves for each set of beam tests according to their shape. Additionally, the maximum load reached by each beam is reported, as well as the exhibited failure mode, the AISC shear capacity, and the AASHTO estimated shear capacity. Comparisons to the other studies included in the report’s literature section are discussed further in the Results and Discussion Task 3 section.

The failure modes provided for each beam test correlate to the governing failure mechanism. These failure modes included web buckling, web yielding, web crippling, and web compression cracking. Web buckling occurs in beams with slender webs, where high stresses within the height of the member cause sudden lateral deformation of the beam perpendicular to the line between the applied load and the support. While the loads required to initiate this type of failure are typically much higher than the other types, it may occur due to web thinning in the beam's height between the applied load and the support. Web yielding and web crippling occur due to the high concentrations of forces located directly beneath the applied load and directly above the support. While both failure types may appear similar, AISC 360-16 defines web local crippling as "crumpling of the web into buckled waves directly beneath the load, occurring in more slender webs, whereas local web yielding is yielding of that same area, occurring in stockier webs" (AISC 2016). Typically, web yielding occurs in the web to flange fillet due to thinning of the web member along this interface, while web crippling occurs within the web height. The web height to thickness ratios for the nominal specimen shapes is provided in Table 13, along with the calculated web slenderness values from Table B4.1a case 5 from AISC 360-16. The height to thickness ratios of these beams were above the slenderness ratio for the W16x45 and W21x62 beams, meaning they are slender members, while the S8x18.4 and W10x26 beams were non-slender. The S8x18.4 members did not exhibit web crippling or yielding, so this distinction did not apply. Finally, web compression cracking occurs due to web holes which cause high concentrations of stresses during loading. Shear stresses generated during loading use these openings as initiation points for web cracking, often propagating towards other nearby web openings, the web to flange fillet, and the beam end. The loads required to initiate web cracking are often sudden and unpredictable and are not typically addressed in shear failure literature.

Table 13. Web Height to Thickness Ratios for the Four Tested Specimen Shapes

Specimen Shapes	Web Height	Web Thickness	h/t_w Ratio	Slenderness Ratios
S8x18.4	6.00	0.271	22.14	40.81
W10x26	8.25	0.260	31.73	39.55
W16x45	13.63	0.345	39.51	32.51
W21x62	18.38	0.400	45.95	33.92

Typical images of the four shear failure types are provided in the figure below. Figure 37a shows a web buckling failure occurring within the diagonal red oval perpendicular to the dashed red line between the applied load and the support on specimen 2-S8-ML. This occurred due to web section losses thinning the web at mid-height between the applied load and the support. During full-scale testing, no beams exhibited web yielding because the beam webs were not stocky, so Figure 37b shows an example of this failure type in another study where the yielding occurred along the top flange fillet due to lateral rotation of the top flange (Narmashiri et al. 2011). Figure 37c shows an example of a web crippling failure that occurred at 3 inches above the bottom flange at the bearing for specimen 9-W16-L because the W16x45 shape is considered slender. In the discussion of web failure modes experienced during load testing, some failures more closely resemble developed continuous plastic web bending along the length of the web from the end than true web crippling failures developed above the bearing due to high concentrations of compressive force. While it is worth noting that these failures do not meet the traditional definition of web crippling, they are referred to as web crippling failures due to their similarity in location for the simplicity of categorization. Finally, Figure 37d shows an example of web cracking occurring on specimen 4-S8-H, where cracks formed between adjacent web holes along the height of the beam. This crack formed due to the formation of diagonal shear stress bands perpendicular to the loads creating tension forces shown as red arrows, which pulled the web apart in the red oval.

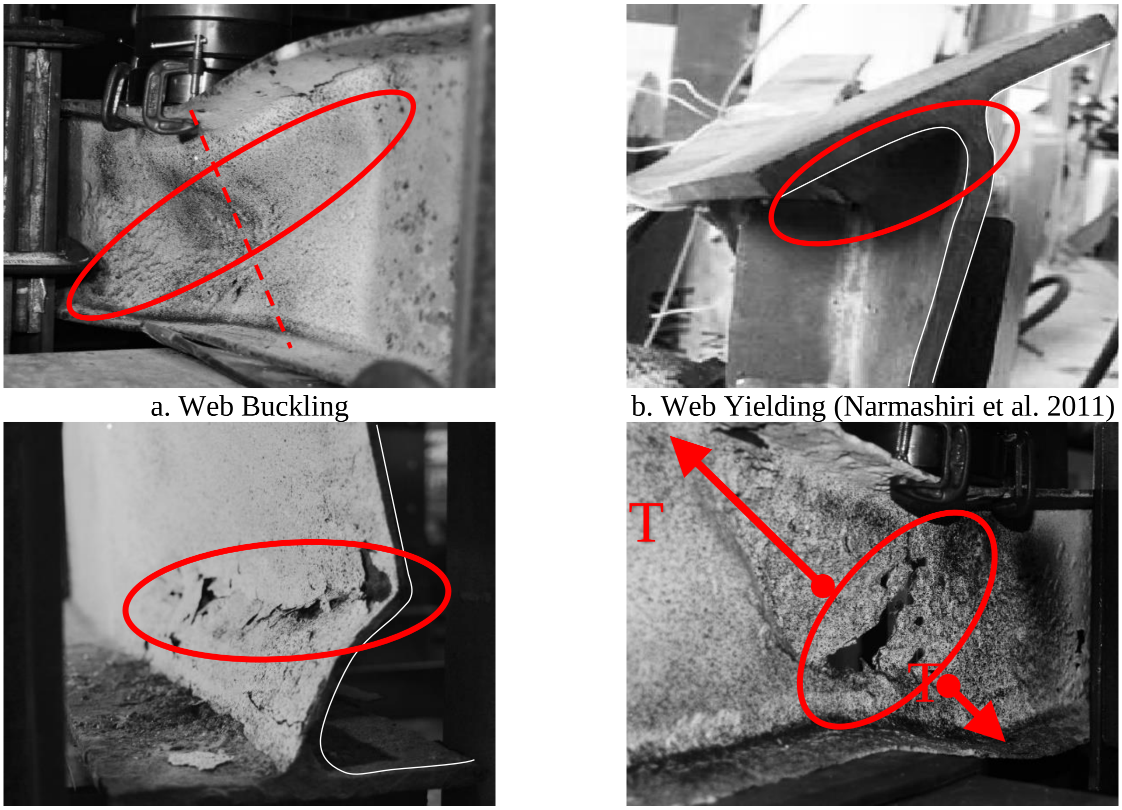

a. Web Buckling
b. Web Yielding (Narmashiri et al. 2011)
c. Web Crippling
d. Web Cracking

Figure 37. Photos of Shear Failure Types

4.2.1 S8x18.4 Beams – Tests 1-4

The load curves for the first set of S8x18.4 beams behaved as expected; however, it should be noted that the data gathered for specimen 1-S8-L is more linear than the others (Figure 38). The first test was performed with the string potentiometer placed away from the applied load due to restrictions on available space. It was decided that it would be inappropriate to compare the data gathered in this alternate position to the other S8x18.4 test data. The data for 1-S8-L was instead retrieved from the displacements measured in the ARAMIS DIC software. For this specific case, displacement measurements were averaged from five sampled points placed along the bottom flange fillet. These locations were selected to reduce the influence of vertical displacement due to web deformation.

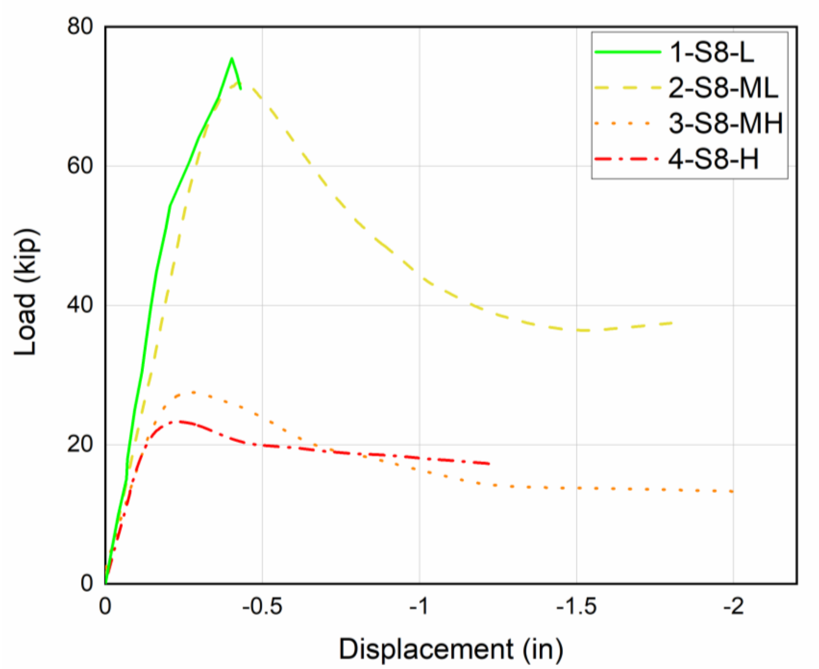

Figure 38. S8x18.4 Load vs. Displacement Data

The load vs. displacement data for the S8x18.4 beams all showed similar linear elastic behavior before yield. This similarity was surprising for specimens 3-S8-MH and 4-S8-H, as they exhibited very irregular beam profiles due to severe corrosion across the full height and length of their webs. Table 14 summarizes all the S8x18.4 beams' test performance in terms of maximum load, failure mode, and the calculated AASHTO and AISC beam shear capacities using the minimum average web thickness taken between the beam end and the applied load. Note that the maximum loads do not necessarily represent the point at which failure was initiated. The maximum load values were presented to provide a consistent reference; however, the maximum displacement varied between tests. The strain behaviors of the beams are further discussed in the True Major Strain Fields subsection. However, the point at which specimens 1-S8-L and 2-S8-ML began to show concentrated bands of plastic strain behavior ranged from 50 to 55 kips, which is much closer to the calculated capacities according to AASHTO and AISC. Additionally, specimens 3-S8-MH and 4-S8-H both began showing localized buckling failure between 15 and 20 kips.

Table 14. S8x18.4 Load Table

Specimen	Maximum Load (kips)	Failure Mode	AASHTO Capacity (kips)	AISC Capacity (kips)
1-S8-L	75.50	Web Buckle	46.94	48.56
2-S8-ML	72.02	Web Buckle	39.18	40.54
3-S8-MH	27.48	Web Cracking	21.70	22.44
4-S8-H	23.31	Web Cracking	21.67	22.42

4.2.2 W10x26 Beams – Tests 5-8

The data gathered in the second set of beam tests is displayed in Figure 39. Like specimen 1-S8-L, the displacement data for 5-W10-L was also collected from the GOM DIC software for the load tests using the vertical displacement value of points near the bottom flange. This procedure was necessary because the data exported from the data logger became corrupted upon export.

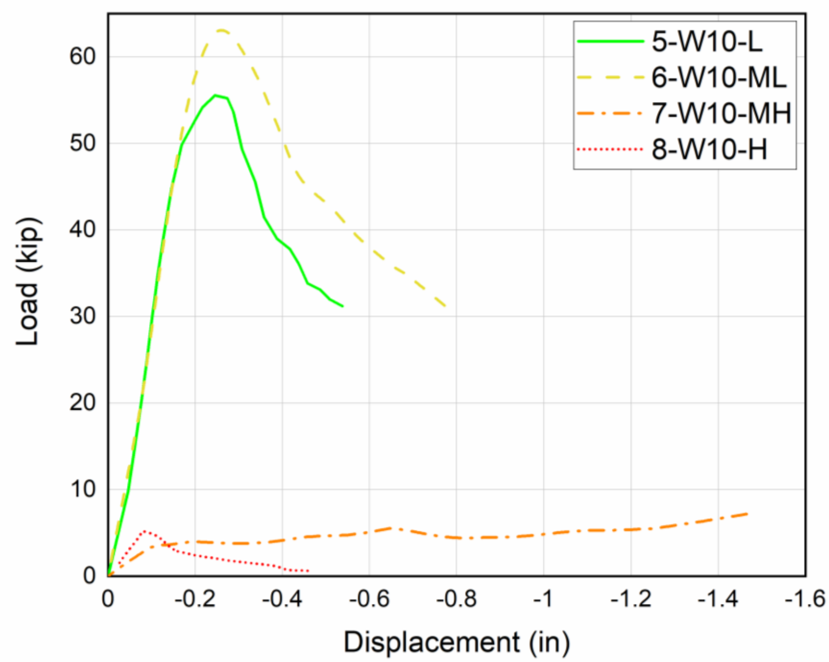

Figure 39. W10x26 Load vs. Displacement Data

The separation between the low and medium-low damage specimens and the two higher damage beams is much greater than the first beam set as shown in both the load vs. displacement data and Table 15. Although the medium-high and high damage W10x26 specimens had holes like the S8x18.4 beams, the main distinguishing factor was the presence of advanced lower web section losses rather than total web height damage. After a crack propagated across the full length of the engaged bearing area, the webs failed. Discussion of the strain fields later in the paper will discuss this behavior regarding specimens 7-W10-MH and 8-W10-H.

Table 15. W10x26 Load Table

Specimen	Maximum Load (kips)	Failure Mode	AASHTO Capacity (kips)	AISC Capacity (kips)
5-W10-L	55.57	Web Crippling	61.12	63.24
6-W10-ML	63.08	Web Crippling	59.07	61.11
7-W10-MH	7.19	Web Crippling	45.62	47.19
8-W10-H	5.18	Web Crippling	46.21	47.80

4.3.3 W16x45 Beams – Tests 9-13

All W16x45 beams' test data share a similar load vs. displacement relation before reaching maximum load and eventual beam failure. As expected, specimen 13-W16-L(A) showed much more capacity than any other since it did not have any web end corrosion due to being cut from the middle of a beam. One discrepancy shown in Figure 40 is that the high damage specimen 12-W16-H exhibited a higher capacity than even the original low damage beam 9-W16-L. This occurrence prompted testing for 13-W16-L(A) after realizing that all previous specimens had beam-end web thinning.

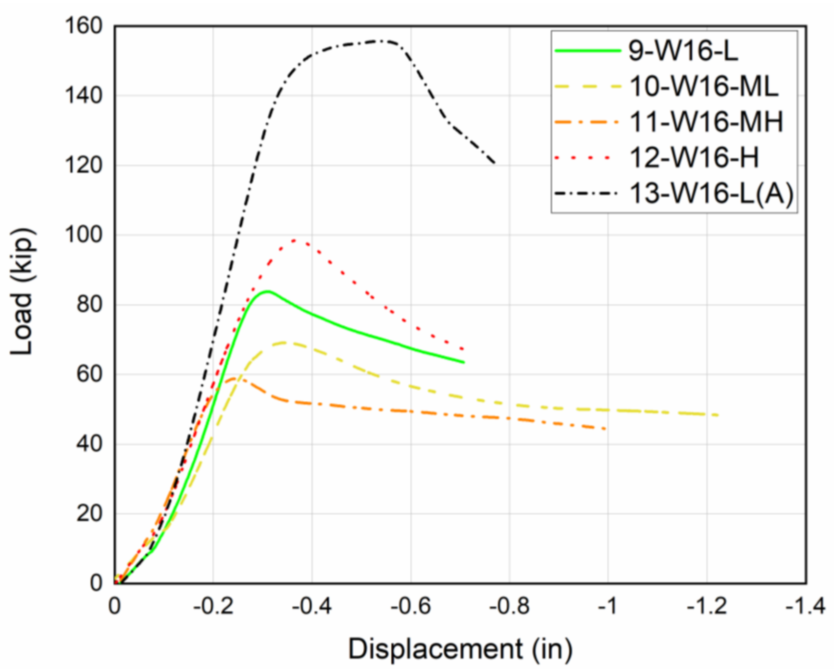

Figure 40. W16x45 Load vs. Displacement Data

The behavior of 12-W16-H is because all the W16x45 beams failed at the bearing (see Table 16), so damage located directly above the support governed the beams' capacity. Specimens 9-W16-L, 10-W16-ML, and 11-W16-MH all showed typical beam end web corrosion with concentrated damage above the support, while 12-W16-H instead displayed severe localized section losses continuing along the length of the beam. The absence of full-height web end damage in 12-W16-H was because, like 13-W16-L(A), it was cut from the mid-section of a beam. Due to the absence of any full-height web corrosion, 12-W16-H showed better performance than the other tests since it did not have adequate damage outside of the bearing area to initiate a local failure away from the support.

Table 16. W16x45 Load Table

Specimen	Maximum Load (kips)	Failure Mode	AASHTO Capacity (kips)	AISC Capacity (kips)
9-W16-L	83.81	Web Crippling	57.20	60.06
10-W16-ML	69.16	Web Crippling	116.35	120.36
11-W16-MH	58.83	Web Crippling	39.22	46.64
12-W16-H	98.54	Web Crippling	129.74	134.22
13-W16-L(A)	155.72	Web Buckling	133.02	137.61

4.3.4 W21x62 Beams – Tests 14-17

The load vs. displacement curves for the W21x62 beams once again followed a similar pre-failure linear relationship between load and displacement seen in Figure 41. One central discussion point is that the medium-high damage specimen 16-W21-MH showed a higher maximum load than the medium-low damage 15-W21-ML. This discrepancy was due to the beam's failure mode, where holes in the lower web caused a quick crack formation before reaching 10 kips of applied load. Thus, most of the curve is post-failure behavior after the upper web began to rest on the bottom flange. As a result, the maximum load recorded by the DIC before failure for 16-W21-MH was 11.12 kips as shown in Table 17 below. Additionally, 16-W21-MH experienced a significant amount of out-of-plane deflection, causing it to lean against the intermediate bracing. Consequently, the applied load continued to rise past the point of failure due to the bracing resistance until the beam eventually began to slip, resulting in the load drop represented by the vertical portion of the 16-W21-MH curve. This was the only exception to the inclusion of the absolute maximum load for the experimental values because it was the only test that was noticeably affected by a failure in the test configuration.

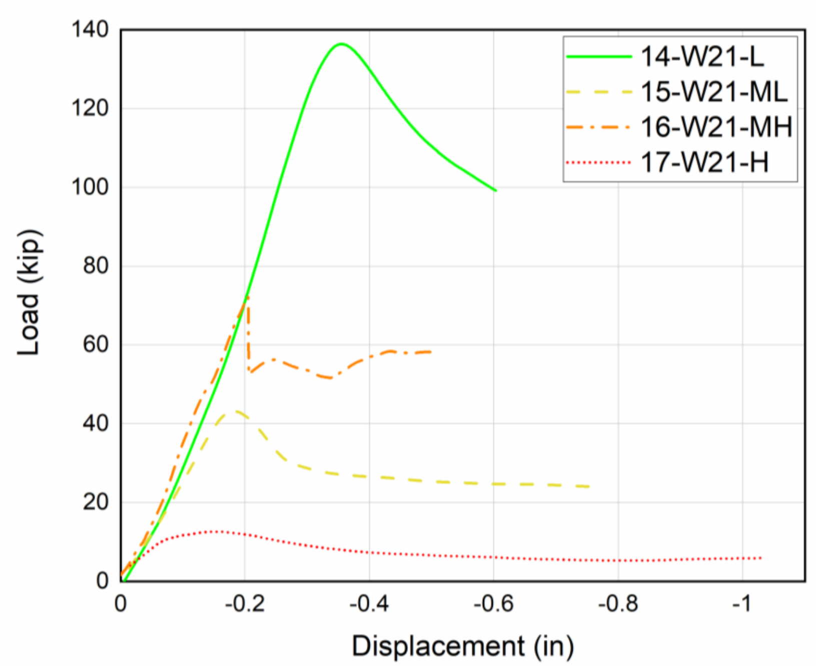

Figure 41. W21x62 Load vs. Displacement Data

Table 17. W21x62 Load Table

Specimen	Maximum Load (kips)	Failure Mode	AASHTO Capacity (kips)	AISC Capacity (kips)
14-W21-L	136.39	Web Crippling	182.89	189.19
15-W21-ML	43.14	Web Crippling	177.29	183.41
16-W21-MH	11.12*	Web Crippling	181.70	187.96
17-W21-H	12.63	Web Crippling	54.05	70.51

*Before crack formed

4.3. True Major Strain Fields

The following true major strain fields were created in the GOM Correlate software using DIC pictures captured during the large-scale shear load testing. Each image presented shows the true major strains at a point during the loading process. Each particular point in time was chosen explicitly to illustrate the strain behavior when the initial web failure mode became identifiable. These modes include crack initiation and propagation, web buckling, and local web crippling below the load or above the support. Not all specimen strain fields were included due to similar behavior to other specimen tests or difficulty in identifying useful information for the report. Additional strain fields for all of the specimens excluded in the True Major Strain Fields subsection may be referenced and provided in Appendix A: Additional Strain Field Figures at the end of the document.

4.3.1 S8x18.4 Strains

The strain field quality for 1-S8-L was excellent for being the preliminary experiment due to the uniform web surface, which was easily tracked by the DIC cameras. The initial test of specimen 1-S8-L clearly shows the development of stress bands, illustrated as red and yellow patterns in Figure 42. As the load increased to its maximum at 75.5 kips, these strains formed a diagonal web buckle perpendicular to the load path between the applied load and support's interior face. Simultaneously, the beam also displayed a typical shear failure mode where the top and bottom flanges buckled and the entire beam past the support began to displace downwards.

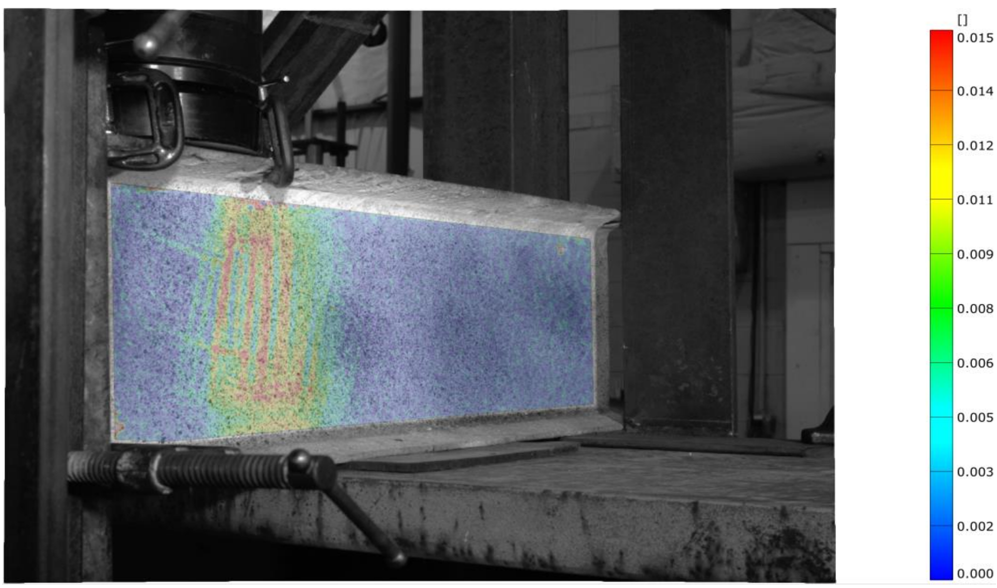

Figure 42. 1-S8-L True Major Strain Field at 55 Kips of Loading Before Maximum Loading

Specimen 2-S8-ML displayed a similar diagonal web buckling failure to 1-S8-L, as shown in a more advanced state of deformation in Figure 43. A post-buckling image was chosen as the shear field's signs of initiation were less apparent due to the highly irregular web surface. Like 1-S8-L, the second beam displayed a combined web buckling and full height beam shearing behavior. This initial failure is represented on the load-displacement diagram (Figure 38, 2-S8-ML) as the transition past the maximum loading. Additionally, the DIC software identified a high area of strain at the site of a localized web deformation at the top right corner of the strain field, which formed after the diagonal web buckle progressed.

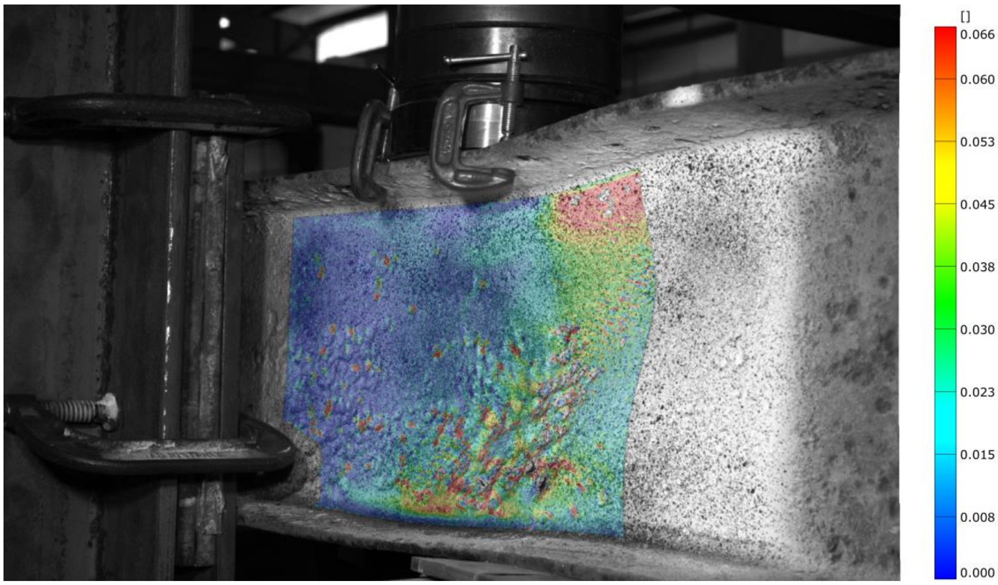

Figure 43. 2-S8-ML True Major Strain Field at -0.7 Inches of Vertical Displacement After Failure

Specimen 3-S8-MH had a much more irregular surface profile than the first two beams, which resulted in a highly complex strain field shown in Figure 44. However, this image also displays crack propagation between the three vertical holes above the edge of the support represented by the high strains connecting the openings (shown in a red circle in the figure). This crack eventually resulted in a full-height web separation along this high strain line combined with a diagonal buckling in a line connecting the longitudinal band of holes approximately 2-inches from the bottom flange.

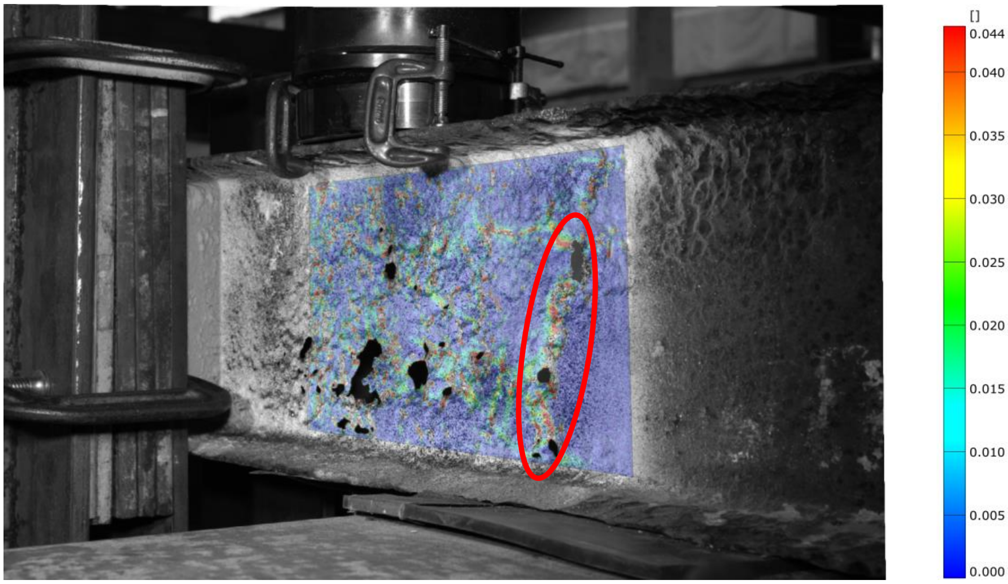

Figure 44. 3-S8-MH True Major Strain Field at 20 Kips of Loading Before Failure

The final S8x18.4 high damage beam showed a similar strain development between the through web holes (Figure 45). The web separated between the holes in two cracks, vertically along the holes directly below the applied load, and horizontally between the strip of holes 1.5 inches above the bottom flange.

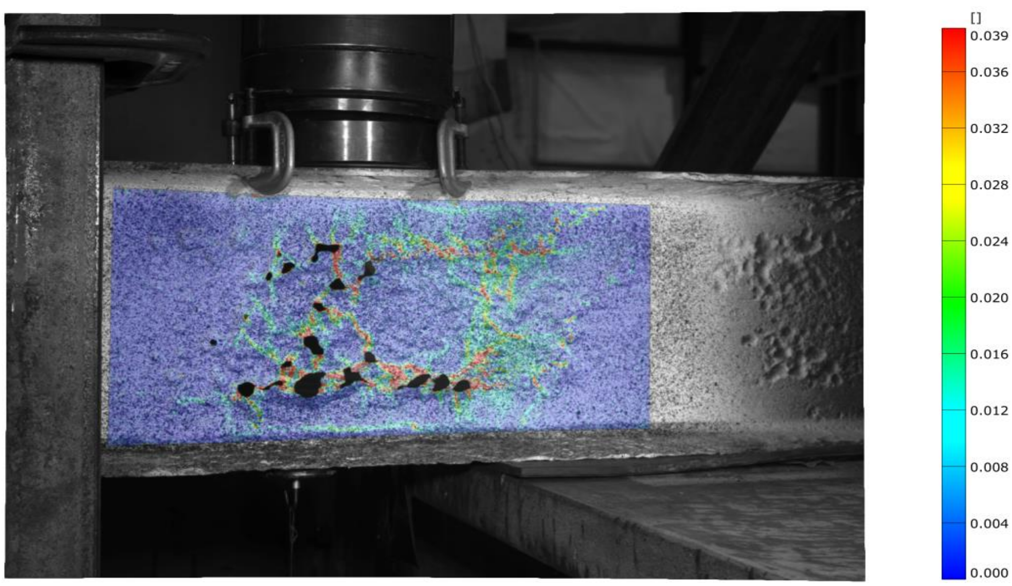

Figure 45. 4-S8-H True Major Strain Field at 22.8 Kips of Loading Before Maximum Loading

4.3.2 W10x26 Strains

Specimen 5-W10-L displayed a comparable strain field to specimen 1-S8-L, where diagonal stress bands formed in the area between the applied load and the face of the support (Figure 46). However, a horizontal stress concentration below the load was observed. This stress concentration developed further and caused a local buckling failure where the web under the top flange folded downwards at the maximum load before a diagonal web buckle could form. This behavior was peculiar, as the surface profile indicated no section losses near the top flange. Instead, the web only displayed minor 1/16-inch section losses for 2.5 inches above the bottom flange on the west face (not shown). It was determined that this action was because the failure first initiated as a local displacement at the section loss above the lower flange on the west side of the web (into the image). Subsequently, a corresponding local failure initiated at the top of the east web displacing to the east (out of the image).

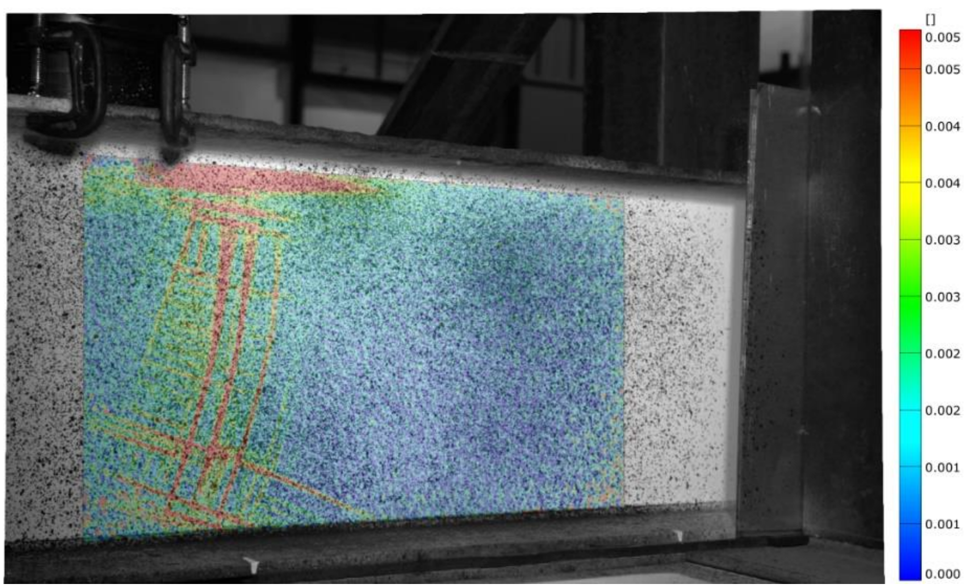

Figure 46. 5-W10-L True Major Strain Field at 49.8 Kips of Loading Before Failure

A similar occurrence to 5-W10-L appears in specimen 6-W10-ML. A horizontal high strain band appeared below the applied load near the top flange in Figure 47, precipitating a local buckling failure of the web in this region. This failure was produced by 0.1-inch section losses in the lower portion of the west face of the beam, which again caused a pair of local out-of-plane displacements in the web.

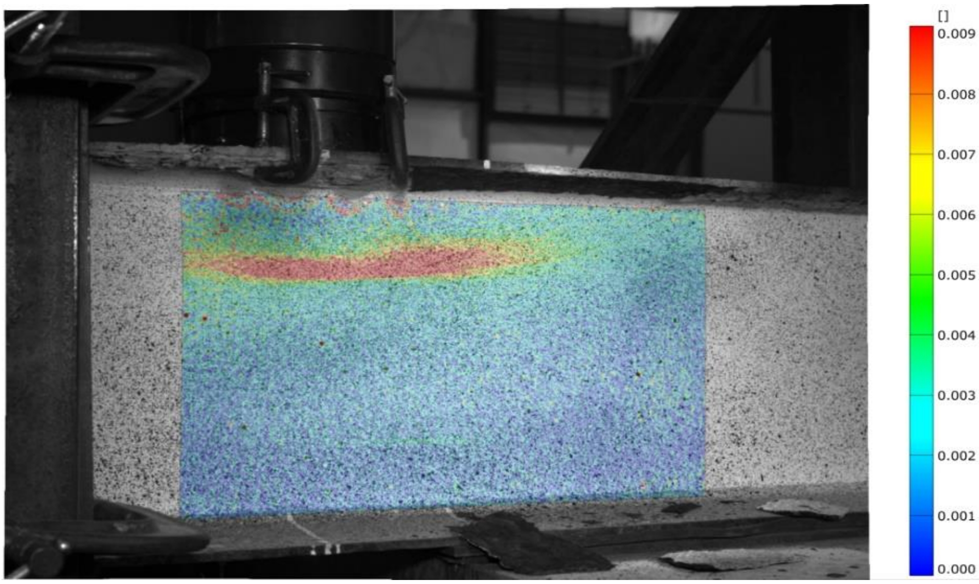

Figure 47. 6-W10-ML True Major Strain Field at 49.9 Kips of Loading Before Failure

For specimen 7-W10-MH, the failure was initiated between six holes at the bottom of the web near the support (Figure 48), which continued until the beam's end. Like specimens 3-S8-MH and 4-S8-H, multiple web openings created a line of high strain between them. This behavior was exacerbated because the beam end was much closer to the support, which reduced the available material to confine the crack. Additionally, the reduced support length from using the welded plate resulted in higher stress concentrations above the short bearing area which ultimately caused a web crippling failure, folding the lower web before the steel could separate.

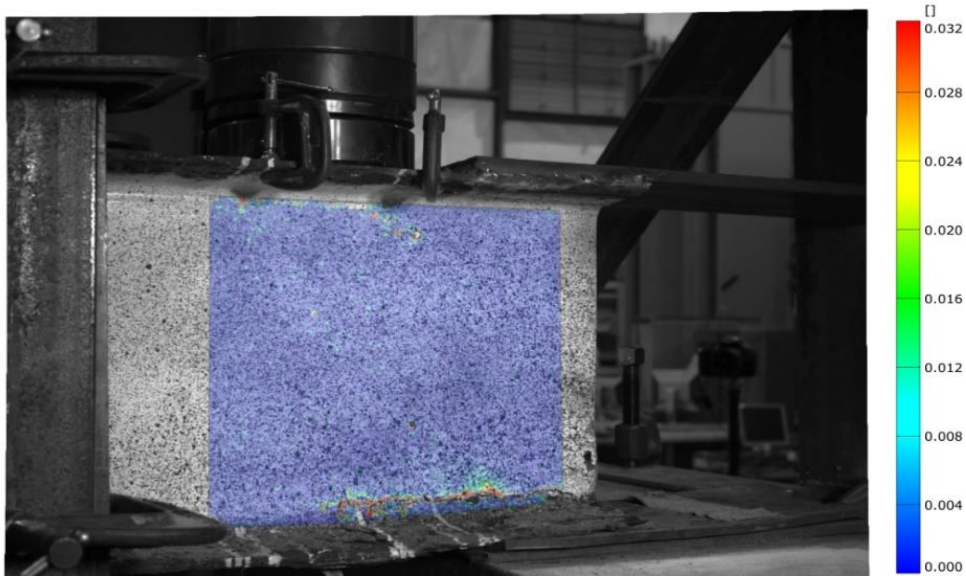

Figure 48. 7-W10-MH True Major Strain Field at -0.45 Inches of Vertical Displacement After Failure

The behavior of specimen 8-W10-H was similar to 7-W10-MH, as the hole in the area between the load and support initiated failure. The beginning of the failure is shown in Figure 49 as a thin red line extending from a pinhole in the web, which is marked with a red oval. Instead of traveling towards the beam end, this high strain line propagated to the 1-inch hole directly beneath the load and quickly jumped to the large 3.4-inch opening to the left. These stress concentrations quickly resulted in local web folding on either side of the 1-inch hole beneath the load. This behavior was categorized as a web crippling failure like 7-W10-MH, where web folding due to concentrated loads above the bearing was augmented by the path of stress concentrations caused by the web holes.

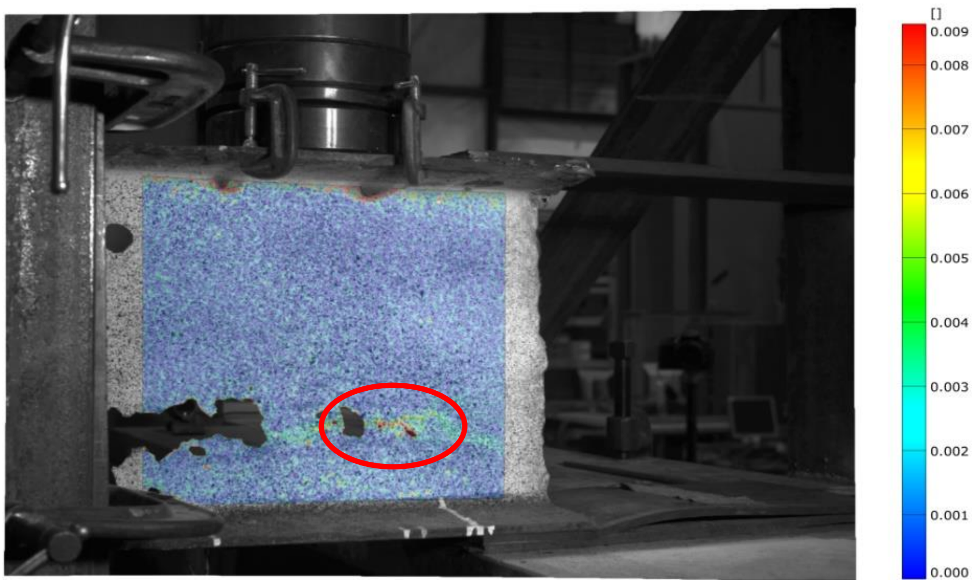

Figure 49. 8-W10-H True Major Strain Field at 5 Kips of Loading Before Maximum Loading

4.3.3 W16x45 Strains

The failure of specimen 9-W16-L occurred as a local web buckle extending to the beam end, similar to how the crack developed in 7-W10-MH. In this case, there was no separation of the beam, but the material strain increased along the line seen in red in Figure 50 until failure occurred. It was assumed that the bearing strength would control in this configuration due to the extensive damage present above the support. Although no damage continued past the face of the bearing pad (marked as a faint white line in the bottom right of Figure 50), the corrosion still caused a change in failure mode from the regular diagonal web buckling, as shown in specimen 13-W16-L(A).

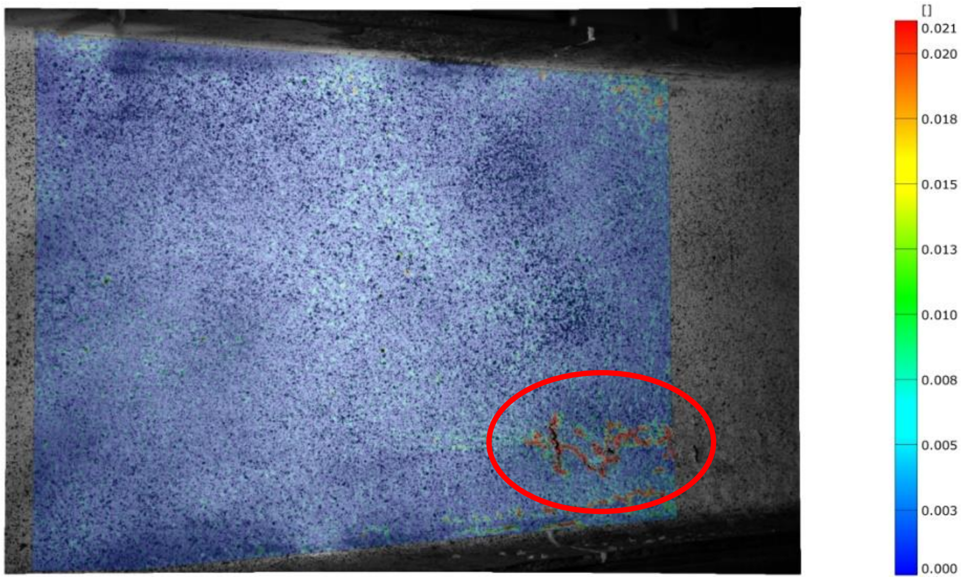

Figure 50. 9-W16-L True Major Strain Field at 77 Kips of Loading Before Failure

The strain field shown in Figure 51 clearly shows the development of a line of high-stress concentration in the lower web above the support. These strains eventually developed into a local crippling failure in this line leading the entire beam past the face of the support deflecting vertically downwards.

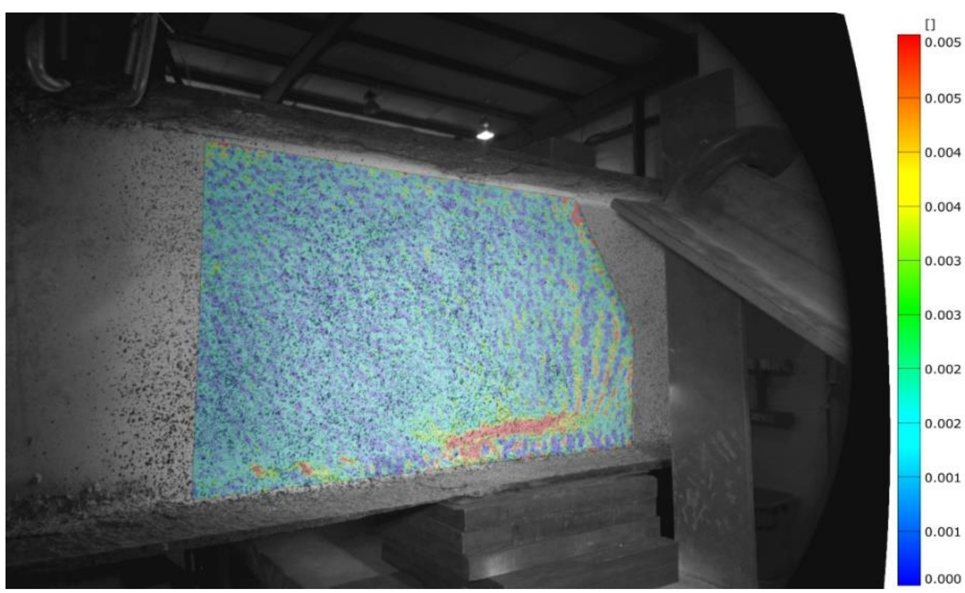

Figure 51. 10-W16-ML True Major Strain Field at 67 Kips of Loading Before Failure

Specimen 11-W16-MH developed a nearly identical failure mode to 9-W16-L. A local buckling beginning above the face of the support extending to the beam end occurred (Figure 52). This failure was due to the extensive section losses near the bottom flange, primarily above the support. Despite the applied load being placed so far from the support, failure resembled a bearing failure rather than some form of local buckling at the support's face.

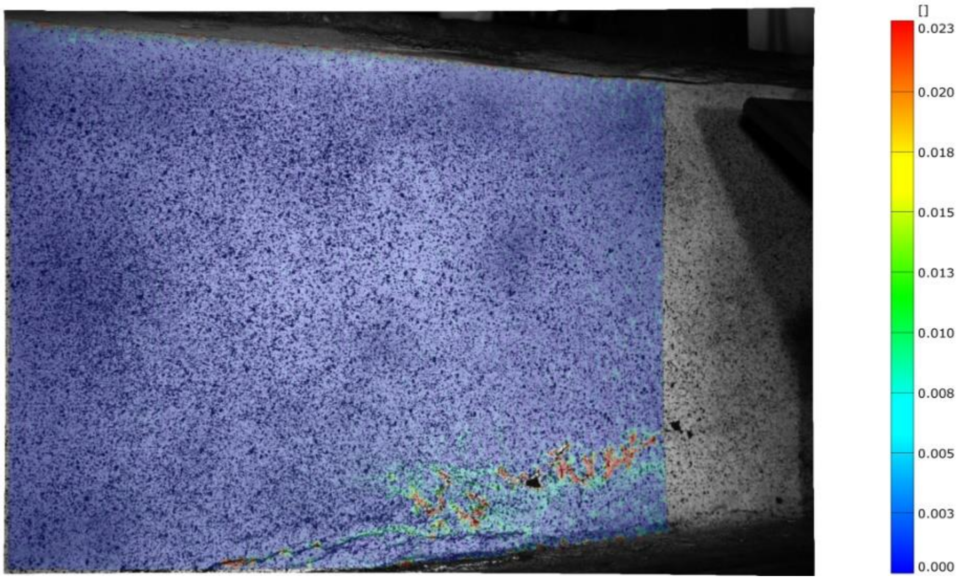

Figure 52. 11-W16-MH True Major Strain Field at 55 Kips of Loading Before Failure

Specimen 12-W16-H exhibited two main areas of strain concentrations below the applied load and above the support (Figure 53). Like specimen 9-W16-L, local web crippling above the support was the governing failure mode. This observation is of interest as most other beam tests favored either failure at the support or below the applied load, but this was the only specimen that simultaneously displayed signs of both cases.

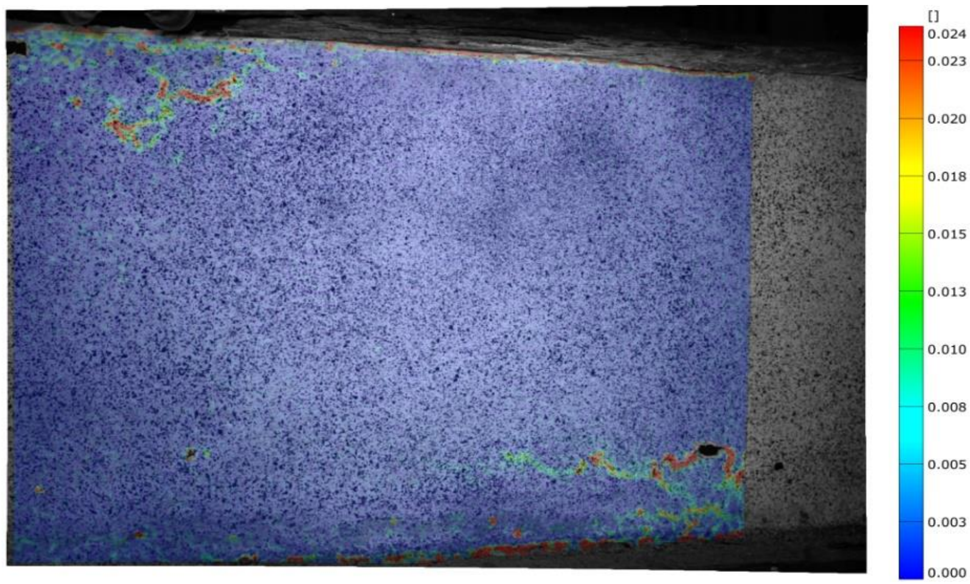

Figure 53. 12-W16-H True Major Strain Field at 79 Kips of Loading Before Failure

The failure mode in 13-W16-L(A) is what was expected to occur in 9-W16-L, which validates its addition to the testing matrix. Multiple vertical and horizontal stress bands can be seen forming on the web's surface as well as a large area of high stress below the applied load. This stress pattern led to a combined local deflection below the loading point and diagonal web buckle from the lower left to the top right of Figure 54.

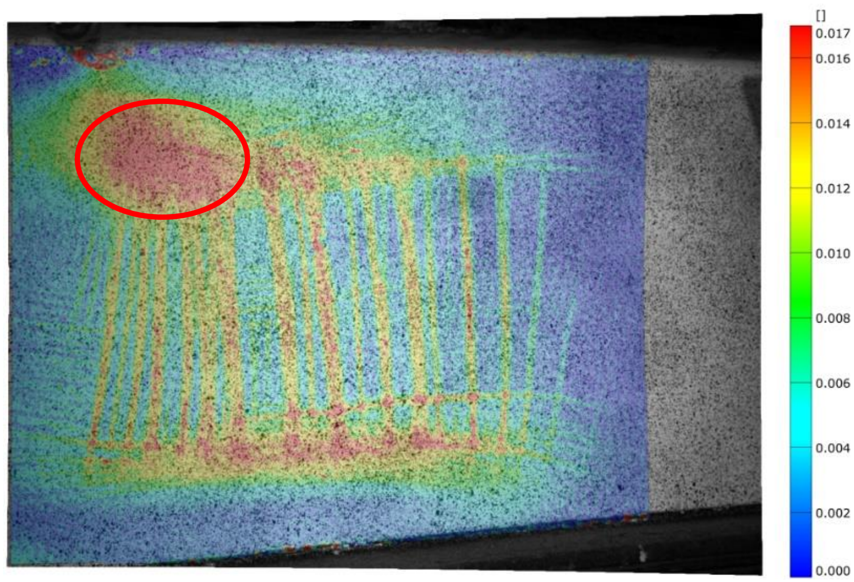

Figure 54. 13-W16-L(A) True Major Strain Field at 145 Kips of Loading Before Failure

4.3.4 W21x62 Strains

The failure pattern of specimen 14-W21-L occurred as a local buckling beneath the top flange at the loading point. Figure 55 shows the stress field condition directly before reaching the maximum load. This failure mode was like that of specimen 6-W10-ML, which would suggest that it was due to section loss either near the top flange or as a mirrored local buckling due to section loss near the bottom flange below the load.

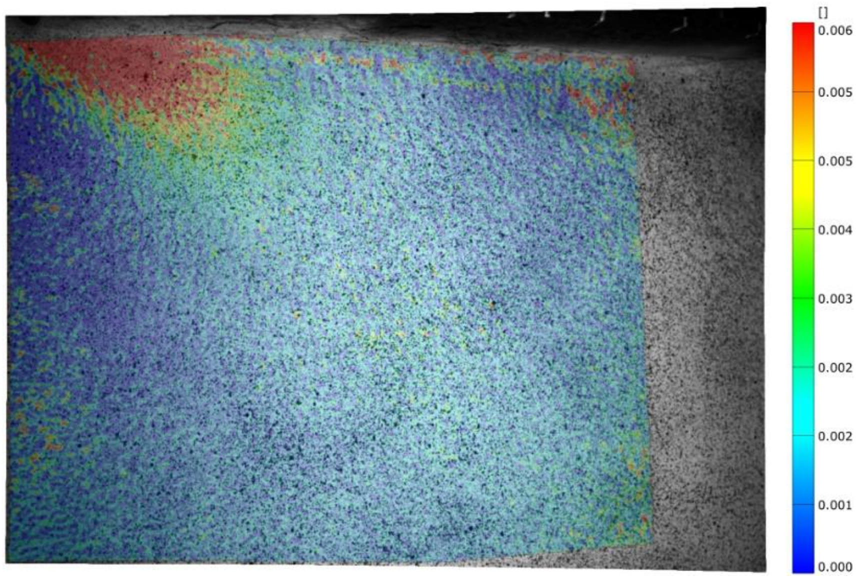

Figure 55. 14-W21-L True Major Strain Field at 133 Kips of Loading Before Failure

The failure of specimen 15-W21-ML was like that of 9-W16-L because most of the deformation preceding failure occurred outside of the DIC scanned area above the support (Figure 56). The strains in 15-W21-ML were all below 0.003, which makes them well below any other values shown so far. Despite spacing the applied load so far from the bearing area, the damaged web section above the support controlled the beam’s failure mode. Like 9-W16-L, it would also be assumed that the bearing strength would govern for this beam, but it is worth noting that the 21 inches of web between the applied load and the support were not engaged whatsoever during the entire failure of 15-W21-ML.

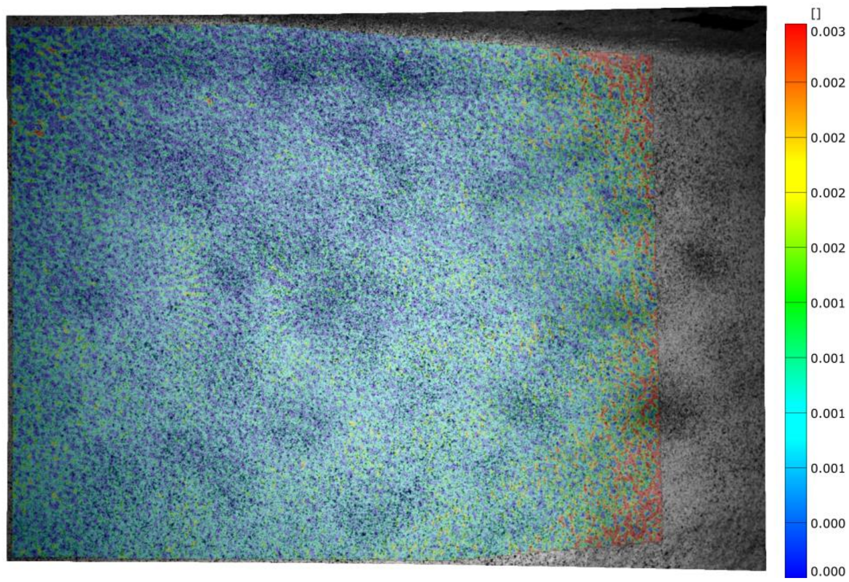

Figure 56. 15-W21-ML True Major Strain Field at 45 kips Loading Before Failure

Failure of 16-W21-MH was due to the presence of a line of through-web holes above the bottom flange (Figure 57). Like specimen 8-W10-H, the failure mode was a line of buckling between the lower web holes, which extended to the beam end. The strain condition captured by the DIC camera showed minimal variation like 15-W21-ML, and the buckled regions between the holes deflected below the view of the camera.

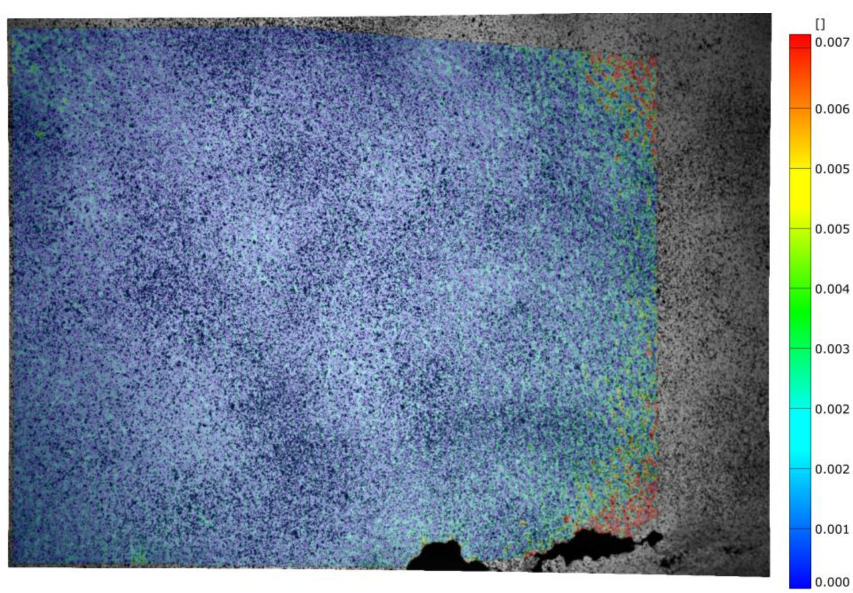

Figure 57. 16-W21-MH True Major Strain Field at -0.15 inches Vertical Displacement After Failure

The failure in specimen 17-W21-H also occurred outside of the camera's view in the section loss below the top flange (Figure 58). The web developed a local out-of-plane buckle below the applied load, which has been typical for several beam failures preceding this one, including tests 5, 6, 13, and 14. It appears that defects in the area directly below the applied load significantly contributed to the beam's failure behavior.

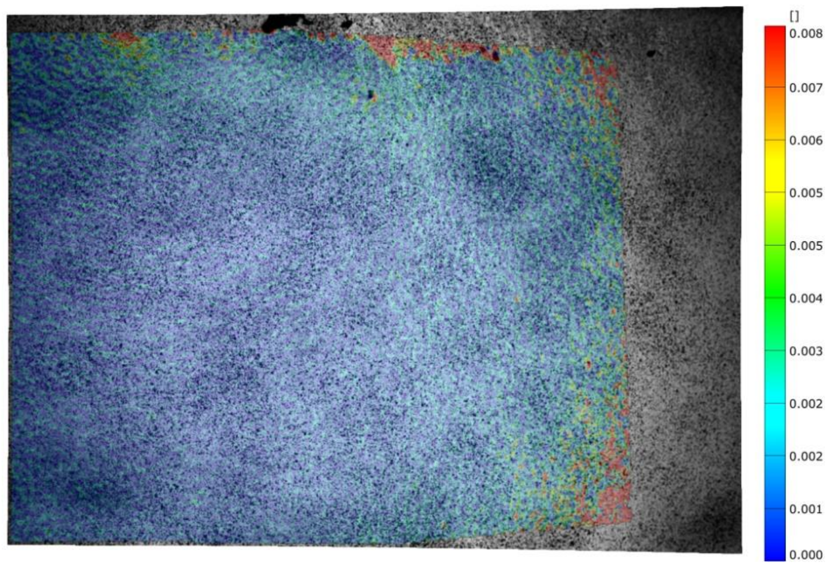

Figure 58. 17-W21-H True Major Strain Field at 52 kips Loading Before Failure

Finally, several observations can be summarized from the failure behavior of the 17 beams tested in this study.

1) Like the conclusions from the Kayser and Nowak studies, beams with less section loss remained close in maximum capacity to one another, while beams with significant section losses or holes showed drastically less capacity. This suggests that the initial linear and later non-linear relationship between section loss and shear capacity holds true.
2) AASHTO and AISC results using the minimum average effective web area are not accurate predictors of remaining web capacity, especially in the case of beams with web holes.
3) Damage on the web near the top flange significantly contributes to the beam's failure behavior by creating a site for local buckling to initiate.

4) Even when applied loads are not placed directly above the support, web section losses concentrated primarily above the bearing will result in web crippling failure to occur.
5) High strains will concentrate between through-web holes, which may initiate web buckling or separation in high section loss cases.

4.4 Comparison of Test Data to Literature

Several shear capacity calculations were compared to the full-scale test results to determine which methods would be appropriate for VDOT to use in bridge load rating. The purpose was to identify an approach that was more accurate than the minimum average cross-section approach, simple to implement into existing load rating procedures, and most importantly, assure the traveling public's safety while using structures evaluated using this approach.

The capacity calculation methods presented in the Literature Review section of the Results and Discussion were compared to determine their correlation to the outcome of the full-scale testing. Each calculation was completed using the measurement data collected from the figures presented in the DIC scanned beam profiles section of Task 2. The process for creating the thickness matrices used in this process is described in the test setup and instrumentation in the Methods section of Task 2. Although this computer measurement process is highly comprehensive, the implementation of these capacity calculation methods requires a method for gathering thickness data in the field without using DIC technology. Such methods could include an ultrasonic thickness gauge or a set of calipers.

AASHTO and AISC equations were both used as baseline shear calculation methods that used the five effective web areas. In addition to these two shear capacity calculation methods, five additional capacity calculation methods were selected to determine their correlation to the test results using the same thickness measurements mentioned above. The Sugimoto, Van de Lindt, and Rahgozar methods calculate a strength reduction ratio or percentage expressing a beam's remaining strength compared to a new beam. These methods rely on the accurate calculation of the undamaged shear capacity using AASHTO, AISC, or an equivalent. Both the Darwin and Tzortzinis methods calculate the capacity directly, and both require web opening measurements. Beams with web holes were measured to determine the length and height of any holes present. Although the holes were irregularly shaped, the length and height measurements assumed the smallest rectangular section fully encompassing the opening.

Table 18 presents the shear at the close support versus the capacities calculated using the seven estimation methods. Shear was calculated using the formulas presented in Table 3-23 of the AISC steel construction manual with an assumed 14-foot span length. The calculated ratios for Sugimoto, Van de Lindt, and Rahgozar were applied to the AASHTO undamaged beam capacities. Additionally, all equations excluding the Darwin and Tzortzinis calculation included an undefined average reduced beam thickness. The minimum average web thickness taken from the DIC scans has been used in these cases due to being a commonly used thickness measurement method before this study. While the Darwin method does not consider section loss outside of web openings, the Tzortzinis study used the lower damage effective web area, specifically for the lower 4 inches of the web. Thus, the lower damage average was used for the Tzortzinis calculations. Blank cells in the table signify that the calculation method could not be used for the associated beam. The Van de Lindt method applies to beams with more than 35% of the web height affected by corrosion, which did not allow it to be used on many higher damaged beams. The Darwin method was only applicable to calculate the effect of web openings, which ruled out beams only displaying section losses without holes.

Table 18. Test vs. Calculated Shear Capacities (kips)

Test	Shear at Close Support	AASHTO	AISC	Sugimoto	Van de Lindt	Rahgozar	Darwin	Tzortzinis
1-S8-L	71.01	36.33	37.58	36.51	36.50	36.57		43.80
2-S8-ML	67.73	35.24	36.45	32.41		35.24		30.21
3-S8-MH	25.84	16.79	17.37	16.10		26.01	46.73	18.00
4-S8-H	21.92	26.33	27.24	21.82		29.68	57.22	17.27
5-W10-L	52.26	51.33	53.10	51.29	52.75	51.33		42.18
6-W10-ML	59.33	49.38	51.08	50.50	46.16	49.38		37.33
7-W10-MH	6.76	22.75	23.88	34.22	38.24	23.93		15.22
8-W10-H	4.87	43.21	44.70	40.37		43.21	41.52	7.17
9-W16-L	72.83	58.62	67.80	128.92		91.88		53.53
10-W16-ML	60.10	60.84	69.50	145.86	157.11	90.14		52.71
11-W16-MH	51.13	39.64	52.24	155.05	154.57	78.15		57.79
12-W16-H	85.64	148.01	153.11	164.73	149.47	148.01		67.56
13-W16-L(A)	135.33	165.73	171.45	165.67	169.85	165.73		74.99
14-W21-L	114.47	107.55	118.93	237.72	222.29	149.31		89.40
15-W21-ML	36.21	38.97	60.45	221.40	197.86	106.45		54.95
16-W21-MH	9.33	16.51	34.10	212.71	144.12	79.95	259.76	4.35
17-W21-H	10.60	55.34	76.37	208.34	170.99	124.00		29.63

This data is displayed below as prediction error graphs, where the estimated capacity of each method appears as points on a scatter plot. These points can then be compared against a 45-degree line representing a one-to-one correlation to each beam's experimental shear capacity. Accurate analysis methods are indicated when the data points fall close to the 45-degree line. Points lying below the line indicate that the approach has overestimated the capacity (unconservative), while points lying above the line conversely mean the method has conservatively underestimated the test load.

Figure 59 shows the prediction error plots for all tested shear capacity calculation methods. The effective web area used to compare each method was the minimum average unless the method specifically called for a web measurement type, the same as in

Table 18. The Tzortzinis method remains in relatively close groups of points for all 17 tests. This behavior is because the AASHTO and AISC shear capacity equations are very similarly structured, and the other methods apply a capacity reduction ratio to these values. The similarity between the methods is a detrimental feature, as many of the predicted values in these cases significantly overestimate the capacity.

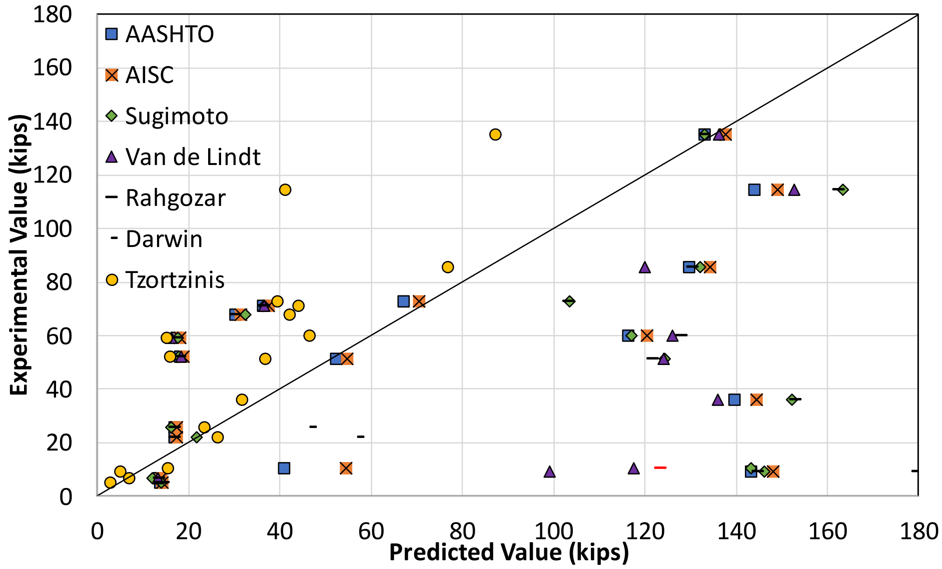

Figure 59. Prediction Error Plot for All Tested Calculation Methods

The prediction error scatters for only the AASHTO and Tzortzinis methods are displayed in the plot in Figure 60. In both cases, the lower damage effective web area is used as the web thickness measurement. In the case of the AASHTO results, using the lower damage effective web area results in less scatter than the minimum web thickness in Figure 60. However, half of the values still lie below the 45-degree line, meaning that they overestimate the tested value. The Tzortzinis method, instead, much more closely follows the experimental value trend than any other shear capacity method. Additionally, the values tend to fall above the 45-degree line, which signifies underestimating the actual shear capacity or a more conservative result.

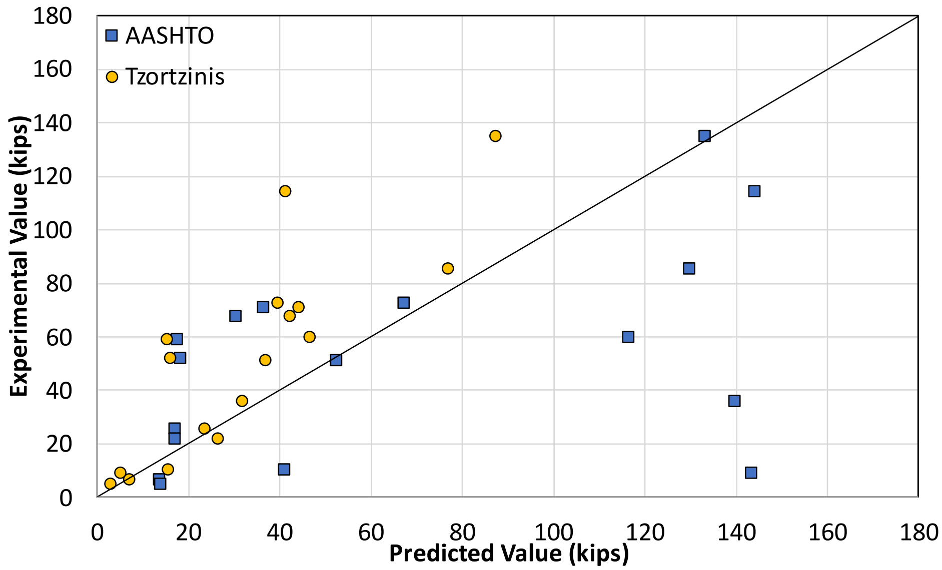

Figure 60. Prediction Error Plot for AASHTO and Tzortzinis Capacity Calculation Using Average Thickness over Damaged Web Area

Several reasons may explain why the Tzortzinis equations performed better than the others. The Tzortzinis method considers web opening's effect during the web thickness calculation rather than having to ignore or average holes. Considering through-web damage is an important feature of a suitable capacity calculation method due to the significant effect of holes on stress concentrations. As shown in the major strain field discussion, web holes are typically the sites of localized web failures that govern the capacity of beams that would otherwise continue to resist shear loads. The Tzortzinis equations factor in the length and height of a single web hole; however, no guidance is provided regarding beam ends with multiple web holes. In these cases, multiple holes can be conservatively treated as a single large hole encompassing all the present openings, but this may provide overly conservative results for widely dispersed web holes.

The Tzortzinis study also uses the corroded web thickness averaged over the area defined in MassDOT bridge rating guidelines previously illustrated in the Literature Review section as Figure 11. This area was defined as the lower 4 inches of the web end above the bearing. For the 17 beams in this study, the band of lower web corrosion was typically found in the lower 3 inches of the web above the bottom flange. Averaging the web thickness over 4 inches tended to capture uncorroded sections of the web, which increases the average web thickness, whereas the bottom 3 inches above the bearing provided more conservative results. Figure 61 shows the effect of using the 3-inch and 4-inch averaged areas for calculating the AASHTO shear capacity. The results trend closer to the test results and are much more conservative than using the minimum average cross-section. Additionally, reducing the equivalent web area from 4 inches in height to 3 inches noticeably moved several of the points under the 45-degree line closer to the line, improving the results.

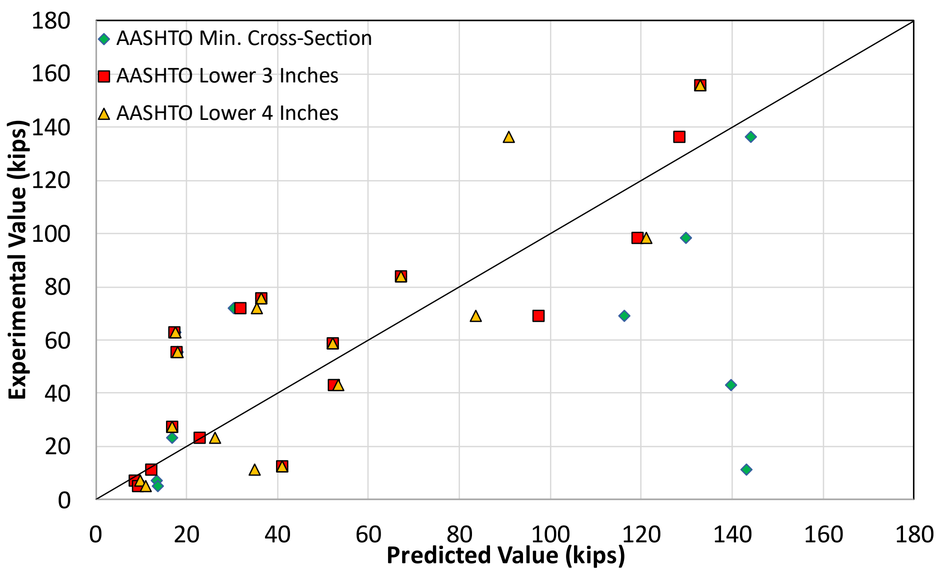

Figure 61. AASHTO Shear Calculation Using Minimum Cross Section vs. Lower 3-Inch Average vs. Lower 4-Inch Average

Another significant difference from the other methods is that the Tzortzinis method calculates the reduced beam capacity directly instead of applying a reduced ratio to the undamaged beam strength. While the yield capacity equation is very similar to the AASHTO and AISC shear capacity equations, the web-crippling equation governed for every beam. The AASHTO, AISC, and the Tzortzinis yield equation are all calculated using the steel yield strength and the cross-sectional area of the web multiplied by various factors. The Tzortzinis web crippling equation instead uses a much different structure with statistically derived coefficients. The Tzortzinis equations are based on the original MassDOT equations, which are compared in Figure 62. The prediction error plot shows that the modifications made to the crippling equation have made a significant improvement to the reliability of the results, as many of the MassDOT results provide considerable overestimates of the test results.

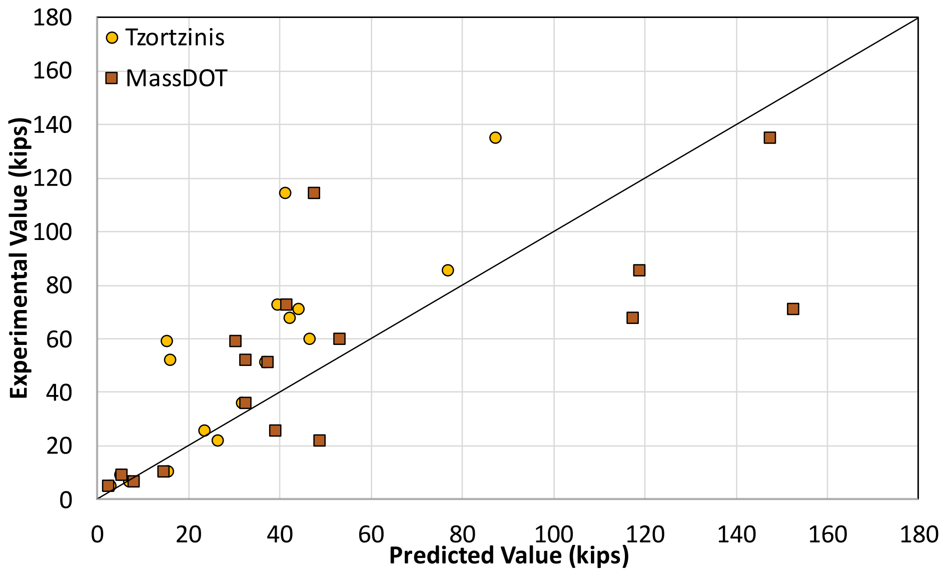

Figure 62. Prediction Error Plot for MassDOT and Tzortzinis Capacity Calculation Methods

Figure 63 shows the comparison of maximum shear stress values for each of the tested methods, which were calculated using an assumed undamaged beam cross-section. While this value does not account for the decreased section area in damaged beams which would result in higher shear stress values, this comparison gives another indication of the trend set by the Tzortzinis method, which still more closely resembles the results of the experimental values than the other analyzed methods and tends to stay above the 45-degree line indicating conservative estimations. Additionally, the spread of the data points between methods for each test is typically close together, while the shear stresses associated with the Tzortzinis method tend to shift the results further to the left, meaning that the estimates were lower and more conservative.

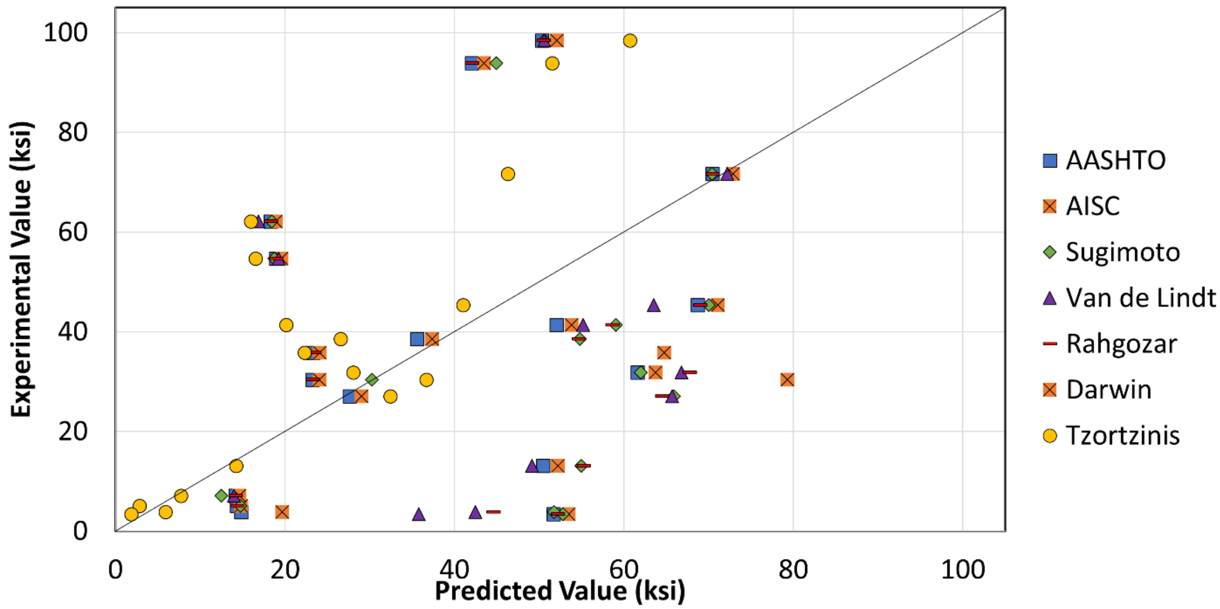

Figure 63. Prediction Error Plot Using Maximum Stress Calculated with Original Beam Cross-sections

One discrepancy with the Tzortzinis method is that the corroded web resistance is calculated as the minimum of the nominal yielding and web local crippling capacities. In the 2019 study, the author recognizes that the method does not include a capacity equation that considers the effect of web buckling, which is reciprocated in the MassDOT Bridge Manual. During the current study, however, web cracking, crippling, and buckling behavior occurred during the large-scale testing process; however, most tests failed due to web crippling. Typically, web buckling occurred on beams with low amounts of damage, less than 1/16 inches of total section loss, or those with web thinning at mid-height. It would be acceptable to continue using the AASHTO shear calculation methods with slightly adjusted thickness percentages in these cases.

In summary, the Tzortzinis method was the most accurate method for calculating the remaining shear capacity of beams exhibiting beam-end corrosion. The effective web area used to determine the average web thickness used with the Tzortzinis method which provided the best agreement with the test data is shown in Figure 64. This area was defined as three inches above the bottom flange extending for the full support length (N) plus one beam height from the interior support (h).

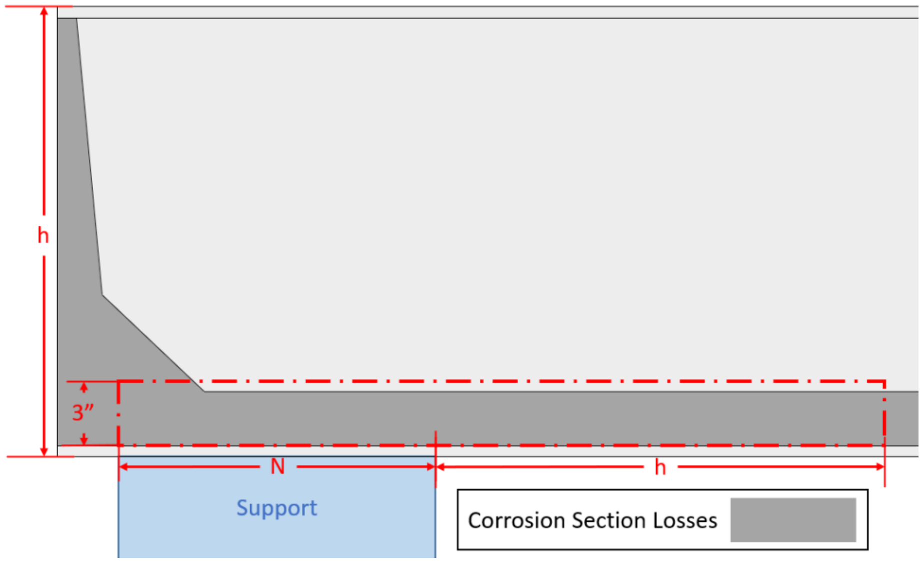

Figure 64. Average Thickness Area for Corroded Web Measurement

Finally, due to inaccuracies with the predicted results in beams with extreme amounts of section loss, a lower bound of section loss must be defined to prevent these calculations' overzealous application to high-risk structures. Similar to the Van de Lindt study, results from this study showed that shear capacities of beams with webs with greater than 35% section loss cannot be accurately predicted. As such, these beams should either be rated with an overly conservative method, such as using the minimum recorded web thickness with the AASHTO shear calculations or assumed non-functional to carry service loads.

CHAPTER 5: Conclusions

5.1 Conclusions

The intent of the research was to determine an approach to predicting the remaining shear capacity in steel beams exhibiting section losses at their beam ends due to corrosion. Through experimental testing of 17 steel beams with this corrosion and subsequent analysis of the load and strain data, the following conclusions were determined.

The full-scale testing results showed that damage location significantly influences the stresses during loading and failure mode of a corroded beam end. The extent of corrosion damage, such as web holes, varies in effect depending on its position in the web. Heavy localized corrosion can cause initiation of shear buckling behavior even outside of the support area. However, beam end corrosion caused by deck joint failure typically results in heavy corrosion localized directly above the support. As such, the most prevalent failure mode for corroded beam ends tends to be web crippling in the web above the bearing.

This study recommends that the shear capacity calculations defined in the 2019 study "Development of Load Rating Procedures for Deteriorated Steel Beam Ends" by Georgios Tzortzinis, Simos Gerasimidis, Sergio Breña, and Brendan Knickle should be used to predict the capacity of deteriorated steel beam end webs in bridges with a maximum of 35% average section loss. In addition to the visible trend on the error plots, the Tzortzinis procedure for corroded beam end shear capacities increased the correlation coefficient from 79% using the AASHTO method to 84%, while the other methods varied between 75% for the AISC method as low as 36% for the Sugimoto and Van de Lindt methods. After comparison to other shear calculation methods and studies, it has been determined that the Tzortzinis approach provided conservative results, which were also more accurate than existing VDOT procedures. However, beams with web holes introduce highly unpredictable behavior which cannot be predicted reliably by any of the methods assessed.

The existing procedures for managing corroded beam ends may be improved by updating the definitions for the section loss area to be measured for analysis and the method of section loss measurement and quantification in corroded beam ends. This will help by ensuring consistent load rating results regardless of the capacity prediction methods used. This study recommends that future measurement of beam end corrosion should be averaged over the lower 3 inches of the web between the beam end and a length between the beam end and one beam height from the inner face of the support. Inspectors should be equipped with an ultrasonic steel thickness gauge to capture the web thickness in these areas. Measurements should be taken at 1-inch intervals vertically starting from the bottom of the web above the far edge of the bearing, continuing up the height of the web 3 inches totaling four thickness measurements. This process should be repeated across the full support length plus one beam height at 1-inch intervals. This recommended process may be abbreviated for webs with less severe or uniform section losses in this defined area. Such deviations from the recommended 1-inch interval process may be made at the discretion of the load rater; however, these changes must be reported in the inspection report accompanying the provided web thickness so that load raters are always made aware and may request more extensive measurements if they suspect that the previous measurements were inadequate.

5.2 Future Studies

The current project was conducted with the specific purpose of determining an appropriate method for evaluating the remaining capacity of corroded steel bridge beams in the context of load rating for the Virginia Department of Transportation. As such, several possible topics of interest were unable to be addressed due to restrictions on the available time to conduct this study. This section of the document will discuss a few of these topics, which may be further analyzed in future studies related to steel bridge beam corrosion.

As stated in the conclusions, the results of the current study's load tests did not focus enough on the influence of web holes to definitively recommend any of the reviewed methods to estimate the remaining capacity of beams with web holes. Future studies should consider the remaining capacity of beams with web openings while also understanding the difficulty of assessing beams with features such as multiple web holes, irregular web holes, and the influence of the location of web holes.

While corrosion due to compromised deck joints is typically localized to the beam end, corrosion damage on steel beam, timber deck bridges can appear anywhere along the deck where cracking of the road surface appears. As such, advanced localized corrosion of the beam flanges within the span is possible to occur and further research may be conducted to determine an appropriate method of determining the effects of steel web corrosion on bending capacity. Additional research may also be conducted to determine the effects of load distribution between undamaged beams adjacent to a beam with localized beam end corrosion. The current study was interested in assessing the behavior of a single beam end in shear, which excludes the contribution of the rest of the bridge structure as a redundant system. As such, future research may include full-scale bridge testing or finite element modeling of a full bridge structure to address this topic.

Finally, a highly relevant though unaddressed topic for beam end corrosion is repair and retrofit of corrosion damaged beams. Many of the beams tested in this study initially included temporary repairs such as wood stiffeners and bolted and welded steel angles to act as longitudinal and transverse web stiffeners. Research may be done to determine the most effective, easily implementable, and economical solution for increasing the available shear capacity in corroded steel beam ends prior to full superstructure replacement.

REFERENCES

AASHTO. (2017). *AASHTO LRFD Bridge Design Specifications 8th Edition*.

Ahn, J. H., Kim, I. T., Kainuma, S., and Lee, M. J. (2013). "Residual shear strength of steel plate girder due to web local corrosion." *Journal of Constructional Steel Research*.

AISC. (2016). *AISC 360-16: Specification for Structural Steel Buildings*.

ASTM International. (2021). "ASTM E8 / E8M-21, Standard Test Methods for Tension Testing of Metallic Materials." West Conshohocken, PA.

Cramer, S., and Covino, B. (Eds.). (2003). *ASM Handbook Volume 13A: Corrosion Fundamentals, Testing, and Protection*. ASM International.

Darwin, D., and Donahey, R. C. (1988). "LRFD For Composite Beams with Unreinforced Web Openings." 114(3), 535–552.

FHWA - Federal Highway Administration. (2012). "Bridge Inspector' s Reference Manual." 1, 2004.

Kayser, J. R., and Nowak, A. S. (1989a). "Capacity Loss Due to Corrosion in Steel-Girder Bridges." *Journal of Structural Engineering*.

Kayser, J. R., and Nowak, A. S. (1989b). "Reliability of corroded steel girder bridges." *Structural Safety*.

Kim, I. T., Lee, M. J., Ahn, J. H., and Kainuma, S. (2013). "Experimental evaluation of shear buckling behaviors and strength of locally corroded web." *Journal of Constructional Steel Research*.

van de Lindt, J. W., and Ahlborn, T. M. (2005). *Development of Steel Beam End Deterioration Guidelines*.

MassDOT. (2020). "LRFD Bridge Manual - Part I CHAPTER 7 LRFR BRIDGE LOAD RATING GUIDELINES." (January), 1–16.

Narmashiri, K., Ramli Sulong, N. H., and Jumaat, M. Z. (2011). "Flexural strengthening of steel I-beams by using CFRP strips." *International Journal of Physical Sciences*, 6(7), 1620–1627.

Rahgozar, R. (2009). "Remaining capacity assessment of corrosion damaged beams using minimum curves." *Journal of Constructional Steel Research*.

Roberge, P. (2012). *Handbook of Corrosion Engineering*. McGraw-Hill Education.

Sugimoto, I., Kobayashi, Y., and Ichikawa, A. (2006). "Durability evaluation based on buckling characteristics of corroded steel deck girders." *Quarterly Report of RTRI (Railway Technical Research Institute) (Japan)*, 47(3), 150–155.

Tzortzinis, G., Gerasimidis, S., Breña, S., and Knickle, B. (2019). "Development of Load Rating Procedures for Deteriorated Steel Beam Ends." (19–008).

Tzortzinis, G., Knickle, B., Gerasimidis, S., Bardow, A., and Breña, S. (2018). “Identification of Most Common Shapes and Locations for Beam End Corrosion of Steel Girder Bridges.” *Transportation Research Board 92th Annual Meeting*.

VDOT. (2007). *Process for Reviewing VIRTIS Analysis Steel Structure Memebers with Holes in Web*.

Virginia Department of Transportation. (2016). “VDOT Supplement to the AASHTO Manual for Bridge Element Inspection.” 88.

Appendix A: Wiring Diagram

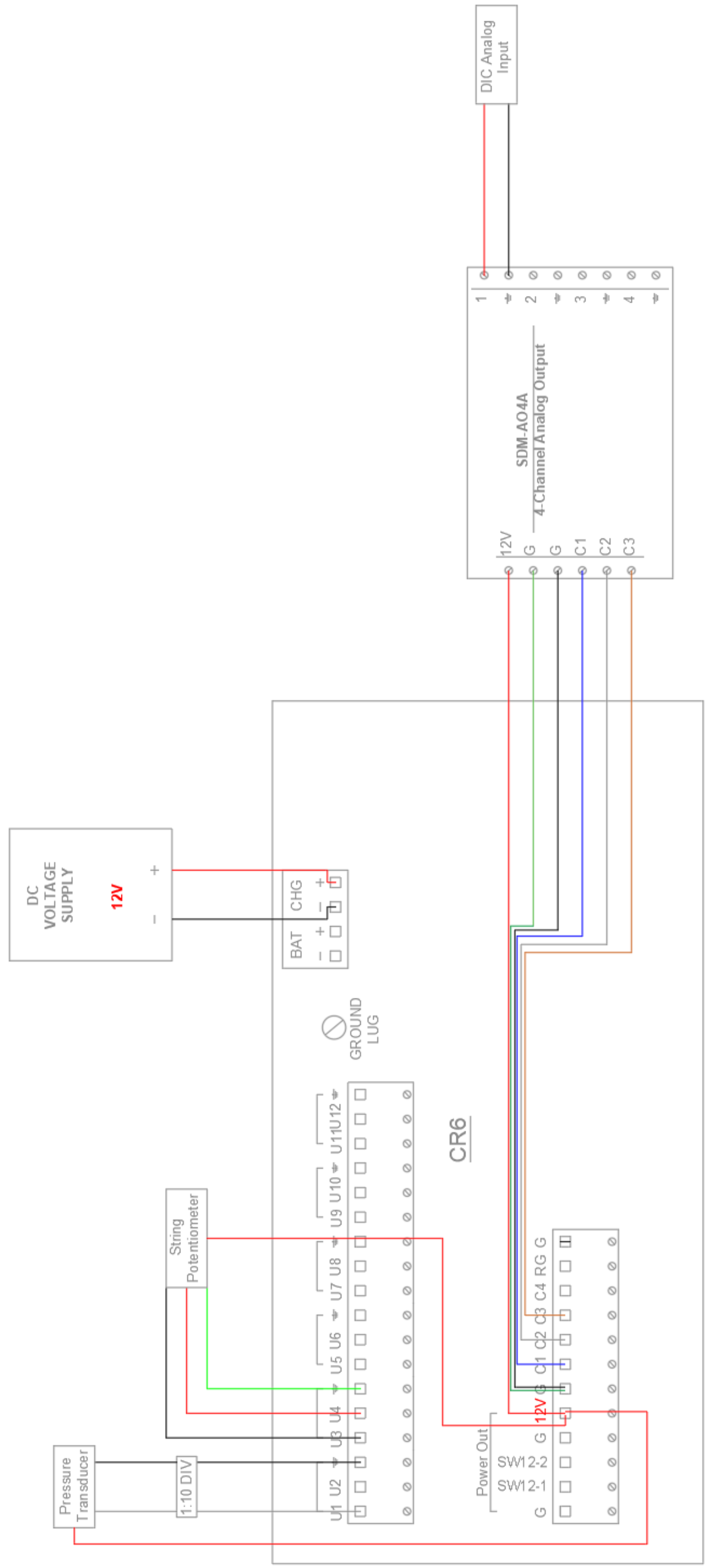

Figure 65. Data Logger Wiring Configuration